CENTRO DE INVESTIGACIÓN Y DE ESTUDIOS AVANZADOS
DEL INSTITUTO POLITÉCNICO NACIONAL

UNIDAD MÉRIDA
DEPARTAMENTO DE FÍSICA APLICADA

Simulation of Synchrotron Radiation for the CERN Highest-Energy Accelerators

Thesis presented by

Gerardo Guillermo Cantón

To obtain the degree of:

Doctor in Science

in

Theoretical Physics

Thesis Directors
Dr. Frank Zimmermann
Dr. Francisco Carlos Larios Forte

CERN-THESIS-2018-468
30/08/2018

Mérida, Yucatán, México. August 2018

Dedicated to my family who has always believed in me.

Declaration of Authorship

I, Gerardo Guillermo Cantón, declare that this thesis titled, 'Simulation of Synchrotron Radiation in CERN highest energy Accelerators' and the work presented in it are my own. I confirm that:

- This work was done wholly or mainly while in candidature for a research degree at CINVESTAV.
- Where any part of this thesis has previously been submitted for a degree or any other qualification at CINVESTAV or any other institution, this has been clearly stated.
- Where I have consulted the published work of others, this is always clearly attributed.
- Where I have quoted from the work of others, the source is always given. With the exception of such quotations, this thesis is entirely my own work.
- I have acknowledged all main sources of help.
- Where the thesis is based on work done by myself jointly with others, I have made clear exactly what was done by others and what I have contributed myself.

Signed:

Gerardo Guillermo

Date: September 5, 2018

"God used beautiful mathematics in creating the world."

Paul Dirac[1]

"It is a great thing to be a forgetful scientist. Everyday you get to learn a new thing!– even if it is the same one."

Gerardo Guillermo

---

[1] As quoted in The Cosmic Code : Quantum Physics As The Language Of Nature (1982) by Heinz R. Pagels, p. 295; also in Paul Adrien Maurice Dirac : Reminiscences about a Great Physicist (1990) edited by Behram N. Kursunoglu and Eugene Paul Wigner, p. xv

Abstract

by Gerardo Guillermo Cantón

In circular accelerators at energies in the order of TeV, synchrotron radiation (SR) is very high, even in a hadron beams. SR could be regarded as an important heat load to the cryogenic system cooling the superconducting electromagnets. In this work SR is simulated using `Synrad3D` to obtain an azimuthal distribution of photon absorption in the arcs of CERN highest-energy accelerators, both: existing and in design phase. This help us draw conclusions on the applied methods to mitigate the effects of SR.

Resumen

by Gerardo Guillermo Cantón

En aceleradores circulares de partículas energías en el orden de TeV la radición de sincrotrón es muy alta, incluso usando rayos de hadrones. Esta radiación puede representar una carga calórica demasiado grande para electroimanes trabajando en estado criogénico. En este trabajo se simula la radiación de sincrotrón generada por un haz de protones en el LHC, utilizando `Synrad3D`, para obtener un mapa azimutal de la distribución de absorción de fotones en los arcos de los aceleradores de más alta energía del CERN, ya sea para los existentes y también para los que están en fase de diseño. Con la ayuda de estos mapas sacamos conclusiones sobre los métodos para mitigar los efectos de la radiación de sincrotrón.

Acknowledgements

I thank to the members of this thesis committee: Dr. Victor José Sosa Villanueva, Dr. Gabriel Perez Ángel, Dr. Antonio Bouzas Arteche and Dr. Francisco Carlos Larios Forte.

The completion of this project could not have been accomplished without the support, help and guidance of my supervisors: Jesus Guillermo Contreras Nuño and Frank Zimmermann.

I thank Consejo de Ciencia y Tecnología (CONACYT) and CINVESTAV for the financial support during my PhD. studies. I also thank CERN for all the resources made available to me.

I thank the 'BEAMS CERN-CONACyT' programme and ARIES for their grants and financial support during my visit at CERN.

I also want to thank Dr. Geonel Rodriguez and Dra. Cristina Vargas, Department Head and Head of Academic affairs at Cinvestav, respectively as well as Ms. Zhirnay Rodriguez for her adminsitrative help at Cinvestav; As well as CERN's administrative personnel, specially Alessia Valenza and Delphine Reviron.

I thank all members of the HSS section at CERN, where my stay took place, for so many useful discussions, with a special mention to Massimo Giovannozzi, Rogelio Tomás, and Laurent Deniau.

I thank several people at CERN who helped me understand the electron cloud phenomena and effects. Amongst them Lotta Mether, Giovanni Iadarola, and Giovanni Rumolo.

I am very grateful with CLASSE which made some computational resources available to me. I cannot express enough gratitude to David Sagan, who helped in all stages with the use of `Synrad3D`: from building, to support and debugging. I thank James Crittenden and Stephen Popprocki who broadened my vision regarding interactions between photons and technical vacuum chamber surfaces.

A special acknowledgment to the team of experimentalists at Instituto Nazionale di Fisisca Nucleare, Laboratori Nazionali di Frascati. Roberto Cimino, Eliana La Francesca, Marco Angelucci, Ignasi Bellafont among others.

Last but not least, I acknowledge my colleagues and collaborators in the University of Guanajuato: Humberto Maury Cuna and Edgar Ortiz Ocampo.

Contents

List of Figures

List of Tables

Abbreviations

AC	**A**lternate **C**urrent
AFS	**A**ndrew **F**ile **S**ystem
ALICE	**A** **L**arge **I**on **C**ollider **E**xperiment
ATLAS	**A** **T**oroidal **L**HC **A**pparatu**S**
CERN	**C**onseil **E**uropéen pour la **R**echerche **N**ucléaire
	European Organization for Nuclear Research
CFH	**C**onfoederatio **H**elvetica **F**ranc
CMS	**C**ompact **M**uon **S**olenoid
DC	**D**irect **C**urrent
EC	**E**lectron **C**loud
EW	**E**lectro-**W**eak
GERL	**G**eneral **E**lectric **R**esearch **L**aboratory
FODO	**Fo**cus/**D**ef**o**cus
FNAL	**F**ermi **N**ational **A**ccelerator **L**aboratory
LBNL	**L**awrence **B**erkley **N**ational **L**aboratory
LEP	**L**arge **E**lectron **P**ositron
LHC	**L**arge **H**adron **C**ollider
LHCb	**LHC** **b**eauty
LEP	**L**arge **E**lectron - **P**ositron Collider
LxPLUS	**L**x **P**ublic **L**ogin **S**ervice
PDF	**P**hoton **D**istribution **F**unction
PS	**P**roton **S**ynchrotron
RF	**R**adio **F**recuency
SLC5	**S**cientific **L**inux **C**ERN **5**

SMIF	**S**ynrad3D **M**ain **I**nput **F**ile
SMOF	**S**ynrad3D **M**ain **O**utput **F**ile
SPEAR	**S**tanford **P**ositron **E**electron **A**ccelerating **R**ing
SPS	**S**uper **P**roton **S**ynchrotron
SR	**S**ynchrotron **R**adiation
SSS	**S**hort **S**traight - **S**ection

Symbols

d	Distance	m
E	Energy	eV
f	focal length	m
l	length	m
$\mathcal{L}$	Luminosity	$\mathrm{cm}^{-2}\mathrm{s}^{-1}$
P	Power	W (Js^{-1})
s	Transversal Direction	m
T	Temperature	K
α_f	fine structure constant	unitless
δ	relative momentum error	unitless
γ_r	Relativistic gamma factor	unitless
ε_c	Critical photon energy	eV
ρ	Radius	m
σ	Surface roughness	nm
ω_c	Critical photon frequency	rads^{-1}
g	Magnetic gradient	dB_y/dx
κ	Curvature	$1/\rho$
K	Focusing parameter	$\kappa + k$
k	Focusing Strength	$\frac{e}{pc}g = \frac{ec}{\beta E}g$
$B\rho$	Beam rigidity	p/e
θ	deflection angle of a bending magnet	l/ρ

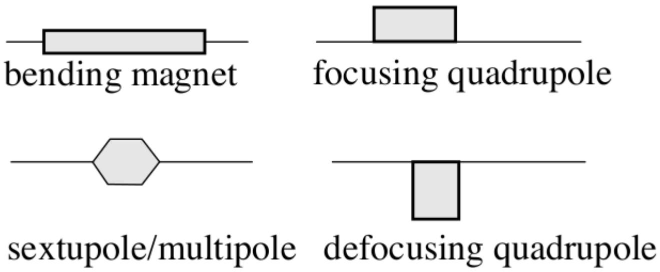
bending magnet
focusing quadrupole
sextupole/multipole
defocusing quadrupole

Introduction

The emission of Synchrotron Radiation (SR) results from a change in direction of relativistic charged particles. Since SR was first directly observed at the General Electric Research Laboratory (GERL) Synchrotron in 1947 [1], the interest in this phenomenon has ever more increased. Even though a theory of synchrotron radiation had already been developed before its discovery, it is still being developed at present, a hundred years later.

In typical electron storage rings and circular accelerators, the emitted synchrotron radiation is characterized by high power levels and fairly high photon energies (e.g. several keV). Nowadays, dedicated electron accelerators are being operated for the sole purpose of producing SR with specific characteristics. In other accelerators, however, SR is still considered a secondary effect which is limiting the performance of the machine.

The power of the emitted SR depends on the square of the relativistic Lorentz factor (γ_r^2). For this reason, SR was hitherto considered negligible in proton accelerators, since at the same beam energy (γ_r^2) is about 2000 times lower than for the electrons. It was not until the construction of the Large Hadron Collider (LHC), with a $\gamma_r^2 \geq 7460$ for protons, that SR became significant also for hadron beams and that the negative effects of SR were no longer negligible.

The LHC cryogenic environment is said to be the coldest place in the universe. In order to keep the superconductor magnetic coils at 1.9 K, gigantic cryogenic plants are used. One of the main heat loads of the arcs is SR with a power deposition of 0.17 W/m/aperture [2].

The nominal vacuum in the LHC is as low as interstellar vacuum, $\sim 10^{-14}$ bar. Photons from SR can erode molecules and particles from the wall degrading this vacuum. Yet another problem related to SR is the formation of electron clouds (EC). Such clouds can grow from seed electrons torn from the wall by incident photons. These initial photo-electrons are attracted and accelerated by the electric field of the passing proton bunches. Inside the accelerator magnets, their motion is also constrained by the magnetic field lines. When accelerated electrons hit the vacuum chamber they can generate secondary electrons leading to an avalanche build up of electrons, which can generate excessive heat load that can no longer be removed, resulting in the "quenching" (unwanted transition to the normal conducting state) of superconducting magnets. Electron-cloud related problems are the main motivation for the studies of this thesis.

The main objective of this work is to map the absorption points of SR photons in the arcs of the highest-energy proton accelerators at CERN, built or in design face. These are LHC and its upgarde HL-LHC, HE-LHC and FCC-hh. These photon-absorption points can then be used to generate a photon distribution function (PDF) as an input for electron-cloud simulations. To compute this map of absorption points, we use the code `Synrad3D` developed at Cornell [3]. `Synrad3D` generates and tracks synchrotron-radiation photons in an accelerator beam line, including specular and diffuse reflection on the surface of the chamber wall. The photons are generated randomly in any bending field, with initial parameters determined by the local beam distribution, the local electromagnetic field, and by the beam energy. When a photon hits the chamber wall its reflection probability depends on the energy and angle of incidence, as well as on the material, including, possibly, combinations of multiple surface layers, and on the surface roughness. The photon-absorption points for each of these accelerators were found and it is presented either as integrated azimuthal distributions or histograms of absorption per side of the beam screen.

This doctoral project is also developed within a larger programme aiming to promote and progress accelerator science in Mexico [4]. As a part of these activities, a group of mexican colleagues [5] have proposed to design and build a electron linear accelerator (linac). This linac would be the first radio-frequency (RF) based instrument fully developed in Mexico [6].

The thesis is structured as follows. The first chapter provides a basic introduction to accelerators, their history and their design, with some emphasis on circular hadron accelerators. In the second chapter we qualitatively describe SR and its relation to EC build-up. In the third chapter It presents some features of the highest-energy circular colliders for which our analysis was implemented. A description of the code `Synrad3D` is given in the third chapter. Also some tests and benchmarking of the `Synrad3D` code will be mentioned. Finally, in the last two chapters, we present our main results, and discuss their implications for CERN's present and future highest-energy circular accelerators.

Chapter 1

Particle Accelerators

Particle accelerators are machines whose name is self explanatory. They were originally developed for nuclear physics. Although we could argue that a cathodic tube is an accelerator itself, we count as the first accelerator one that was designed, after Rutherford challenged the scientific community in 1927, to accelerate charged particles to energies higher than natural α-decays [7], which have a typical energy of 5 MeV. This accelerator was the Cockcroft-Walton multiplier, which was used to produce the first ever reported nuclear fission. The original setup is shown in Fig. 1.1. It consisted of an AC power source charging a ladder of capacitors by means of diodes, generating a large voltage output [8]. Following the relation between the electric field ($\vec{E}$) and the scalar potential (V): $\vec{E} = -\nabla V$ and equating Newton's second law of motion ($\vec{F} = m\vec{a}$) to the Lorentz force ($\vec{F} = q(\vec{E} + \vec{v} \times \vec{B})$) we infer that the acceleration in an electrostatic accelerator such as the Cockcroft-Walton is: $\vec{a} = -\frac{q}{m}\nabla V$. Ever since, accelerators have not stopped evolving. Scientists kept building larger and larger accelerators until they hit a limit with electrostatic fields due to voltage breakdown [9].

A new technique for accelerating charges emerged. Already in 1924 Gustav Ising had proposed using drift tubes to shield the charged particle from a pulsed voltage [10], and in 1928 Rolf Wideröe suggested using a radiofrequency (RF) system [11]. To prove this principle Wideröe built the first linear accelerator or linac, and RF acceleration was born. Using the RF acceleration principle and one

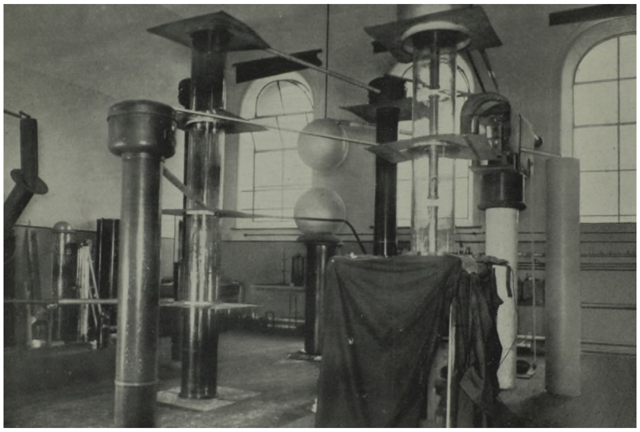

Figure 1.1: Cockcroft-Walton accelerator original setting.
Picture taken from [8]

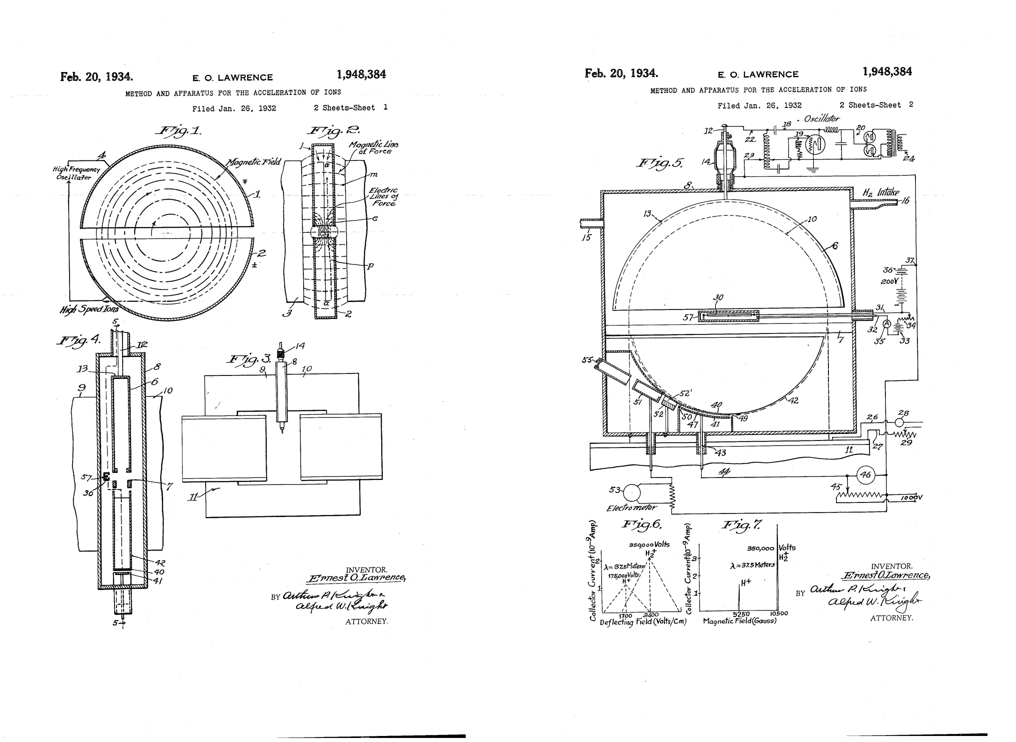

Figure 1.2: E. O. Lawrence patent of the cyclotron in the U.S.A.
Picture taken from [12]

of Wideröe's ideas, Ernest Lawrence set electrons in a curved path by applying a perpendicular magnetic field so that the electrons would pass several times through and accelerating gap. Figure 1.2 shows Lawrence drawings in his 1934 patent and in Fig. 1.3 we see Lawrence standing next to his 1.5 m diameter cyclotron in the University of California at Berkeley.

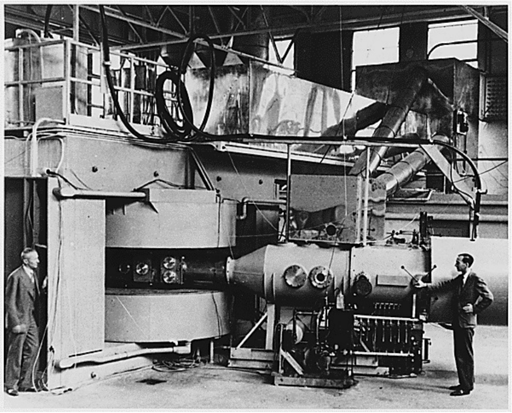

Figure 1.3: E. O. Lawrence (left) next to his 1.5 m in diameter cyclotron at LBNL. Picture from the U.S. Department of Energy

Using yet another of Wideröe's ideas, Donald Krest built a machine in 1940 that would keep an almost constant orbit while accelerating the electrons. This is achieved by increasing the magnetic field over time. Betatrons where widely used in hospitals as sources of X-rays. In 1944 Vladimir Veksler [13] and separately in 1945 Edwin McMillan [14] published the principles of phase stability which relates the synchronicity of the orbiting particles and the electric field of the time-varying RF; this principle is explained in Sec. A.8.1.1. Using this principle Frank Goward and D.E. Barnes built the first synchrotron by modifying an existing betatron in England [15]. The second synchrotron accelerator was built by GERL and it was there where synchrotron radiation was first observed. This effect will be further discussed in Chapter 2.

Given the large mass of protons compared to electrons, they become ultra relativistic at much higher energies, and this posses a difficulty to synchrotrons: They need to increase the magnetic field as the particles gain energy. This technological problem had the effect of proton synchrotrons developing much latter. Te cosmotron was the first synchrotron to achieve the GeV regime [16], and the first one to use the beam for external experiments [17].

After the idea of strong focusing was developed, using focusing-defocusing quadrupole magnets, it became possible to reach even higher energies. The CERN Proton Synchrotron (PS) started operating in 1959, and it reached energies of 28 GeV.

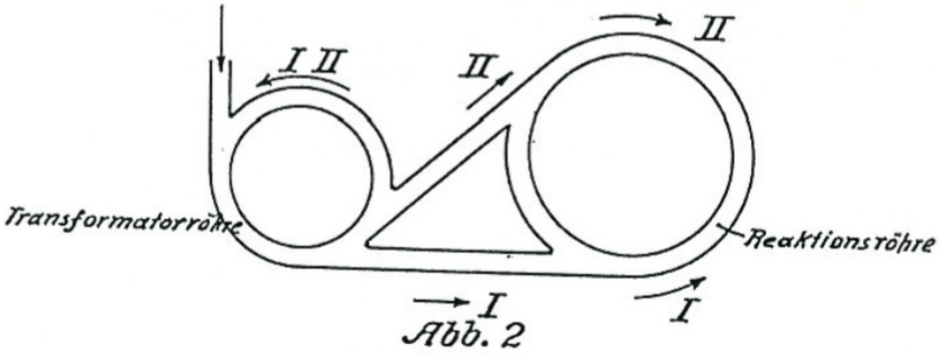

Figure 1.4: Original diagram from the collider patent by Wideröe.
Picture taken from [20]

A machine to collide beams, hence greatly improving the energy released, was first patented by Wideröe in 1943 [18]. The patent design is shown in Fig. 1.4. Although some people would consider that idea to be trivial and obvious [19], it was irrelevant at that time because the repetition rate would have been too low. It was until storage rings were developed, that colliders became a practical application. The first circular proton collider consisted on protons accelerated in the Proton Synchrotron (PS) and then transferred to the newly built Intersecting Storage Rings (ISR) in 1971. The layout is shown in Fig. 1.5. The ISR had 300 m in diameter, the maximum design energy was 28 GeV, but the bunched particles could be further accelerated in the ISR up to 31.4 GeV at the price of reduced luminosity [21]. It had eight intersections where the collisions took place. To achieve its maximum current of 20 A it was required to empty the PS several times into each of the two rings.

In 1973 at the Stanford Positron Electron Accelerating Ring (SPEAR), researchers realized that the SR emitted by the beam was too high to allow it to go to waste, hence creating the Stanford Synchrotron Radiation Laboratory (SSRL). Although the goal of SSRL was to take advantage of the 'wasted' energy emitted as SR, eventually SPEAR became solely dedicated to SSRL. Nowadays there are several accelerators around the world dedicated only to emit SR, these are known as light sources.

Accelerators around the world kept growing in number, size, energy reach, and

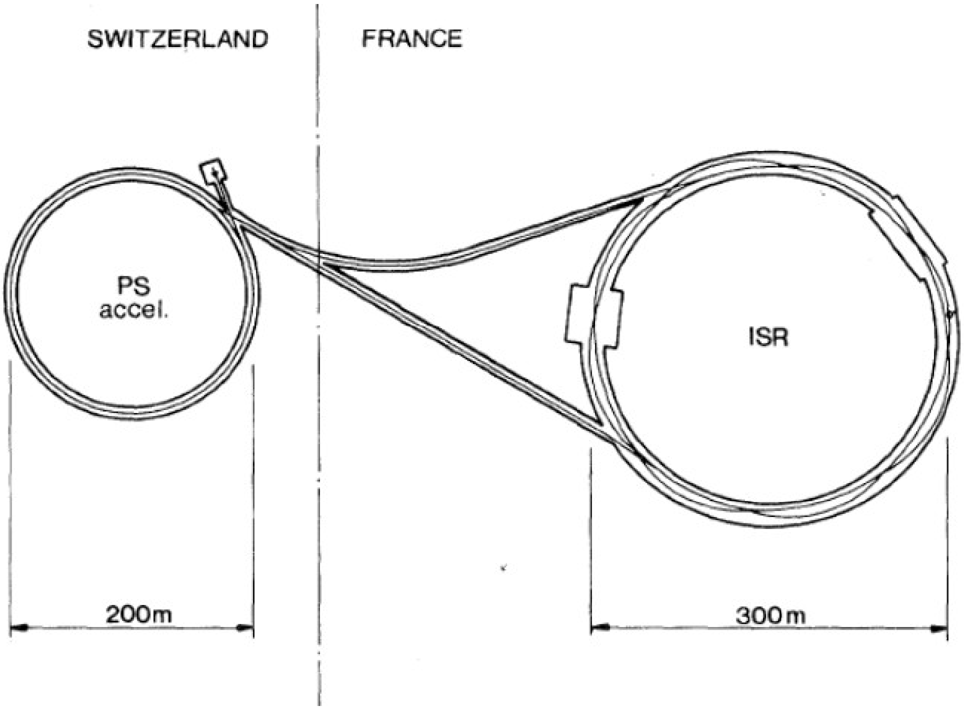

Figure 1.5: Layout of the ISR. taken from [21]

luminosity over the following years. An important technological development in the decade of 1970 was the use of superconducting materials to greatly improve the efficiency of RF cavities and bending magnets [22].

In 1983, the Fermi National Accelerator Laboratory (FNAL) replaced its main ring with a proton-antiproton accelerator and collider with center-of-mass (CoM) collision energy of 1.8 TeV. It was called the Tevatron, the first accelerator reaching energies superior to 1 TeV. It remained the highest energy collider until the construction of LHC, which is further discussed in Sec. 3.1.

Chapter 2

Synchrotron Radiation

This chapter is dedicated to a brief, mostly qualitative description of synchrotron radiation (SR). For a deeper understanding, the author recommends chapters 1, 2 and 3 of [23]; and chapters 12 and 14 from [24].

2.1 Radiation

The idea of electromagnetic waves has always fascinated the minds of physicists around the world. In 1887 G. Hertz generated, emitted and received electromagnetic waves. This was an experimental proof of Maxwell's equations. The source of that radiation were oscillating charges.

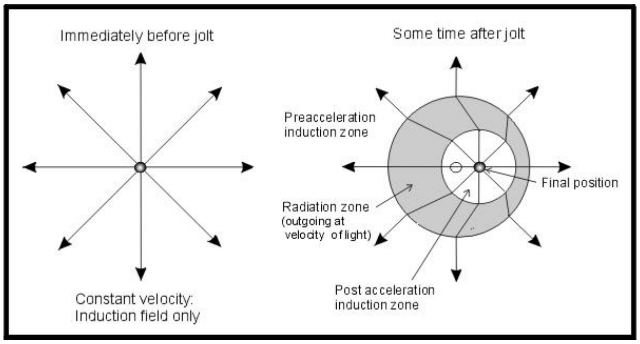

FIGURE 2.1: Electromagnetic field of a charge a) static b) after a short jolt. Picture taken from [25].

Electromagnetic radiation is a consequence of the finite velocity of light [26]. While a particle is at rest, or in a constant motion, it carries electric field lines radially out to infinity. If we suddenly accelerate this charge, the information of that acceleration propagates with the speed of light, so that information is only known to a vicinity defined by

$$\Delta d \leq c * \Delta t. \tag{2.1}$$

The resulting distortion of the field lines, which is travelling away from the charge, is what we call electromagnetic radiation. This concept is illustrated in Fig. 2.1.

2.1.1 Conservation laws

The emission of electromagnetic radiation from charged particles is a classical phenomenon. We may therefore use a visual approach to gain some insight into conditions and mechanisms of radiation emission. The emission of electromagnetic radiation involves two components, the charged particle and the radiation field. For the combined system energy–momentum conservation must be fulfilled. These conservation laws impose very specific selection rules on the possible emission processes.

2.2 Synchrotron radiation

We call synchrotron radiation (SR) the radiation emitted from a charged particle with angular acceleration. In this description, we present the basic properties, considering electrons as the moving charges, but they could be easily replaced by any other charged particle, in particular by protons.

The interest in electromagnetic theory grew from the mid 1940s with the development of theories for the radiation emitted by free electrons, partly driven by the development of high energy electron accelerators.

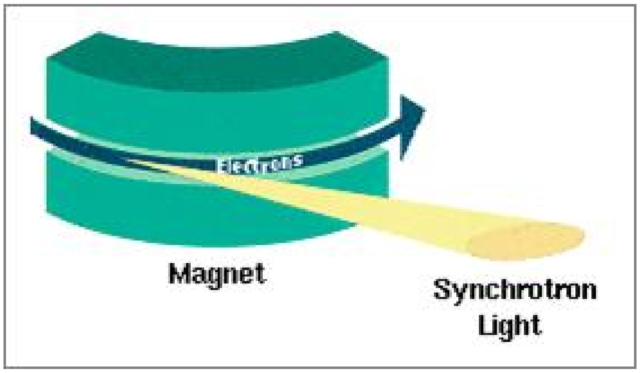

Figure 2.2: Synchrotron radiation produced by a bending magnet.
Picture taken from [27].

In 1944 Pomeranchuk discussed a weakness of the betatron principle, and he derived an energy limit due to the losses from electromagnetic radiation. Indeed, the energy that charged particles lose to SR posed great technological and economic obstacles to further increasing the energy of circular accelerators. To surpass this limitation, circular accelerators started to grow diametrically in size [26].

When a relativistic charged particle, or bunch of particles, changes its direction, it emits electromagnetic radiation, with the features of a "search light", because this radiation is highly collimated in the forward direction although it is broadband. This is illustrated in Figure 2.2. The short pulse indicates to the observer the presence of synchrotron radiation. The corresponding broadband spectrum is characterized by the critical photon energy. This energy depends solely on the particle's energy and its bending radius as shown in Eq. 2.2, where ε_c denotes the critical photon energy, ω_c the critical photon angular frequency, E the particle's energy, m_e its mass, and ρ its bending radius [26].

$$\varepsilon_c = \hbar\omega_c = \frac{3\hbar c}{2(m_e c^2)^3}\frac{E^3}{\rho}. \tag{2.2}$$

There are particular characteristics of synchrotron radiation that depend on the magnetic devices used to generate that radiation, such as wigglers, undulators, wavelength shifters, etc. Nevertheless in this work we are only interested in bending magnets, especially, long high-field superconducting dipoles.

2.2.1 Bending magnets

When a charged particle enters a magnetic field region, the particle is deflected from its original trajectory perpendicularly to the magnetic field. The radius of this deflection depends only on the energy of the particle, its charge and the strength of the field. So we can express the critical photon energy as a function of the particle energy and the magnetic field. The numerical expression for an electron is [26]

$$\varepsilon_c[\text{keV}] = 2.2183\frac{E^3[\text{GeV}^3]}{\rho[\text{m}]} = 0.66503E^2[\text{GeV}^2]B[\text{T}] \; , \tag{2.3}$$

where B is the strength of the field. Sometimes the critical energy required for a given experiment is too high to be reached using regular magnets, or if we have a fixed ρ and try to achieve maximum particle energy, as is the case of the LHC which had to fit in the existing LEP tunnel as mentioned in chapter 3. In these cases regular iron-based electromagnets are replaced with much stronger and shorter superconducting magnets. Conventional bending magnet fields rarely exceed 1.5 or 2 T, but superconducting magnets can be operated at 5 to 6 T, or higher [26]. CERN highest-energy accelerators currently achieve over 8 T and future accelerators are planned to reach twice as much as shown in Table 3.3.

2.2.2 Radiation power

To know the total radiated power we integrate the Poynting vector $\vec{S}$ (from Eq. A.15) over a closed surface that encloses the charge:

$$P = \oint \vec{S} \cdot d\vec{A} \tag{2.4}$$

Doing this we find that the power radiated from a charged particle moving perpendicularly to a magnetic field is proportional to the fourth power of the particle's momentum and inversely proportional to the square of the bending radius [26]. For that reason, a slight increase in energy for a high energy particle leads to a huge increase of power loss due to synchrotron radiation. This is the reason why the highest energy particle accelerators require a very large diameter.

The Liénard formula gives us the instantaneous power radiated by a charge:

$$P = \frac{2}{3}\frac{e^2}{4\pi\epsilon_0 c}\gamma_r^6[\dot{\beta}_r^2 - (\beta_r \times \dot{\beta}_r)^2] \ , \tag{2.5}$$

where β_r is the relativistic velocity and γ_r the relativistic factor. In the case of linear motion, the vector product between velocity and acceleration nullifies, and the formula reduces to

$$P = \frac{2}{3}\frac{e^2}{4\pi\epsilon_0 m_e^2 c}\left(\frac{dp}{dt}\right)^2 \ , \tag{2.6}$$

where p is the momentum and m_e the electron rest mass.

In the case that interests us, namely circular motion, the multiplication becomes the acceleration times the velocity. and we can express the instantaneous power as

$$P = \frac{2}{3}\frac{e^2}{4\pi\epsilon_0 m_e^2 c}\gamma_r^2\left(\frac{dp}{dt}\right)^2 \ . \tag{2.7}$$

Comparing 2.6 and 2.7 we easily see that for the same magnitude of applied force, the power radiated is γ_r^2 times larger if the force is applied orthogonally to the direction of velocity than applied in the direction of velocity.

In accelerator science we are often concerned about the energy loss per turn in a storage ring. This can be expressed as

$$U_0 = \oint \frac{P}{\beta_r c}ds = \frac{2}{3}\frac{e^2}{4\pi\epsilon_0}\beta_r^3\gamma_r^4\oint\frac{ds}{\rho^2}; \tag{2.8}$$

This important formula tells us the minimum RF voltage required in order not to lose the beam. We highlight that the synchrotron radiation emission grows fast, as E^4.

2.2.2.1 Angular and spectral distribution

We are particularly interested in where this energy is deposited. To know this, we take the fraction of energy that passes by a solid angle in the direction of a static observer:

$$\frac{dP}{d\Omega} = (\vec{S} \cdot \vec{n})R^2 = \frac{1}{\mu_0 c}(RE)^2, \tag{2.9}$$

where R is the distance to the observer, and $\vec{(}n)$ is a unit vector pointing towards the observer. And now we put it per unit time of the emitter:

$$\frac{dP}{d\Omega}\frac{dt}{dt'} = \frac{dP}{d\Omega}(1 - \vec{n} \cdot \vec{\beta_r}). \tag{2.10}$$

Introducing Eq. 2.9 into Eq. 2.10 as well as the electrical field for the case of circular motion of a relativistic electrical charge we get:

$$\frac{dP}{d\Omega}\frac{dt}{dt'} = \frac{e^2 c}{2\pi^2 \epsilon_0}\frac{\gamma_r^6}{\rho^2}\left(\frac{1 + 2\gamma_r^2\theta^2(1 - 2\cos^2\phi) + \gamma_r^4\theta^4}{(1 + \gamma_r^2\theta^2)^5}\right), \tag{2.11}$$

where θ is the angle between $\vec{\beta_r}$ and $\vec{n}$, this distribution is highly peaked in the forward direction in a cone defined by γ_r^{-1}.

For spectral distribution we must use the Fourier transform. The total energy radiated per solid angle is the integral of the instantaneous power per solid angle over time:

$$\frac{dW}{d\Omega} = \int \frac{dP}{d\Omega} dt = \frac{1}{\mu_o c}\int (RE)^2 dt. \tag{2.12}$$

We now move to the frequency domain and extract the total energy per solid angle per frequency:

$$\frac{d^2W}{d\omega d\Omega} = \frac{1}{2\pi\mu_0} = \frac{1}{\mu_0 c}\left|\int (RE)e^{i\omega t}dt\right|^2. \tag{2.13}$$

The integral in Eq. 2.13 can be solved analytically, for our case, the case of circular motion, using the Airy integrals or the modified Bessel functions. The answer is:

$$\frac{d^2W}{d\omega d\Omega} = \frac{e^2}{16\pi^3\epsilon_0 c}\gamma_r^2\left(\frac{\omega}{\omega_c}\right)^2(1+\gamma_r^2\theta^2)^2\left[K_{2/3}^2(\xi)+\frac{\gamma_r^2\theta^2}{1+\gamma_r^2\theta^2}K_{1/3}^2(\xi)\right], \tag{2.14}$$

where K are the modified Bessel functions, and θ is the angle in the vertical plane, the term ξ is

$$\xi = \frac{\omega}{\omega_c}\frac{(1+\gamma_r^2\theta^2)^{3/2}}{2},$$

and the critical frequency (ω_c) is:

$$\omega_c = \frac{3}{2}\frac{\gamma_r^3 c}{\rho}.$$

We can see from Eq. 2.14 that the power emitted in the form of high frequency EM waves is negligible, i.e. frequency values greater than the critical energy (ω_c). It is also evident that the power emitted towards large angles θ is negligible, i.e. larger than the critical angle (θ_c): $\theta_c = \frac{1}{\gamma_r}\frac{\omega_c}{\omega}$. Figure 2.3 shows a typical plot describing the behaviour of the spectral distribution of intensity integrated over the vertical angle (θ). The area under the curve is divided roughly in half by a vertical line at $x = 1$.

2.2.2.2 Examples

Using Eq. 2.2 I calculate and present in Tab. 2.1 some relevant examples for critical photon energy in some accelerators. We notice that the critical photon energy for the FCC-hh is over 10 times larger than that for the HE-LHC, eventhough the beam energy and bending radius of the FCC-hh are roughly four times larger than those for the HE-LHC. The reason for this is that ϵ_c depends on the third power of the energy and only inversely on the bending radius. We also notice that the critical photon energy for a proposed Mexican light source is 20 times higher than that for the LHC, eventhough the beam energy of the LHC is over 2400 times higher. The main reason for this is that electrons are much lighter than protons, and the critical photon energy depends on inverse of the third power of the mass

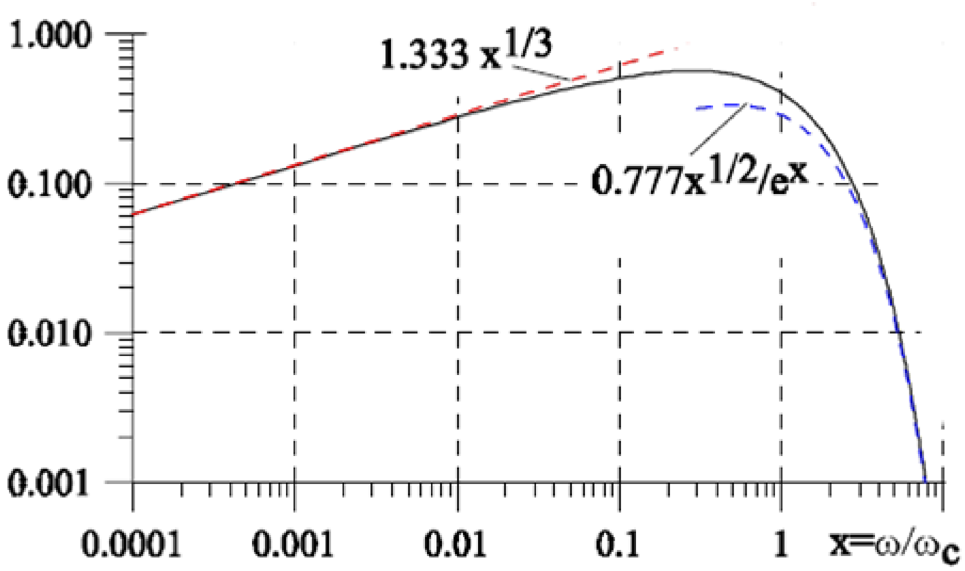

Figure 2.3: Normalized function describing the spectral distribution of intensity integrated over vertical angle (θ). Picture taken from [24].

Table 2.1: Examples of critical photon energy for some accelerators

Accelerator (at top energy)	Critical photon energy (eV)
LHC	44
HL-LHC	44
HE-LHC	314
FCC-hh	3985
Proposed Mexican light source*	950

* The parameters for a proposal for a Mexican light source where taken from [28]. It considers a bending radius equal to 400 m and a beam energy equal to 3 GeV.

of the particle. For this reason, hadron accelerators below the TeV regime can neglect SR effects.

2.3 Electron cloud due to beam induced SR

When high energy SR photons strike a surface, they are able to set loose electrons out of the surface through the photoelectric effect. These electrons are then attracted by the electric field of a passing proton bunch, they move, finally hit the opposite wall extracting further electrons out of the wall through secondary

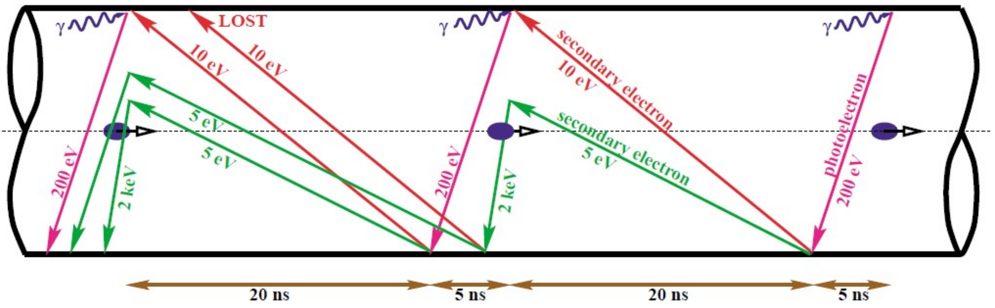

Figure 2.4: Schematic of the formation electron clouds in the LHC. Picture taken from [29].

emission. The latter will be accelerated in the field of the next bunch of protons, etc. This repetitive process can lead to a fast build up of a dense electron cloud inside the vacuum chamber, as is shown in Fig. 2.4. The electron-cloud formation is highly undesirable and accompanied by excessive heat loads, which might no longer be removed from the beam screen.

In order to quantify the photoelectric effect of SR on the wall of the vacuum chamber we first need to express the emitted power in terms of photons. The mean number of emmitted photons per radian, $N_{\gamma,r}$, in a bending magnet or for a full revolution, $N_{\gamma,t}$, are, respectively [24, 30]

$$N_{\gamma,r} = \frac{5}{2\sqrt{3}}\gamma_r\alpha_f, \tag{2.15}$$

$$N_{\gamma,t} = \frac{5\pi}{\sqrt{3}}\gamma_r\alpha_f \ , \tag{2.16}$$

Where α_f designates the fine structure constant ($\approx 137^{-1}$). Importantly, the quantities $N_{\gamma,r}$ and $N_{\gamma,t}$ depend only on the energy of the particle.

Various effects of the electron clouds and possible mitigation methods have been studied at CERN since 1997 [31–34].

Chapter 3

CERN Highest Energy Circular Hadron Colliders

In Chapter 1 I gave a brief history of accelerators which led us to the development of the highest energy accelerators. We now take a deeper look at CERN highest energy hadron colliders, currently in operation and under design. It was for these accelerators that my research was conducted. Figure 3.1a shows a time line illustrating the periods of design, prototyping, construction, and physics exploitation of LEP, LHC, HL-LHC and FCC studies.

3.1 LHC

The Large Hadron Collider (LHC) at CERN is a wonder of engineering and technology. It lies inside a 26.7 Km circular tunnel and 100 meters under the ground. Its construction took over 15 years, involved engineers from all over the world and cost over 6.5 billion CHF. Inside the tunnel there are two counter-rotating hadron beams accelerated to energies up to 7 TeV each. These two beams are then forced to collide inside four huge detectors, that measure the products of the collision [35].

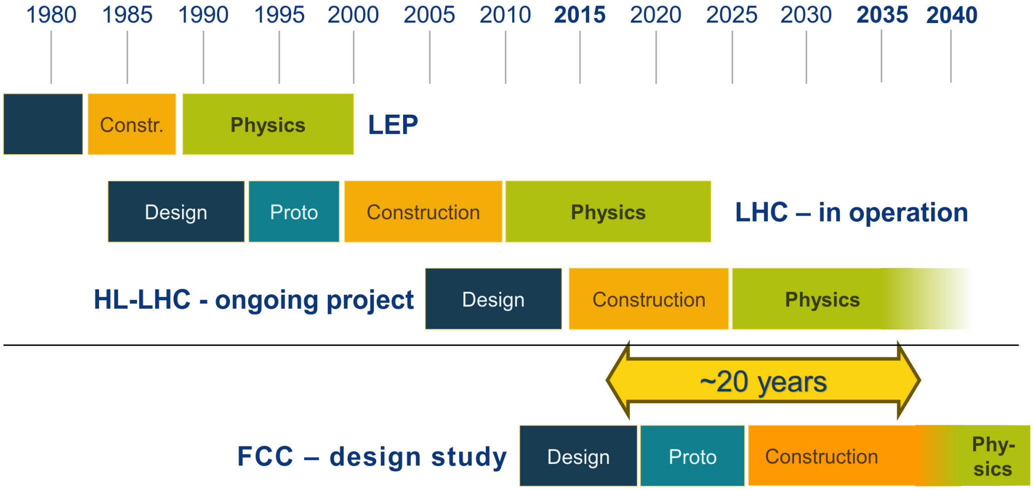

(A) Time lines of some past, present and future circular colliders at CERN, distinguishing periods of design, prototyping, construction, and physics exploitation. Picture courtesy of CERN.

3.1.1 Characteristics

The 26,659 m tunnel used by the LHC was inherited from the previous Large Electron-Positron collider (LEP), when the latter had been shut down. The basic tunnel layout consists of eight long straight sections and eight bending arcs [36]. In order to keep the 7 TeV proton beams on such a small orbit it was necessary to use 1,232 magnets with a 8.3 T field, and a length of 14.3 m each [37]. To achieve this, powerful high-field superconducting magnets are used. For the LHC, as for all previous superconducting hadron colliders, the magnets are made from Nb-Ti superconductor. For efficient cooling and highest field, the specific approach of the LHC was, and still is, to keep the magnets submerged in superfluid Helium below 2 K [36], while previous hadron colliders had operated magnets at temperatures around 4.5 K.

The basic layout of the LHC is sketched in Fig. 3.2, where Beam 1 is shown in blue and circulates clockwise; and in red Beam 2 which rotates counterclockwise. There are four intersections, one in each major experiment: ATLAS, CMS, LHC-b, and ALICE. The first two, ATLAS and CMS, are high luminosity experiments and are located diametrically opposite to each other, while LHC-b is devoted to b-quark experiments, and ALICE, standing for A Large Ion Collider Experiment, studies

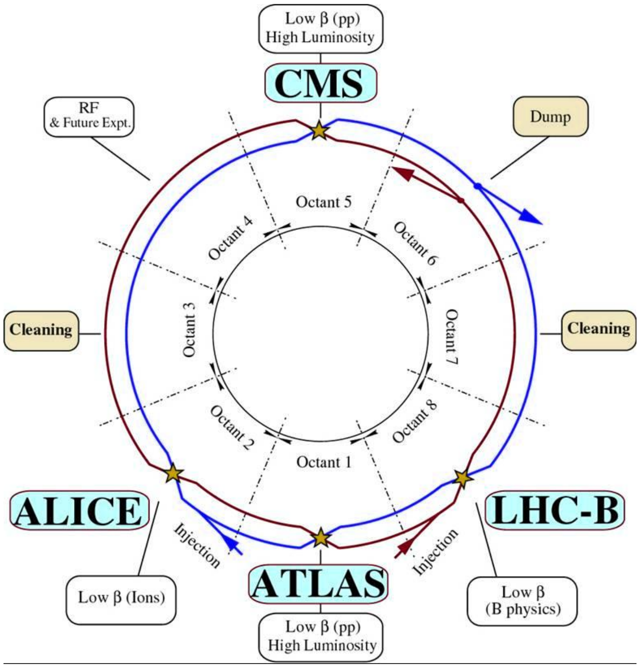

Figure 3.2: General schematic for the LHC.
Picture courtesy of CERN.

collisions of fully stripped Pb ions. The LHC consists of 8 arcs and 8 straight section and it is divided in octants, that start at the center of on arc and end at the center of the next one [37].

one [37]. The main LHC parameters for operation at top energy are listed in Tab. 3.1.

3.1.2 Optics

The LHC optics design allows an optics matching with fixed and equal phase advances over the insertion regions for both beams that does not perturb the optics in the rest of the machine. The total number of particle trajectory oscillations during one revolution in the storage ring of the machine is adjusted by the optics of the arc cell. The flexibility of the phase advance over the insertions provides a measure for the flexibility of the total LHC optics and tell us how much liberty we have to change the phase advance between the main experimental insertions [37].

Table 3.1: Main parameters for proton-proton collisions

Energy	7 TeV
Dipole Field	8.33 T
Coil aperture	56 mm
Luminosity	10^{34} s^{-1} cm^{-2}
Injection energy	450 GeV
Circulating current/beam	0.56 A
Bunch spacing	25 ns
Particles/bunch	1.1×10^{11}
Stored beam energy	350 MJ
Normalized trasverse rms emittance	3.75 μm
Rms bunch length	0.075 m
Beam lifetime	22 h
Luminosity lifetime	10 h
Energy loss/turn	6.7 keV
Critical photon energy	45 eV
Linear photon flux	1×10^{17} $m^{-1}s^{-1}$
Total radiated power/beam	3.8 kW

* This table was taken from "the LHC vacuum system", p. 292 [38].

3.1.2.1 Arc cells

The arcs consist of 23 regular arc cells. These are made out of two 53.45 m long half cells each of which consist of one cold mass with a length of 5.355 m (inside a 6.63 m long cryostat), a so-called short straight section (SSS) assembly, and three 14.3 m long dipole magnets. The optics of Beam 1 and Beam 2 are coupled by electrical connections of the main magnets. There is also a dispersion suppressor at every transition between arcs and straight sections. The arc cells emulate a FODO lattice [37], as described in Sec. A.6.3.1.

3.1.3 LHC Beam Pipe

Because of the high beam intensities needed to reach the high target luminosity, as shown in Table 3.1, the LHC cannot work the same way as the Tevatron, which collided protons with (lower-intensity) antiprotons and used a single vacuum chamber and one set of magnets for both beams. Conversely, for higher-intensity proton-proton collisions, the LHC requires a vacuum chamber for each beam and dipole magnets with opposite bending field in the two apertures, and the beams only share a common beam pipe around the regions where the collisions take place over a length of around 130 m long [37]. On one hand we have the price of the magnets and on the other hand we have the problem that there is not enough space in the LEP tunnel for two sets of magnets. As a result the LHC was built with dual-aperture twin-bore magnets constructed from two sets of coils and beam channels within the same mechanical structure and cryostat [37].

Around 90% of the surface of the LHC vacuum chamber, especially inside the superconducting magnets, should be maintained below 20 K and is made of copper cladded stainless steel in order to reduce Ohmic resistance. The rest can stay at room temperature and is made of thick copper beam pipe [37].

The cold LHC beam pipe comprises a special “beam screen”, held at a temperature of 5–20 K, i.e. higher than the 1.9 K of the cold bore, for better Carnot cooling efficiency. This cooled screen is intended to intercept the heat load of SR and electron clouds, in order to prevent the magnets from heating and “quenching”, which is an unwanted transiting into the normal-conducting state. Figure 3.3 shows the conceptual design of the LHC beam screen [37, 38]. The manufacturing process of the beam screen starts by co-laminating a specially developed low permeability 1 mm thick austenitic stainless steel strip with a 75 μm copper sheet, and then imprinting (rolling) a “saw-tooth structure” on the horizontally outward side of the chamber, where SR photons first impinge. The purpose of the sawtooth is to intercept photons at quasi-normal incidence, thereby minimizing the probability of photon reflection. Inside a dipole magnet, photoelectrons generated in the region of the sawtooth are trapped by the strong vertical magnetic field, therefore cannot be accelerated in the field of the passign bunches, and cannot approach the proton beam at the centre of the vacuum chamber. Such photoelectrons do not contribute to electron-cloud formation or heat load. The beam-screen “pumping slots” are punched into this composite strip, which is then rolled into its final shape and closed by a longitudinal weld [38]. Molecules passing through the pumping slots can get stuck on the cold bore of the magnets (so-called cryo-pumping), ensuring an excellent low vacuum pressure.

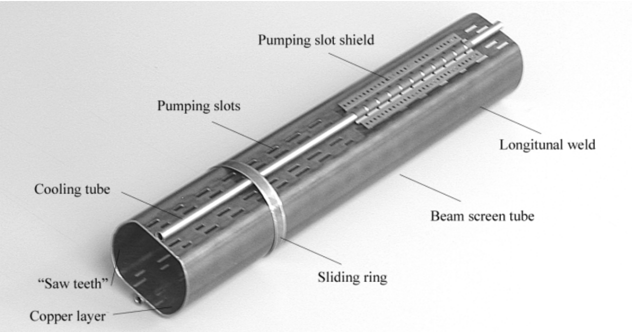

FIGURE 3.3: LHC Beam Screen
Picture courtesy of CERN.

Some example reflection probabilities for an LHC like chamber surface with a 10 nm thick carbon layer on top of copper are presented in Fig. 3.4.. The carbon layer models the effect of the surface conditioning due to electron bombardment ("electron-cloud scrubbing") [39]. For 7 TeV beam energy, the critical photon energy for LHC proton sycnhrotroan radiation is about 44 eV.

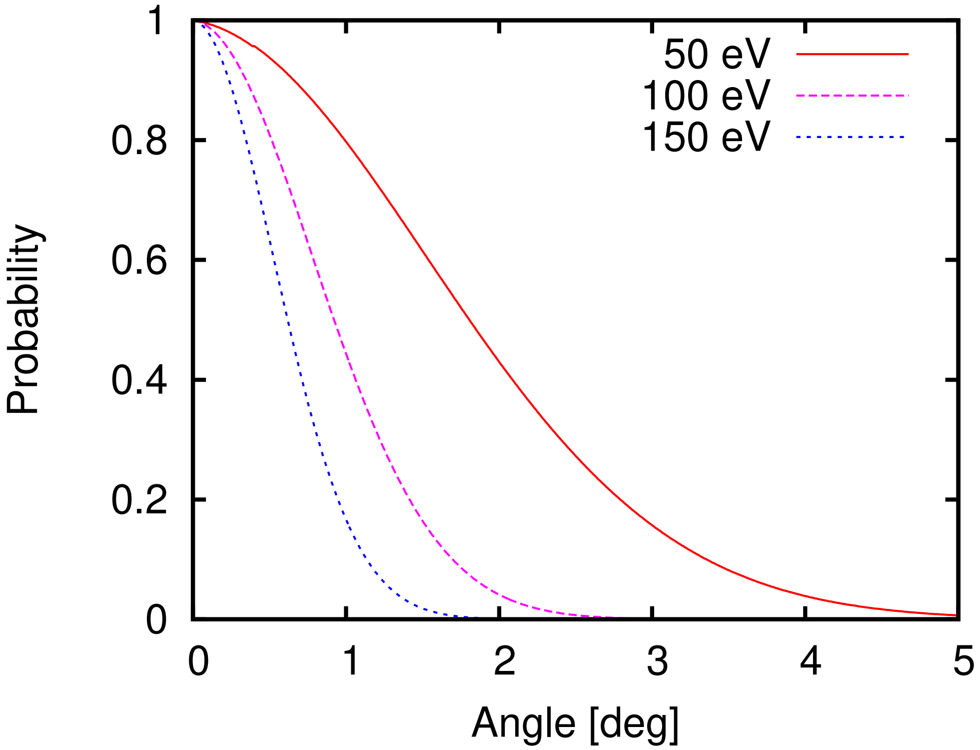

FIGURE 3.4: Photon reflectivity as a function of angle of incidence for three different photon energies, considering a 10 nm carbon layer on top of a copper surface.

3.1.3.1 Sawtooth

To reduce the photon reflection the inner surface of the beam screen, on the horizontally outward side, features a sawtooth pattern, which should ensure almost perpendicular impact of the photons and, thereby, minmize the photon reflection. The sawtooth has longitudinal period of about 500 μm and a horizontal amplitude around 35 μm. The vertical extent of the sawtooth pattern is ± 7.5 mm from the equatorial plane [40].

3.1.4 Cryogenics

The LHC uses cryomodules that are cooled with liquid helium. Each module loses 150 W of heat statically, in addition to the dynamic losses, which span from 100 W to 800 W, depending on the mode of operation. For operation at nominal field the pressure inside the helium tank has to be carefully controlled to avoid frequency variations of the cavity [37].

3.1.5 Synchrotron radiation

The LHC is the first proton collider for which SR is significant. At its highest beam energies, SR gives rise to an important heat load on the LHC beam screen [37], as already mentioned in Sec, 3.1.3. Table 3.2 shows that each beam produces an average of 6.8×10^{16} photons per metre per second in the arcs, which corresponds to a total of 3886 W per beam. So the SR power per metre per bending-length and per beam is 220 mW/m, remebering from Sec. 3.1.1 there are 1232 bending magnets, 14.3 m long each.

3.2 HL-LHC

The High Luminosity (HL) LHC is an upgrade of the current accelerator. Studied since the year 2000, the HL-LHC project implementation began in 2011. It will

Table 3.2: SR Parameters

Parameter	450 Mev	7 TeV
Total power/beam	0.066 W	3886 W
Energy loss per turn	0.11 eV	6.7 keV
average photon flux per metre and second	0.4×10^{16}	6.8×10^{16}
Photon critical energy	0.01 eV	43.13 eV
Longit. emittance damping time	5.5 yr	12.9 h
Trans. emittance damping time	11 yr	26 h

* This table was taken from the "LHC Design Report", p. 108 [37].

require a replacement of over 1.2 km of the current machine. This upgrade should allow us to achieve an integrated luminosity a factor ten times larger than the LHC nominal value.

The instantaneous luminosity ($\mathcal{L}$) is the ratio of the number of events detected (N) in a certain time interval (t) to the interaction cross-section (σ_p),

$$\frac{dN}{dt} = \mathcal{L} \cdot \sigma_p \tag{3.1}$$

The integrated luminosity is the time integral over $\mathcal{L}$ over a given period of time; e.g. one year of running or the luminosity accumulated over the full lifetime of the accelerator. With this improved luminosity the probability of making new discoveries is increased and the maximum energy reach for discoveries is extended. The way to raise the luminosity is to further increase the beam intensity (through an upgrade of the LHC injector chain), and to further squeeze the beam in the interaction regions (IR). The way to improve the squeeze is explained in Sec. 3.2.2.

In June 2018 the civil-engineering work for the HL-LHC began, and by 2026 the upgrade should be fully operational (See Fig. 3.1a).

3.2.1 Superconductivity

The primary technology of future hadron colliders is high-field magnets, both dipoles and quadrupoles. Magnets made from Nb-Ti superconductor were the core technology of the present LHC. Nb-Ti magnets are limited to maximum fields of about 8 T. The HL-LHC will use, for the first time in a collider, some tens of dipole and quadrupole magnets with a peak field of 11–12 T, based on a new high-field magnet technology using Nb_3Sn superconductor.

3.2.2 ATS

Aside from an almost two times higher beam current in the arcs, the main difference between LHC [2] and HL-LHC [41] relevant to our studies, is a beta wave introduced through the long adjacent arcs, required to squeeze the β^* at the primary two collision points, while still correcting the collider chromaticity in spite of a limited strength of the arc sextupole magnets. This optics scheme is called the achromatic telescopic squeeze (ATS) [42]. It exists in round ($\beta_x^* = \beta_y^*$) and flat configurations ($\beta_x^* \gg \beta_y^*$). With a large vertical beta beat in the LHC arcs '45' and '56', the distribution of photons hitting the chamber wall (and being absorbed there) might change. For example, in the "pre-squeeze" optics with a $\beta_{x,y}^* = 0.44$ m, the minimum beta function in the arc is 32 m, whereas for a non-baseline flat ATS optics with $\beta_y^* = 0.05$ m in IP5 [43], the minimum vertical beta function shrinks to $\beta_{y,\min} \approx 16$ m in arcs '45' and '56'. This is to be contrasted with the baseline flat ATS optics which has a vertical beta function in IP5 of 0.075 m [44].

For a full description of the updated ATS optics, we refer to [45].

3.3 FCC Studies

As of June 2018, 129 institutions from 34 countries are collaborating to design the most ambitious accelerator complex ever conceived in history, under the umbrella of the Future Circular Collider (FCC) study. The FCC accelerators could shed new light on many of the outstanding questions of high-energy physics. For a full description of the physics reach, in particular the FCC studies of Higgs physics and electro-weak (EW) symmetry breaking see, e.g., Ref. [46].

The center-of-mass energy reach of a hadron collider is directly proportional to the maximum magnetic field B and to the bending radius, ρ [47].

$$E_{CoM} =\propto \rho B \ . \tag{3.2}$$

So in order to increase our E_{CoM} to 100 TeV, taking the LHC as a reference, the FCC aims at increasing the bending radius by about a factor four and the magnetic field by a factor 2 [48]. The new Nb_3Sn magnet technology which will be used for a few magnets of the HL-LHC 3.2.1, at a field of 11–12 T, will prepare the ground for the development of 16 Tesla Nb_3Sn magnets, and the later production of about 5000 Nb_3Sn magnets required by the FCC-hh.

3.3.1 HE-LHC

A possible intermediate step before, or an alternative to, building an almost 100 km tunnel is to reuse, again, the LEP tunnel. This time we would install an even stronger accelerator than the LHC, and, thereby, test most of the technology that, if successful, would make FCC-hh feasible. This accelerator is the High-Energy LHC (HE-LHC)

3.3.1.1 Parameters

The HE-LHC shall provide proton-proton collisions at an energy of about 27 TeV in the center of mass. Its integrated luminosity should exceed 10 ab^{-1} over 20 years of operation. The HE-LHC will employ FCC dipole magnets with a field of 16 T [48, 85]. The expected photon flux and synchrotron radiation power are 5–20 times higher than for the LHC. The FCC-hh beam screen design [49] offers an adequate solution, with high pumping capacity, low impedance, and a good Carnot efficiency. The HE-LHC also incorporates novel elements from the HL-LHC [50, 86], such as crab cavities and low-impedance collimators.

The HE-LHC could accommodate two high-luminosity interaction-points (IPs) 1 and 5, at the locations of the present ATLAS and CMS experiments. IPs 2 and 8 might host secondary experiments (or a lepton-hadron collision point) combined with injection, as for the LHC.

Following the LHC injector upgrade (LIU) [87], in 2020, a brighter proton beam will be available. Injection into the HE-LHC could be accomplished from the present SPS at 450 GeV, from a new fast ramping single-layer coil superconducting (SC) synchrotron in the SPS tunnel at 900 GeV [88], or from a double-layer coil SC synchrotron at 1.3 TeV [88, 89].

The HE-LHC itself must fit into the existing LHC tunnel with a typical diameter of 3.8 m. Therefore, the outer diameter of its dipole magnets is restricted to 1.2 m, while half sector cooling reduces the size of the cryogenics lines. Overall, the HE-LHC will need up to eight new cryoplants, each with 1.5 times the capacity of one of the existing eight LHC plants, and additional plants at 1.8 K. Two new underground cubes (10 m sides) are required at IPs 3 and 7.

The HE-LHC baseline design parameters are summarized in Table 3.3, which also presents a comparison with the corresponding values for LHC, HL-LHC and FCC-hh [90], which is described in Sec. 3.3.3.

3.3.1.2 Optics

The choice of the HE-LHC arc optics will be a compromise between maximizing the energy reach (favoring fewer and longer cells) and allowing injection from the existing SPS (calling for a larger number of shorter cells). Exploring the parameter space, we are considering two alternative arc optics: The first one, denoted "18 × 90", features 18 FODO cells per arc and 90 degree phase advance per cell. The second optics, referred to as "23 × 90", consists of 23 cells per arc, similar to the present LHC optics. Both optics follow the footprints of LEP and LHC, to within a few centimetres. Tab. 3.4 compiles key parameters. At 450 GeV, for the 23 × 90 optics the minimum physical aperture in every regular arc cell is about

Table 3.3: Key parameters of HE-LHC compared with FCC-hh, HL-LHC [93] and LHC [94], for operation with proton beams. All values, except for the injection energy, refer to collision energy. HE-LHC entries shown in parentheses refer to a larger crossing angle; LHC entries in parentheses to the HL-LHC. The bunch spacing is 25 ns for all colliders.

parameter	unit	FCC-hh		HE-LHC	(HL-)LHC
centre-of-mass energy	TeV	100		27	14
injection energy	TeV	3.3		0.45/0.9/1.3	0.45
arc dipole field	T	16		16	8.33
circumference	km	97.8		26.7	26.7
beam current	A	0.5		1.12	(1.12) 0.58
bunch population N_b	10^{11}	1.0		2.2	(2.2) 1.15
longitudinal emittance ($\sim 4\pi\sigma_z\sigma_E$)	eVs	5		4.2	2.5
norm. transv. rms emittance $\gamma\varepsilon$	μm	2.2		2.5	(2.5) 3.75
IP beta function $\beta^*_{x,y}$	m	1.1	0.3	0.25	(0.15) 0.55
peak luminosity per IP	10^{34} cm^{-2}s^{-1}	5	30	28	(5, leveled) 1
peak no. of events per crossing	—	170	1000	800	(132) 27
SR power / beam	kW	2400		100	(7.3) 3.6
transversal emittance damping time τ	h	1.1		3.6	25.8
initial proton burn-off time τ_{bo}	h	17	3.4	2.5	(15) 40
luminosity per year (160 days)	fb^{-1}	≥ 250	≥ 1000	730	(250) 55

9.5 σ, for the 18 × 90 optics only 7.2 σ [95], using the parameters of [96] and a mechanical tolerance of 1 mm. These numbers are smaller than the minimum aperture of 12.6 σ for the HL-LHC [96]. They might become acceptable with a stricter control of injection oscillations, adequate machine protection measures, and tighter primary collimator settings. For example, above the primary collimators set at 5 σ another 4.5 σ (23×90) or 2.2 σ (18×90) [present LHC: ~9 σ] would be available for preserving the collimator hierarchy between primary, secondary, and dump-protection collimators, and the arc aperture.

The calculated multipole field errors for the Nb_3Sn magnets of the HE-LHC are shown in Table 3.5, which assumes a SC wire filament size of 20 μm. For the

Table 3.4: Arc optics parameters for LHC (scaled to a beam energy of 13.5 TeV) and the two HE-LHC optics designs.

parameter	unit	23×90	18×90
cell length	m	106.9	137.2
quadrupole length	m	3.5	2.8
max., min. beta	m	177, 32	230, 40
max., min. dispersion	m	2.2, 1.1	3.6, 1.8
dipole field for 13.5 TeV	T	16.59	15.83
c.m. energy for 16 T dip.	TeV	26.01	27.28

18×90 optics, including b_3, b_4 and b_5 correctors, the simulated dynamic aperture (10^5 turns, 60 seeds, $\Delta p/p = 0.075\%$) is 4.8 σ at 1.3 TeV, and significantly less at lower energies. For the 23×90 optics, it is 2.8 σ at 450 GeV, 1.0 σ (!) at 900 GeV, and 11.9 σ at 1.3 TeV [95]. At present only this last case looks viable. However, adding artificial pinning centers (APC) and either magnetic iron shims [98] or HTS persistent-current shims [99] could further reduce the field errors [100]. Improved correction schemes may also help.

More details on the arc optics can be found in [101]. An integrated overall HE-LHC optics exists at injection and collision energies [95]. It includes the experimental insertions [102, 103], betatron collimation straight [104], injection and extraction straights [105], and rf straight [106].

Table 3.5: Systematic, uncertainty and random normal sextupole component b_3 in the main arc dipoles, in units of 10^{-4} at a reference radius of 16.7 mm, for three different injection energies, considering a wire with 20 μm filament size and $\pm 5\%$ critical current variation [97].

energy	syst.	uncertainty	random
450 GeV	-35	10	10
900 GeV	-55	4	4
1.3 TeV	-40	3	3

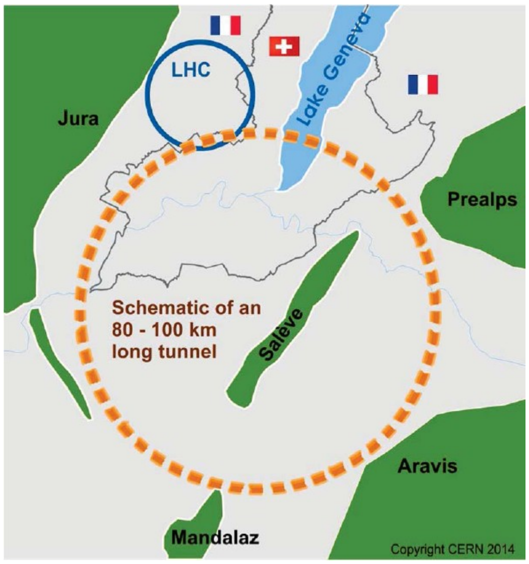

FIGURE 3.5: Schematic of FCC-hh tunnel location. Courtesy of CERN

3.3.2 Beam pipe

Given the dimensions of the dipole gaps, it is imperative to use a smaller beam pipe than the one used in LHC. Over the design period, the main options considered to be used as beam pipes for HE-LHC are: a) a scaled version of the one used for LHC with the same SR mitigation scheme: i.e. a sawtooth pattern on the inner side of the radially outward wall; and b) The same vacuum chamber designed to be used in the FCC-hh. Models of these chambers are displayed in Figs. 5.14, 5.13 and 3.7.

3.3.3 FCC-hh

The ultimate goal of the FCC studies is to construct a 100 TeV E_{CoM} proton-proton collider (FCC-hh). Its circumference would be about 100 km long and would be located more than 100 m underground in the Lake Geneva basin, as shown in Fig. 3.5.

A proton beam could be injected into the FCC-hh from the LHC at a beam energy of 3.3 TeV, a second option is to replace the current SPS with a new fast ramping superconducting synchrotron and to inject at 1.5 TeV.

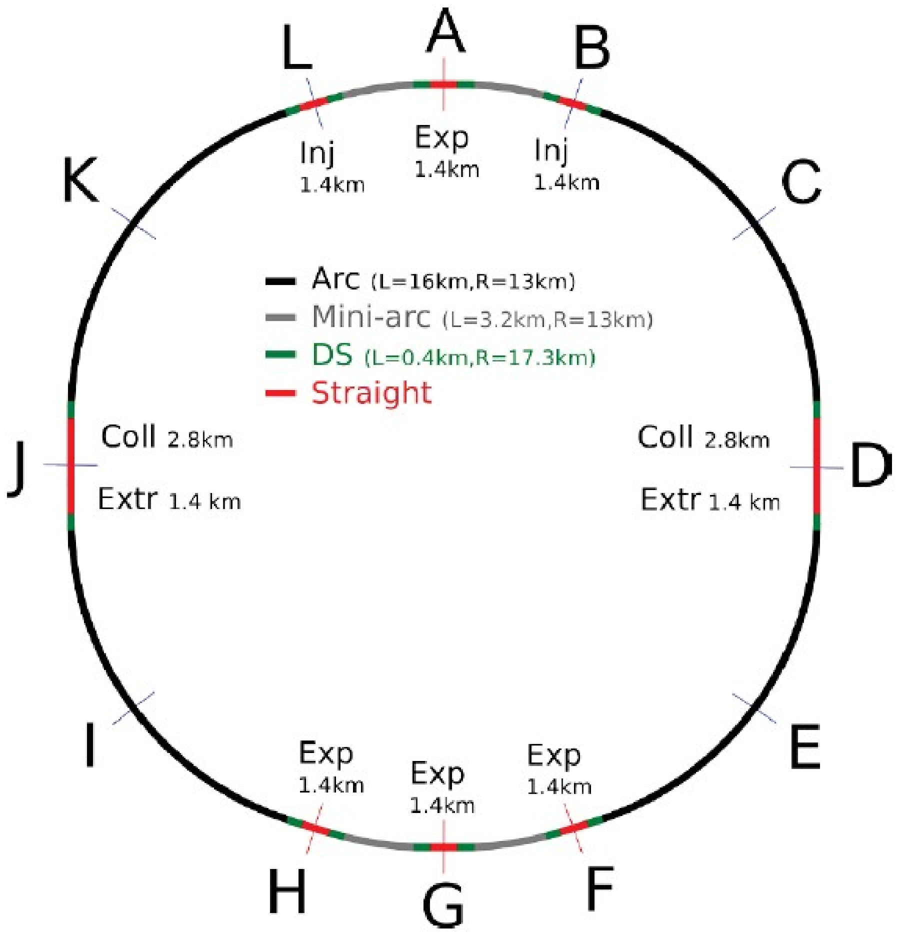

Figure 3.6: Preliminary layout of FCC-hh.

Figure 3.6 shows a preliminary layout for the FCC-hh, which could house four experiments, two high-luminosity experiments at points A and G, and two special detectors at F and H [48].

The SR emitted by the FCC-hh beams will be substantial as shown in Table 3.3. It could be as high as 30 W/m/aperture, more than 100 times higher than for the LHC, which is a dramatic heat load[48] on the beam screen. Depending on the temperature chosen for the cold bore, we could allow the temperature of the beam screen to increase by up to a factor of ten compared to that of the LHC [51].

For our study is also important to notice that the total number of photons emitted per revolution scales in proportion to the beam energy. For the FCC-hh it is a factor of about seven higher than for the LHC, from equation 2.15. A more

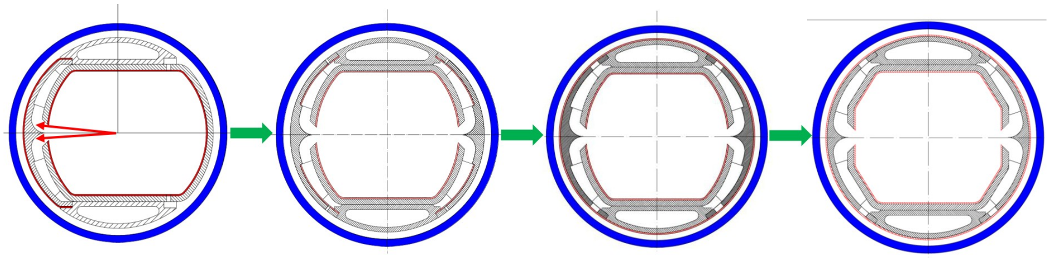

Figure 3.7: Evolution of FCC-hh vacuum chamber design.
(courtesy of C. Garion, CERN).

important difference is the critical photon energy (ϵ_c) which scales as ${\gamma_r}^3/\rho$, and, hence, is a factor 100 higher in the FCC-hh than in the LHC.

3.3.4 Beam pipe

An extremely high power is emitted as SR inside the cold arcs of the FCC-hh, a factor of 666 times the one of LHC, as shown in Table 3.3. To handle this power, the FCC-hh will feature a novel beam-screen, which includes integrated ante-chambers whose purpose is to absorb SR photons outside the inner vacuum chamber, thereby, facilitating the beam-screen cooling and stabilising the beam vacuum [49, 52] as well as minimising the generation of an electron cloud in the beam pipe proper.

The original design suggested a 3 mm high slot on the radially outward side of the beam pipe. The opening would lead to a circular mirror-like edge deflector which would reflect photons into the ante-chamber. Finally a symmetric design with opening on either side was adopted. Over time it has been further modified, The most relevant changes to our research is the expansion of the slot height, to 5 mm at first, and then to 7 mm. Another recent change is the replacement of the deflector by a a sawtooth surface. Figure 3.7 shows the evolution of the design of the vacuum chamber, and Figs. 3.8a and 3.8b show the latest versions which no longer feature the deflector. The deflector presented difficulties in the manufacture process and had issues at its tip.

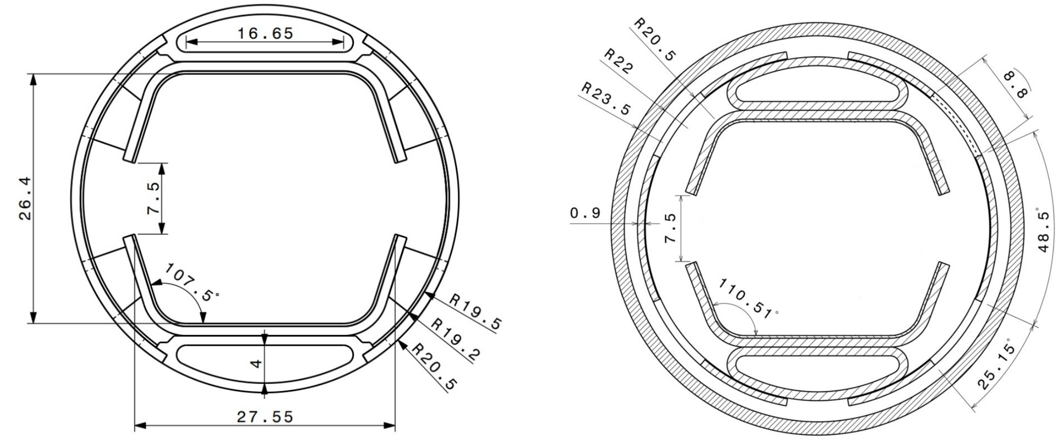

(A) Model of the FCC-hh vacuum chamber in 2017.

(B) Model of the FCC-hh vacuum chamber in 2018.

FIGURE 3.8: FCC-hh vacumm chamber models
(Courtesy of I. Bellafont, ALBA).

Chapter 4

Software

This chapter is devoted to show the main computational tools I used for my simulations. Section 4.2 explains the main tool and it is based in its manual [53]. The subsequent sections show other more generic tools. And finally we validate the code by benchmarking it with a second independent code and with experimental data.

4.1 Bmad

Bmad, which was build in 1996 at Cornell University's Laboratory for Elementary Particles Physics, is a subroutine library for relativistic charged particles and X-Ray simulations in high energy accelerators and storage rings. The Bmad subroutines are programmed in an object oriented approach and are written in Fortran90. The main objectives of this project were:

- Cut down on the time needed to develop programs.
- Minimize computation times.
- Cut down on programming errors,

- Provide a simple mechanism for lattice function calculations from within control system programs.
- Provide a flexible and powerful lattice input format.
- Standardize the sharing of lattice information between programs.

Bmad's diverse routines are capable of doing many things, such as simulating wake fields and radiation stimulation, calculating transfer matrices, emittances, Twiss parameters, dispersion, coupling, etc., and they include various tracking algorithms including Runge-Kutta and symplectic integration.

We are particularly interested in a set of routines used to build a program called `Synrad3D`, which is employed to track both produced and scattered photons from SR in a high energy machine. This particular program is described in Sec. 4.2.

4.2 Introduction to Synrad3d

`Synrad3D` is a program constructed upon the beam-optics code Bmad. It was written by David Sagan using a photon scattering model developed by Gerry Dugan, both of them from Cornell University.

`Synrad3D` simulates the production and scattering of synchrotron radiation generated by a beam of charged particles in a high energy machine [53]. The `Synrad3D` program uses the Monte Carlo method for photon generation, scattering, and absorption calculations.

4.2.1 Physics of Synrad3d

The following description of the `Synrad3D` calculation recipe is based on Ref. [53].

To generate photons, a section of the machine is designated. The user sets the total number of photons to be generated. `Synrad3D` calculates how many photons need to be generated within each machine element. The local bending field at the beam orbit is used to determine the photon spectrum.

Each photon is tracked from the point of origin to the point at which it hits the vacuum chamber wall. The angle of incidence relative to the local normal to the vacuum chamber is computed. The scattering probability is calculated, using this angle and the photon's energy. Using the value of this probability, the photon is either absorbed at this location, or scattered. If it is scattered, the scattering is taken to be elastic. That is, photon energy does not change. This ignores any fluorescence. Surface roughness, on the other hand is taken into account, so that there is a diffuse component of the photon scattering, in addition to specular reflection. Then the photon is tracked to the next hit on the vacuum chamber wall, and the probability of scattering is computed again. This process goes on until the photon is absorbed.

4.2.1.1 Photon Generation

Photon generation is based on the standard synchrotron radiation formulas, applicable for dipoles, quadrupoles, and wigglers. The radiation is assumed to be incoherent.

`Synrad3D` slices up each element longitudinally and generates photons from each slice. The number of photons generated in a slice is weighted by the local probability of photon emission which depends on the local orbit curvature.

Both circular and "linear" (that is, non-circular) machines can be simulated. In both cases, the orbit of the charged particle beam, which may be non-zero, sets the centroid position and angular orientation of the generated photons. Photon generation is based upon the local field along the beam orbit. Thus, for example, off-axis charged particles in a quadrupole will produce radiation. The beam orbit is calculated from such things as the settings of steering elements, element misalignments, etc. as given in the lattice file. For circular machines, the beam orbit is the closed orbit. For linear machines, the starting beam position as set in the lattice file is used in the orbit calculation.

When a photon is generated at a given longitudinal position, the beam emittances and centroid positions are used, so that the resulting photon distribution mirrors the Gaussian positional and angular distribution of the beam. Horizontal/vertical coupling is taken into account in this calculation. The photon energy distribution is the standard energy spectrum of photons generated in a bend.

A photon's initial angular orientation is generated by, first, using a random number generator to generate an angular orientation based on a probability function that corresponds to the beam's angular distribution. To this orientation, an angular offset out of the plane of the bend is added, where this offset is calculated using a random number generator with a probability distribution based on the standard angular spectrum of photons generated in a bend. No angular offset is added to the angle in the plane of the bend. The generated photons will have the proper correlation between photon energy and photon angle. Note that the plane of the bend may not be horizontal. For example, the bend plane orientation for an offset beam in a quadrupole will depend upon the offset.

4.2.1.2 Photon scattering

Simulated photons are tracked until they hit the wall, where the probability of being scattered, and the scattering angle, are determined by their energy and angle of incidence. This section describes the scattering model.

Generally, the probability of specular reflection of a photon from a rough surface depends on the the rms surface roughness σ, the photon wavelength λ, and the grazing angle. An explicit formula for this probability is [54]

$$P_{\text{spec}} = \mathrm{e}^{-g(x,y)} \, , \tag{4.1}$$

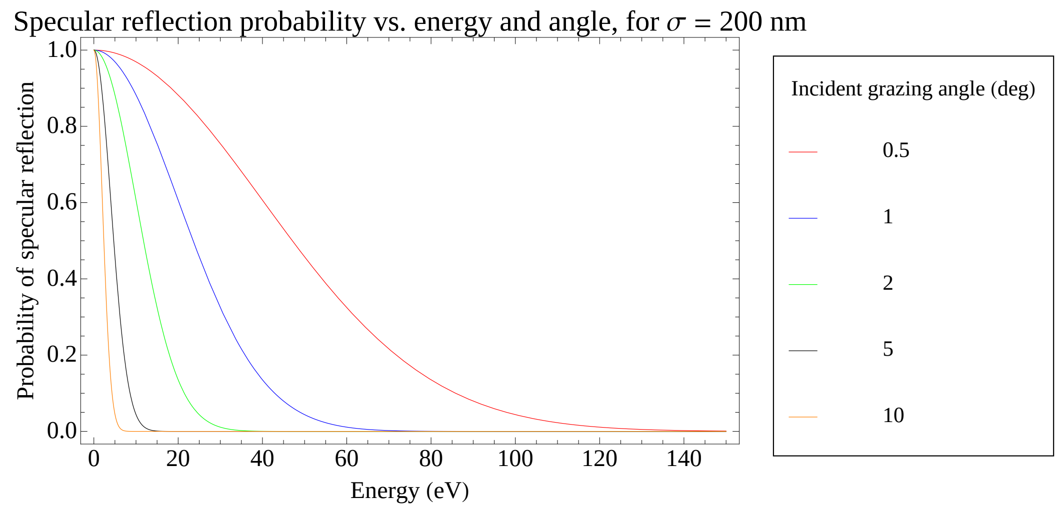

FIGURE 4.1: Specular reflection probability [54], vs. photon energy and angle, for an rms surface roughness of 200 nm. Picture taken from [53].

in which

$$g(x, y) = \frac{4\pi^2\sigma^2(x+y)^2}{\lambda^2} \, , \tag{4.2}$$

where x is the cosine of the incident polar angle, and y is the cosine of the scattered polar angle. For a typical technical vacuum chamber surface, the rms surface roughness $\sigma \gtrsim 200$ nm is greater than most of the X-ray wavelengths of interest, for all except the lowest energy photons. In this regime, except at very small grazing angles, diffuse scattering from the surface dominates over specular reflection. This is illustrated in Fig. 4.1. The theory of diffuse scattering of electromagnetic waves from random rough surfaces is a well-developed subject, and is covered in detail in references [54] and [55]. The model used in `Synrad3D` assumes a Gaussian distribution for both the surface height variations (rms σ) and for the transverse distribution (equal in both transverse directions, with an autocorrelation coefficient T).

The most general expression for the diffusely scattered SR power is complex, and involves an infinite sum. However, the expression simplifies substantially in the limit $g(x, y) \gg 1$. For very rough surfaces corresponding to technical vacuum chambers, for which typically $\sigma \gg \lambda$, this condition is satisfied over much of the region of interest. In this limit, the diffusely scattered power per unit solid angle

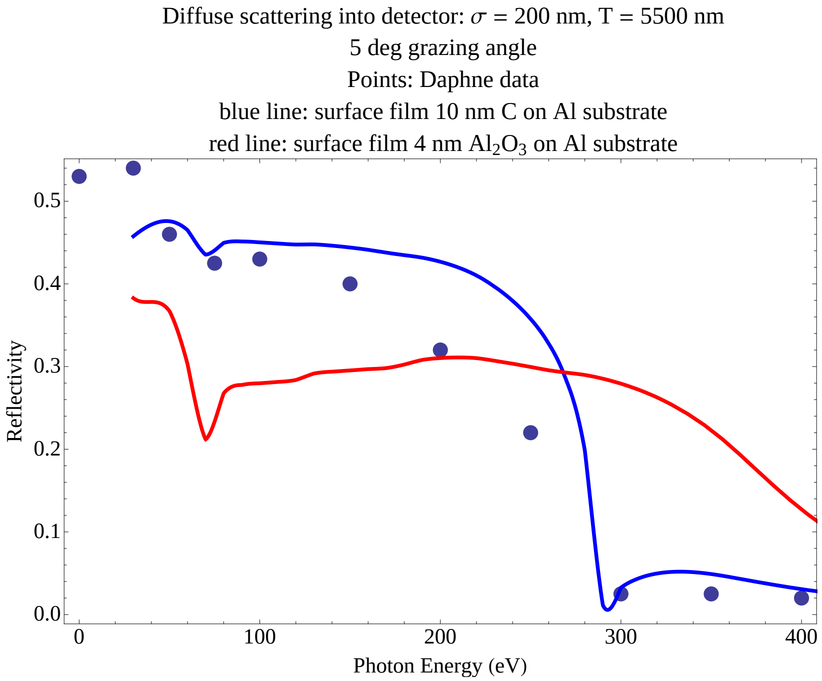

FIGURE 4.2: Diffuse scattering at 5 deg from a surface layer on an aluminium substrate: comparison of data and model. Picture taken from [53].

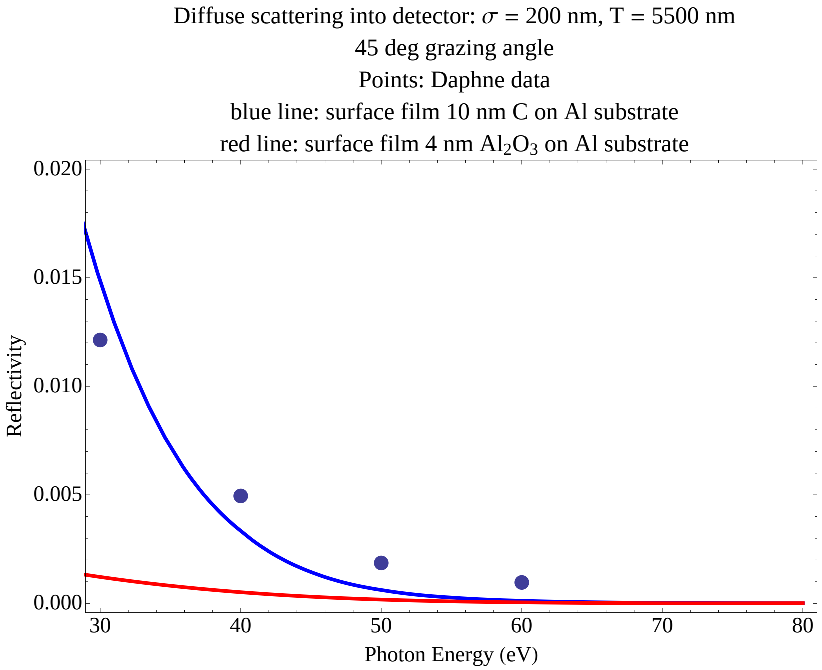

FIGURE 4.3: Diffuse scattering at 45 deg from a surface layer on an aluminium substrate: comparison of data and model. Picture taken from [53].

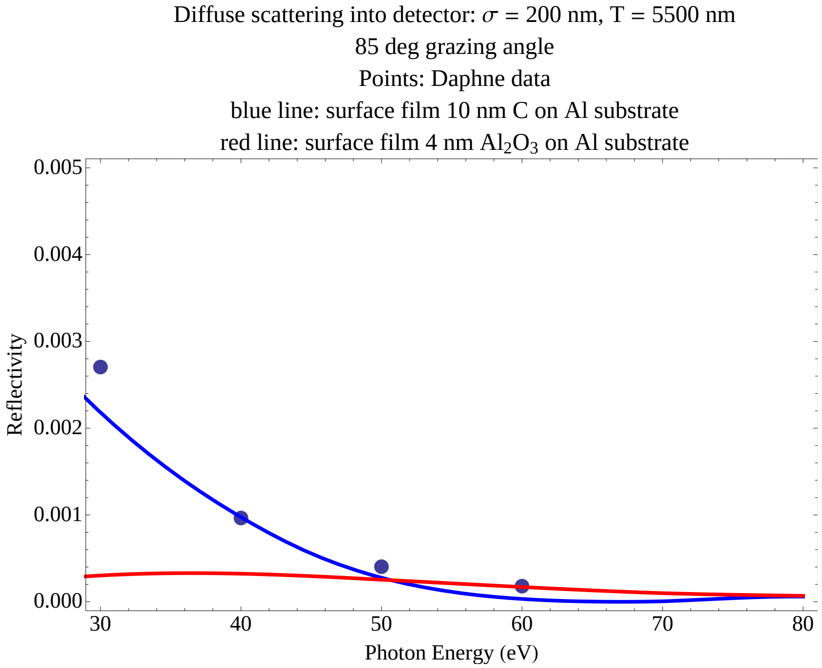

FIGURE 4.4: Diffuse scattering at 85 deg from a surface layer on an aluminium substrate: comparison of data and model. Picture taken from [53].

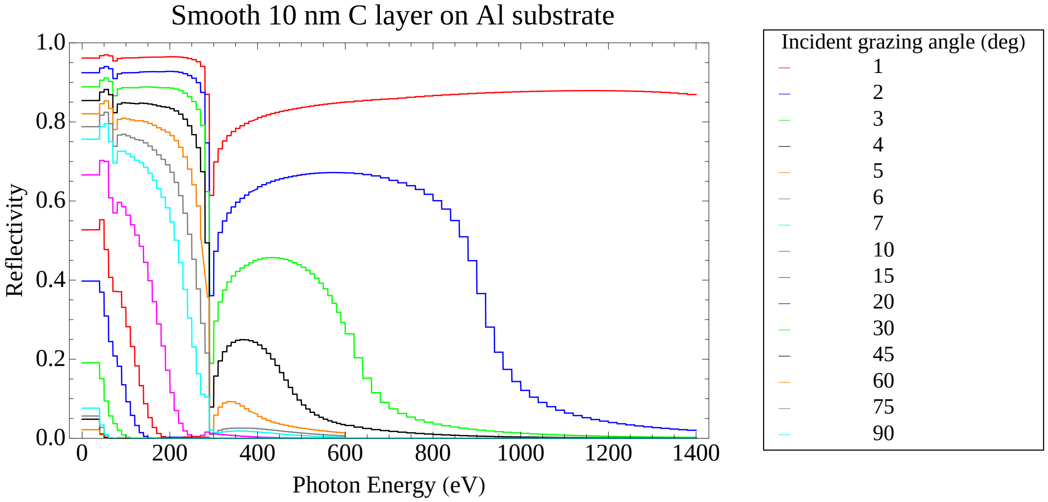

FIGURE 4.5: Smooth surface reflectivity for a 10 nm C film on Al substrate: from Ref. [56]. Picture taken from [53].

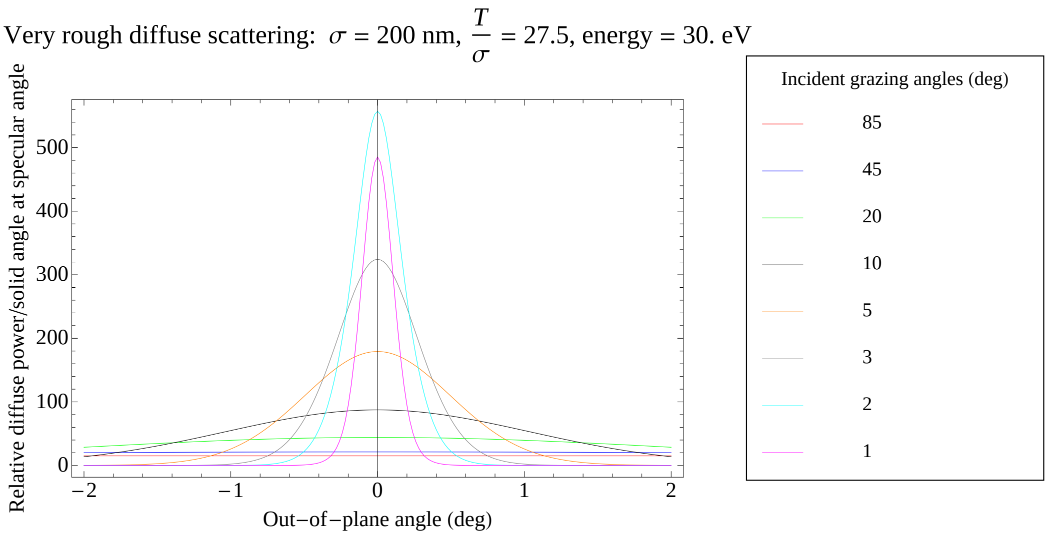

FIGURE 4.6: Diffuse scattering out-of-plane angular distributions for 30 eV photons. Picture taken from [53].

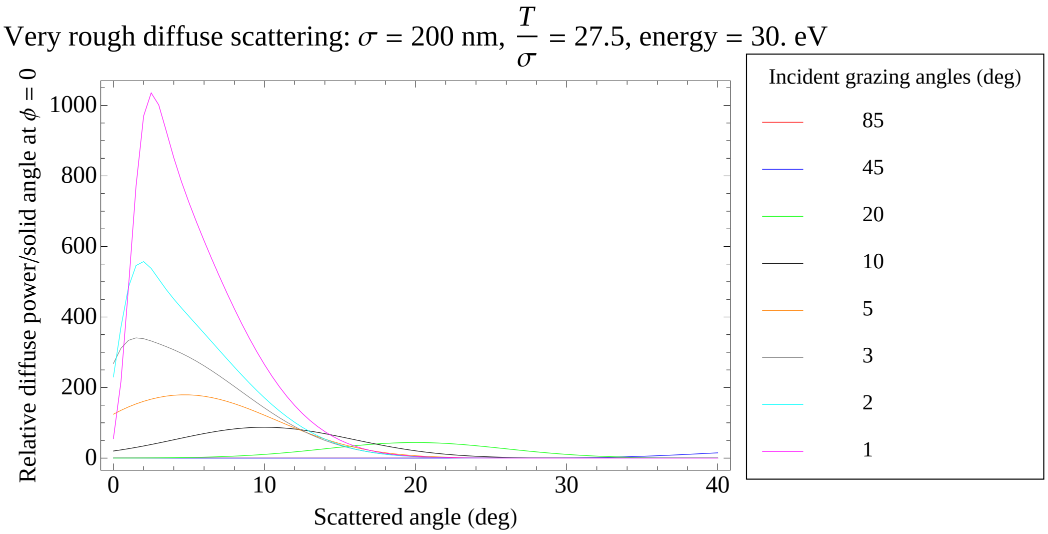

FIGURE 4.7: Diffuse scattering polar angular distributions for 30 eV photons. Picture taken from [53].

is given by

$$\frac{dP_{\text{diff}}}{d\Omega} = P_0 \frac{\langle R\rangle}{4\pi y}\frac{(1+xy)^2}{(x+y)^4}\tau^2 \mathrm{e}^{-\frac{(2-x^2-y^2)\tau^2}{4(x+y)^2}}(1-a\cos\phi)^2 \mathrm{e}^{b\cos\phi}, \tag{4.3}$$

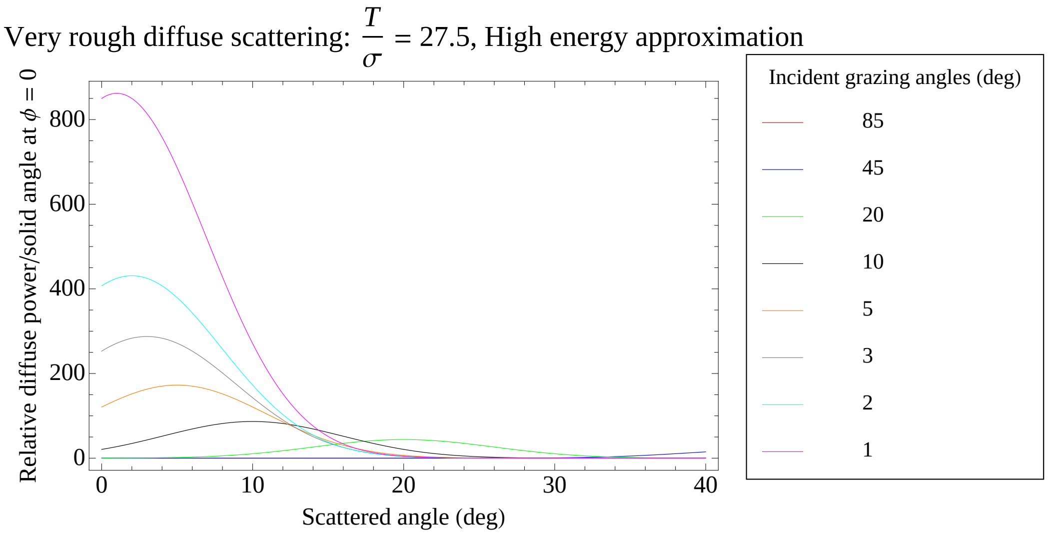

FIGURE 4.8: Diffuse scattering polar angular distributions for high energy photons. Picture taken from [53].

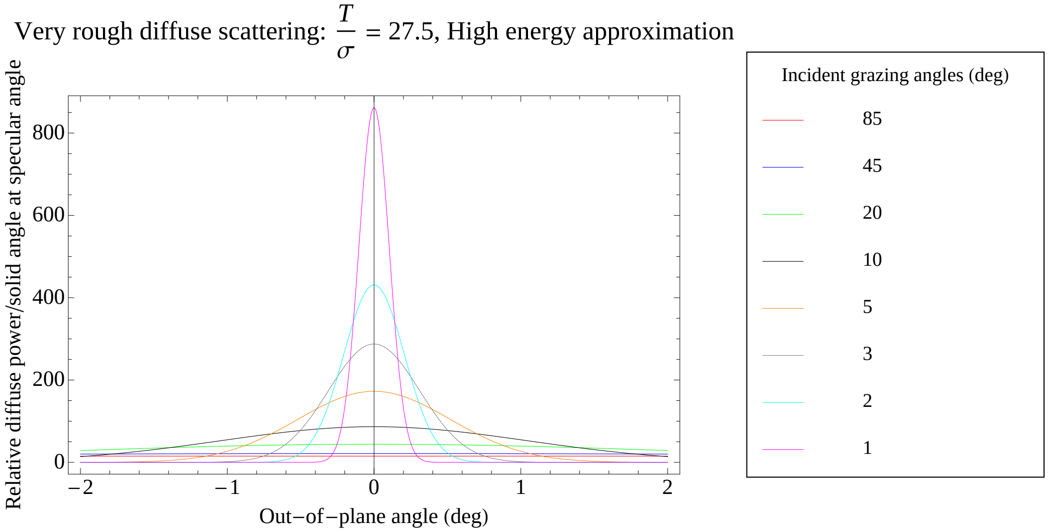

FIGURE 4.9: Diffuse scattering out-of-plane angular distributions for high energy photons. Picture taken from [53].

with

$$a = \frac{h(x,y)}{1+xy}, \tag{4.4}$$

$$b = \frac{2h(x,y)\tau^2}{4(x+y)^2}, \tag{4.5}$$

$$h(x,y) = \sqrt{1-(x^2+y^2)+x^2y^2}\,. \tag{4.6}$$

In this expression, P_0 is the incident power, and $\langle R \rangle$ is the smooth-surface reflectivity, which is determined by the atomic structure of the surface material. ϕ is the scattering angle out of the plane of incidence. Note that the relative power depends only on the ratio $\tau = T/\sigma$, and not on T or σ separately.

The smooth-surface reflectivity $\langle R \rangle$ depends on the atomic structure of the surface materials (including any thin layers which may be deposited on the surface). The surface roughness parameters σ and T depend on the geometry of the surface deviations from a perfect plane. These parameters may be determined from inspection of the vacuum chamber surface, for example, using an atomic force microscope.

To derive a working model for the smooth surface reflectivity and the surface parameters for a typical vacuum chamber surface, we have relied on measurements [57] of X-ray scattering from an aluminium vacuum chamber surface performed at DAPHNE in Italy. For these measurements, the rms surface roughness of the sample was reported to be 200 nm.

The theory of diffuse scattering discussed above has been used, together with smooth surface reflectivity results taken from an X-ray database [56], to predict the scattering and the compare with the measurements. From these comparisons, the best-fit value for the transverse autocorrelation parameter, T, was found to be 5500 nm. In addition, it was found that the smooth-surface reflectivity corresponding to a 10 nm carbon film on an aluminium substrate was needed to fit the data. On the other hand, the assumption of an aluminium oxide surface film was not consistent with the data. The data and the corresponding fits are shown in Figs. 4.2, 4.3, and 4.4.

With the smooth-surface reflectivity known, and the surface parameters established, the scattering model in `Synrad3D` is completely determined. The model currently in use has a smooth-surface reflectivity illustrated in Fig. 4.5. Diffuse scattering distributions for 30 eV photons are shown in Fig. 4.7 and Fig. 4.6. At these low values of photon energy, the approximation $g(x, y) \gg 1$ does not hold in general, and instead the full diffuse scattering formalism is used to compute the corresponding distributions. Diffuse scattering distributions for high energy photons, for which $g(x, y) \gg 1$, are shown in Fig. 4.8 and in Fig. 4.9. These distributions have been computed from Eq. 4.3.

4.2.2 Modeling the diffuse reflection for ultra low σ

The model used by Synrad3D for simulating diffuse reflections was developed by Dugan and Sagan [58]. The model gives the probability $P(x, \phi)$ that a photon scatters diffusely at the reflected polar angle x and azimuthal angle ϕ, as explained in Sec. 4.2.1.

For calculational convenience, instead of working with the probability function $P(x, \phi)$, which is a function of two variables, two one-dimensional probability functions are used. The first function is $P_x(x)$ which is $P(x, \phi)$ integrated over ϕ (Eq. A140 in [58]). For a given scattering event, $P_x(x)$ is first used, with the help of a random number generator, to choose a value for x. After this, the probability function $P(\phi|x)$ which is the probability of scattering at an angle ϕ for a given x is used to choose a value for ϕ.

For a typical technical vacuum chamber surface, the RMS surface roughness is of order $\sigma \sim 200$ nm [58]. Given the low surface roughness used for our simulations ($\sigma = 50$ nm) [59], the probability function $P_x(x)$ becomes highly peaked where the reflected polar angle x equals the incident polar angle. That is, the diffuse reflection distribution resembles the delta function distribution for specular reflections [58]. In prior simulations, a 30^{th} order Chebyshev fit to $P_x(x)$ was used to integrate $P_x(x)$ (the integration is needed to normalise the scattering probability). With the low surface roughness required for LHC simulations, this proved to be a poor fit due to the delta function like nature of $P_x(x)$. To address this issue, the Chebyshev fit was replaced by an adaptive Akima spline fit [60], which better represents extremely peaked functions for a number of reasons. The Akima spline has the advantage of locality in that the calculated slope at a knot point is only affected by the neighbouring knot points. Additionally, the Akima spline does not mandate a continuous second derivative at the knot points. This is an advantage with highly peaked functions since, in this case, there are large changes in the second derivative. Finally, the adaptive point selection places knot points to minimise the estimated error in the integrated area. With a peaked function, more knots will be used near the peak where the second derivative is changing the most. This non-uniform distribution of knots minimises the computation time needed.

4.2.3 Input files

The input files used by `Synrad3D` are the following:

Synrad3d Main Input File (SMIF)

This file should be specified on the command line that invokes `Synrad3D`. If it is not specified, the default name "synrad3d.init" will be selected. This file contains the parameters of the simulation.

- The region where radiation is produced specified by the index numbers of elements in the lattice.
- The direction in which the photons are travelling when initially created.
- The minimum number of photons that need to be generated before `Synrad3D` will stop the simulation.
- The number of photons generated throughout the radiation production region.
- The minimum distance to track the particle beam between emission points.
- The particle beam size.
- The lattice file defining the optics of the accelerator.
- The wall file defining the vacuum chamber's details.

- The name of the output file.
- The surface roughness for the default surface.
- The surface roughness correlation for the default surface.
- The surface reflection file for non-default surface.
- The minimum and maximum initial energy values to be filtered by `Synrad3D`.

There are other parameters that can be specified in the SMIF, but are not mentioned here, because they are not relevant to my work.

Lattice file

This file contains the complete description of the elements of the lattice, defining the optics of the machine. The name of this file must be specified in the SMIF.

Vacuum chamber wall definition

The file specified in the SMIF defines the cross section of the vacuum chamber's wall at a number of longitudinal positions.

Chamber Surface Reflectivity

The reflectivity of the vacuum chamber wall can be described on the surface reflection file specified in the SMIF. If no file is specified `Synrad3D` will use the default reflectivity, which is based on the reflectivity of a Carbon film on Aluminium substrate.

4.2.4 Output files

Synrad3d Main Output File (SMOF)

The name of this file must be specified in the SMIF. This file contains the information in the SMIF and the data generated for each photon. The information of the photon consists in:

- The number of the photon.
- The number of times the photon hit the wall.
- The photon's energy.
- The position where the photon was generated.
- The position where the photon was absorbed.
- The distance travelled by the photon.
- The type of element of the lattice that absorbed the photon.

Once again a couple of elements are left out because they are irrelevant to this thesis work.

Output table

In order to make it easier to read and manipulate the data, the photons information is also written in a table format, which carries the same name as the SMOF, but with the extension .dat_table. In the most recent versions of `Synrad3D` this is not an automatic output.

4.3 Tools

Given the nature of routines described in Sec. 4.2, and the need for using enough photons to obtain statistically valid results, running this program would take months in a regular commercial computer. To surpass this limitation we were grated access to the *Lxplus* computing cluster at CERN.

4.3.1 Lxplus

The Lx Public Login Service or Lxplus is a login service offered to all CERN users. This cluster consists in several public machines running SLC5 in 64 bit mode, where all interactive and batch systems are built on top of the CERN standard Unix/Linux Environment. A wide range of shells are available, that can be sorted in two groups: the C-shell like and the Bourne-shell like grups. We used Bash to maximally profit from the Linux based facilities. Since the Lxplus machines cannot be used to store data, a dedicated work space was created on the AFS file system, that is accessible through normal system commands. Running CPU-intense jobs directly on an Lxplus machine is prohibited.

4.3.2 Lxbatch

To run CPU intense jobs we used Lxbatch that currently consists of around 30,000 CPU cores accessible through the running platform LSF®. This service is open to all CERN users and its aim is to share the resources fairly between all CERN experiments. So the amount of resources we can use depends on how much the other experiments are using. LSF jobs can be sent to different queues. One should select the proper queue according to the processing time the job will require. There are queues covering the range from 8 minutes to 2 weeks. we ran our jobs in the 1 week queue.

4.4 Validation

To validate the used code `Synrad3D`, we followed two steps. First we benchmarked the code against a second code called `Synrad+`. Later we simulated experimental conditions on a copper surface the way it was measured.

4.4.1 `Synrad+`

Synrad+, like Synrad3D, is a Monte Carlo simulator for synchrotron radiation, developed since the 1990s. With Synrad+ the user can define the beam properties and magnetic regions, typically representing dipoles or quadrupoles. The software then calculates the beam trajectory and generates virtual photons distributed evenly along the beam path inside the magnetic regions. These photons are then traced in a geometry described by polygons, that can be defined inside the code or imported from external CAD programs. Due to the 3D visualization and since geometries of arbitrary complexity can be treated, Synrad+ is suitable for detailed simulations of accelerator components. Since the number of polygons is limited to a few hundred thousands, however, Synrad+ cannot simulate large (e.g., several km long) machines without significant simplifications of the geometry.

4.4.1.1 Comparison

As in Sec. 5.1.1, we consider the optical lattice of an LHC arc cell at top energy, i.e. 7 TeV. One optical arc cell consists of two halves with three bending magnets each. We limited our simulations to synchrotron radiation emitted while passing through the fields of these dipoles. We started by comparing the emission mechanisms, and then moved into the tracking of photons through all reflections till final absorption; for each case 0.2 million photons were tracked using Synrad3D and 100 million with Synrad+.

For the first part we defined the wall as a perfect absorber, so that the absorption points would depend solely on the emission, and we used an ideal beam with zero emittance. Figure 4.10 shows the absorption of photons along the coordinate s as determined by both codes.

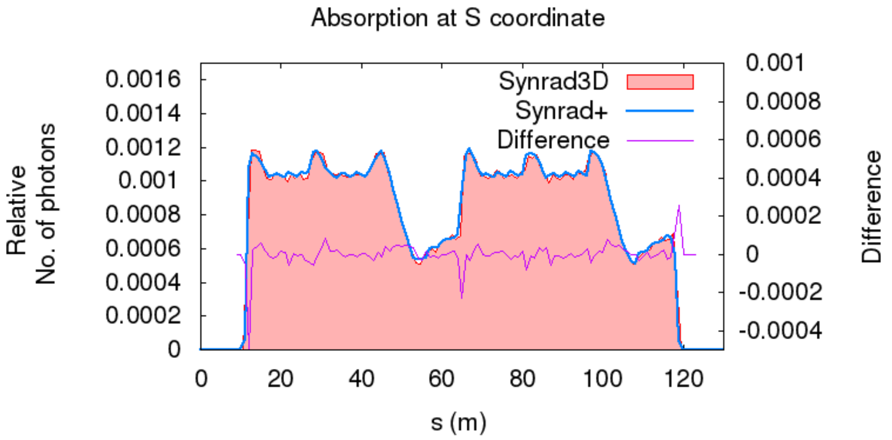

FIGURE 4.10: Simulated photon absorption as a function of longitudinal coordinate s for one LHC arc cell, treating the chamber wall as a perfect absorber; the blue line is the result using Synrad+, while the red area is the result from Synrad3D.

Next, we included the size of the beam and the material properties of the chamber wall in the simulation. We considered a copper wall, without any carbon coverage on the surface, with a surface roughness of 40 nm. In addition, the sawtooth pattern on the horizontally outward side of the vacuum chamber was included. For this simulation model, the absorption points along the coordinate s obtained from each code are compared in Fig. 4.11.

4.4.2 Measurements

The reflectivity measurements were performed at BESSY II. The general experimental setup is described in Refs. [61] and [62], as schematically shown in Fig. 4.12. Synchrotron radiation coming from BESSY II is made monochromatic through a plane grating monochromator (PM-1) with blazed gratings (1200 l/mm), before arriving to the end station. In this configuration, it is possible to vary the photon energy from 35 to 1800 eV, the incidence angle from 0° to 90° and the detectors position from 0° to 180° with respect to the optical axes, collecting the specular

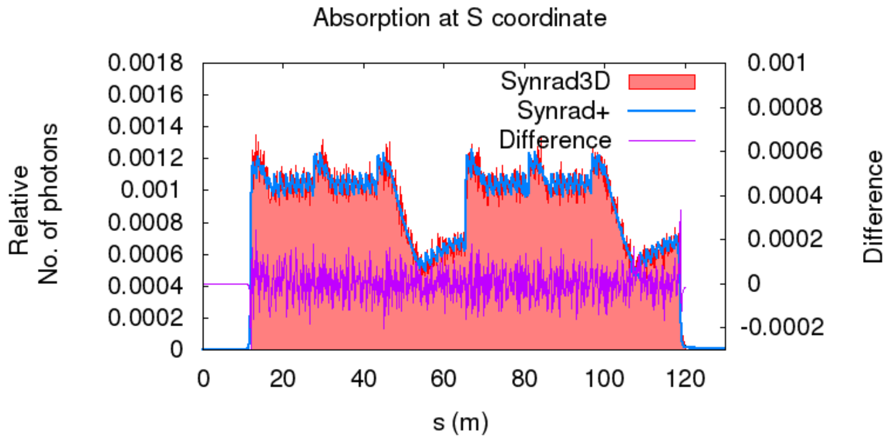

FIGURE 4.11: Comparison of photon absorption as a function of s simulated by Synrad+ and `Synrad3D`, for the realistic model of the beam pipe.

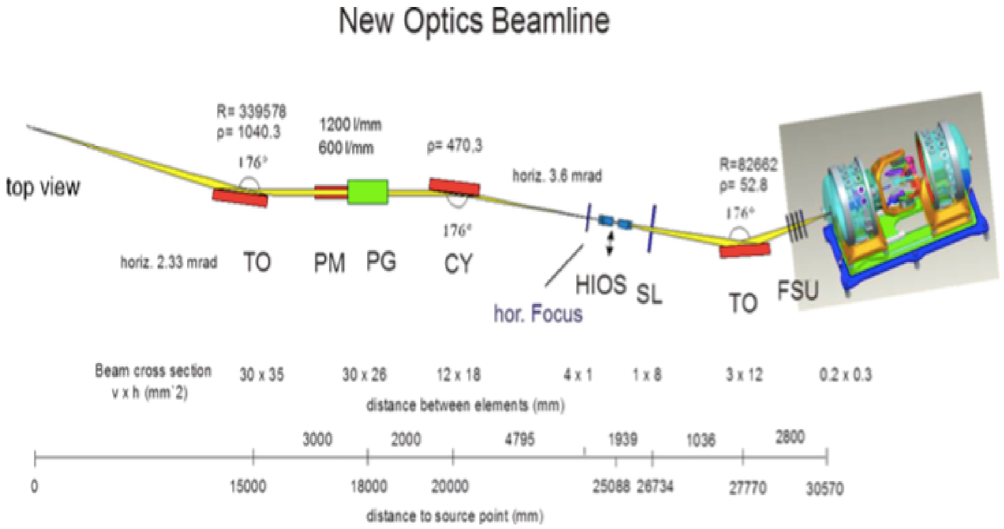

FIGURE 4.12: BESSY II optics beamline [61].

and non-specular reflections. The accuracy of the specular reflection measurement depends on the purity of the monochromatic light in the BESSY II beam line; a conservative error estimate is 10^{-5}. The error of total reflectivity measurements for a rough surface can be 100 times larger. Our measurements were performed on two different samples: a smooth copper surface, with a roughness of $R_a = 9.6$ nm, and a 10 cm piece of a chamber, shown in Fig. 4.13, with the actual sawtooth pattern used for the LHC beam screen.

The measured specular reflectivity for the smooth copper sample, with an incident

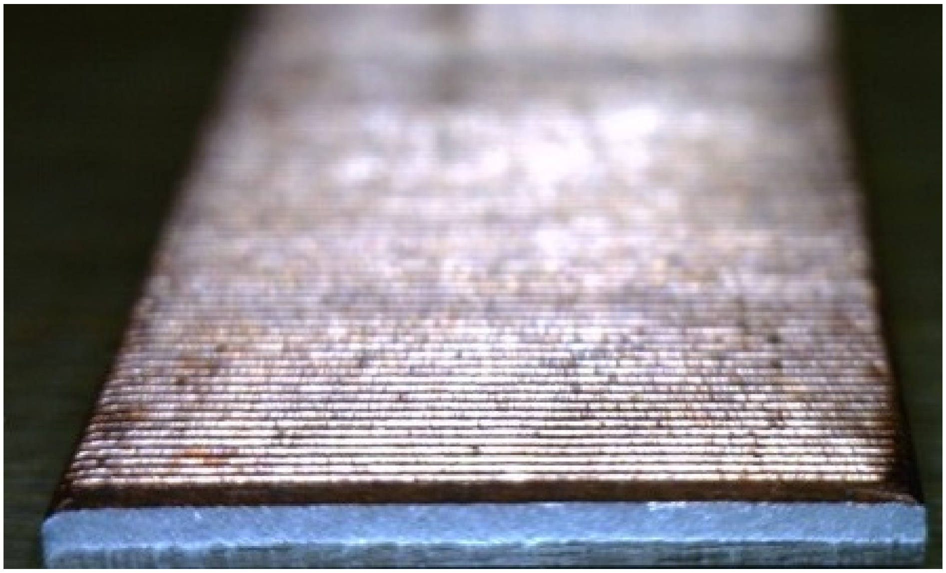

Figure 4.13: Cu sawtooth sample. Picture taken from [63],

angle spanning from 0.25° to 7°, is reported in Fig. 4.14 and the simulated total reflectivity (i.e. the sum of specular and diffuse reflection) in Fig. 4.15. These two results agree rather well. In fact, for close to ideal mirror-like surfaces the total reflectivity computed by Synrad3D is essentially all in the forward direction and, in this particular case, directly comparable with the experimental measurements of specular reflectivity as shown in Fig. 4.14. This would no longer be true for rough surfaces where the forward reflected component is only a fraction of the total reflectivity.

Certainly this correspondence is not fulfilled for the sawtooth structure, illustrated in Fig. 4.13. In Fig. 4.16 we present the measured forward reflectivity for two angles of incidence, 1° and 2°, for the sawtooth sample. The value of the measured forward reflectivity is much reduced compared with the specular reflectivity observed for a smooth surface; compare for example the curve for 50 eV in Fig. 4.14. The sawtooth structure was indeed introduced to reduce forward reflectivity to mitigate the electron-cloud build up due to photoelectrons [64–66].

The curves in Fig. 4.17 represent the simulated total reflectivity. The measured forward reflectivity of Fig. 4.16 is significantly lower than the total simulated reflectivity as would be expected for an artificially rough surface.

At three photon energies (36, 45 and 100 eV), and two different angles of incidence (1° and 2°), we measured the entire photon distribution over a significant solid angle. An experimental estimate of the total reflectivity was obtained by numerical integration of all forward, diffused and back reflected photons over the available solid angle. Figure 4.17 includes these six measurement points of total reflectivity for the sawtooth chamber (the dots), revealing a higher total reflectivity than expected from the simulation model. In particular, the simulated reflectivity decreases by more than a factor of 10 as the photon energy increases from 35 to 100 eV, while the measured reflectivity at 35 eV is about 2 times larger than the simulated value, and remains almost constant for higher photon energies. Both simulated and measured reflectivities weakly depend on the (small) angle of incidence.

The measured data demonstrate the ability of the BESSY II system to distinguish between forward, diffused and back reflected photons, representing an ideal test bench to verify simulation codes.

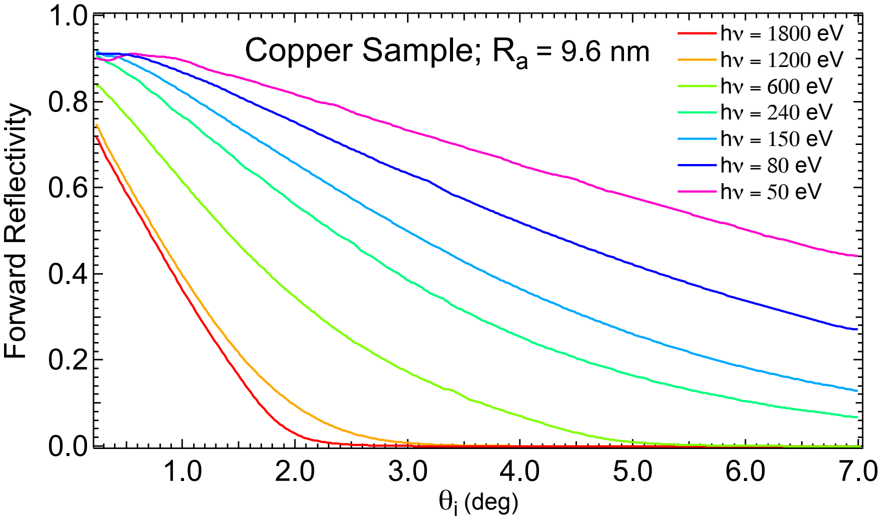

FIGURE 4.14: Measured normalized reflectivity vs. incidence angle for different energies for a copper surface, for different photon energies. Picture taken from [63],

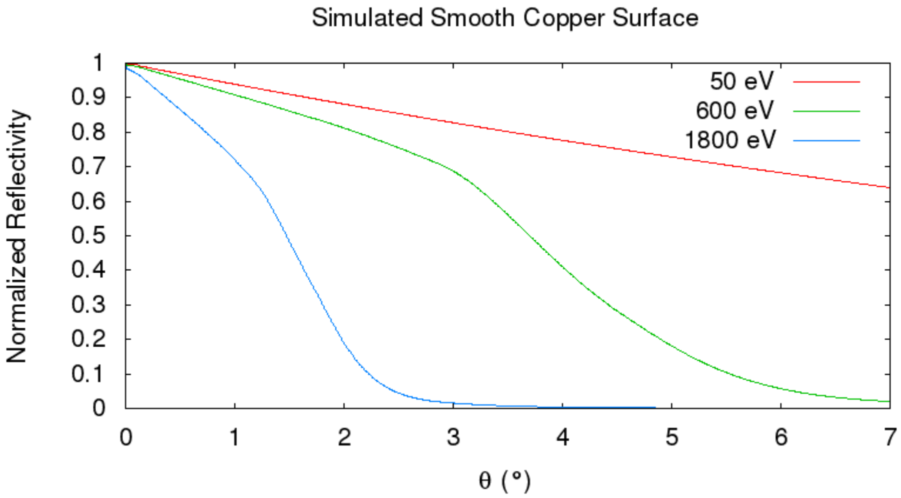

FIGURE 4.15: Simulated normalized total reflectivity vs. incidence angle for different energies for a copper surface, for different photon energies.

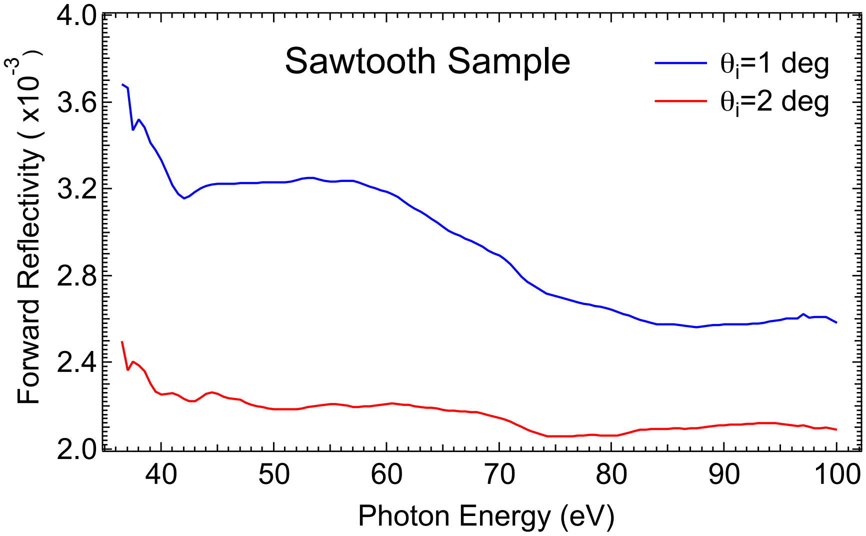

FIGURE 4.16: Measured normalized forward reflectivity as a function of the energy of impinging photons (36 eV - 100 eV), for two different incidence angles on a sawtooth chamber. Picture taken from [63],

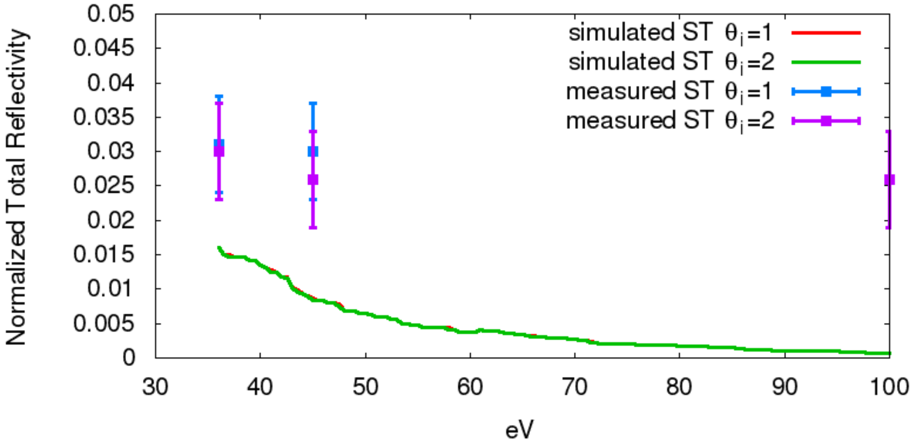

FIGURE 4.17: Simulated normalized total reflectivity as a function of the energy of impinging photons (36 eV - 100 eV), for two different incidence angles on a sawtooth chamber. Picture taken from [63],

Chapter 5

Results

We ran `Synrad3D` which was described in Ch. 4. Our goal was to produce a map of absorbed photons on the surface of the beam screen for the accelerators described in Ch. 3. In the following I first present the simulation results for each accelerator, and then a discussion of the results. The main results presented in this chapter, were published in [67].

5.1 LHC

In order to fully appreciate the effect of the sawtooth pattern imprinted on the beam screen of the LHC, we first ran the simulations for the model described in Sec, 5.1.1. We then simulated the effect for two other cases: a) the absence of the sawtooth. And b) and inverted sawtooth in the longitudinal coordinate as shown in Fig. 5.1 bottom left. A motivation for this second comparison is that since 2008, a number of LHC arc beam screens are installed with the wrong orientation (“inverted sawtooth") [68]. This could be causing certain sectors to overheat or to be susceptible to enhanced electron clouds.

5.1.1 SMIF

The SMIF used to run these simulations assumed the following parameters:

- The wall file describing the vacuum chamber with a sawtooth pattern, consisting of a series of 30 μm high steps at a distance of 500 μm in the longitudinal direction, on the horizontally outward side of the chamber. Figure 5.1 shows the model of the LHC sawtooth beam screen implemented in `Synrad3D` for the case of an inverted sawtooth.

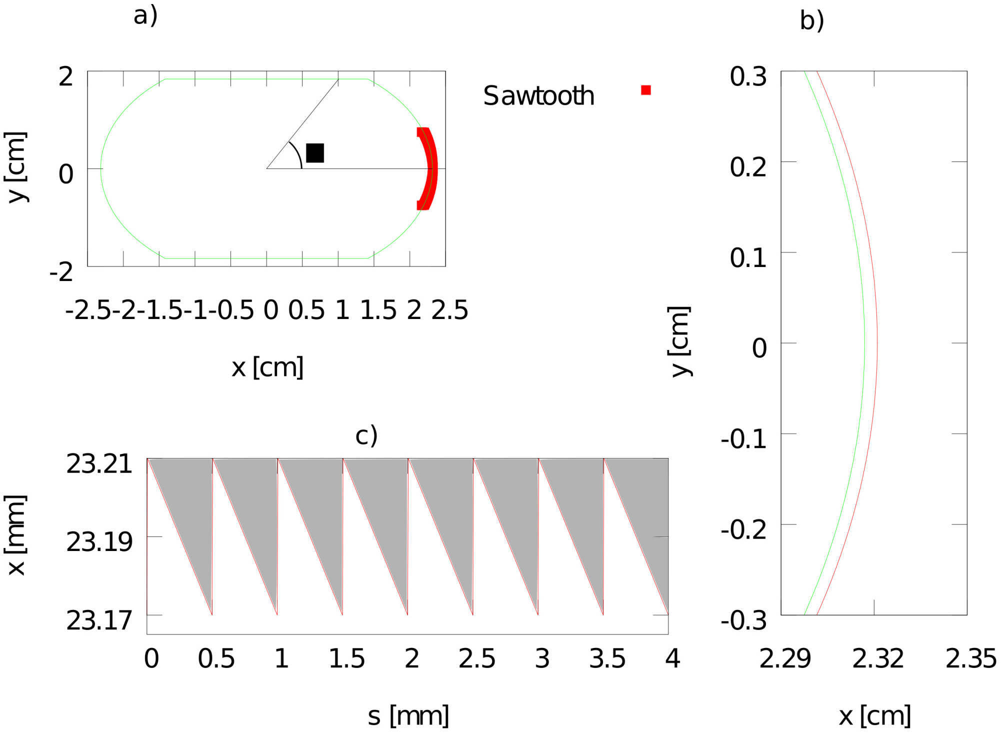

FIGURE 5.1: `Synrad3D` model of LHC beam screen design with an inverted sawtooth chamber, and definition of the angle ϕ.

- The lattice file which contains the version 6.5 of the LHC was employed.
- The simulated section were two half cells, which are then periodically repeated at the arcs.
- The photon direction was set to be positive which means a forward generation.

- The total number of photons generated varied between half a million and two millions per run.
- The seed for the random number generator was set to be the system clock.
- A custom reflectivity table was used. This table assumes a carbon layer of 10 nm on a copper substrate. For this table the probability of reflection (P_{reflect}) was taken from the LBNL X-ray database [69]. Some example reflection probabilities for an LHC-like chamber surface with a 10 nm thick carbon layer on top of the copper are presented in Fig. 5.2. The carbon layer models the effect of surface conditioning due to electron bombardment ("electron-cloud scrubbing") [39]. For protons of 7 TeV energy passing through an arc bending magnet, the critical photon energy for LHC proton synchrotron radiation is about 44 eV.

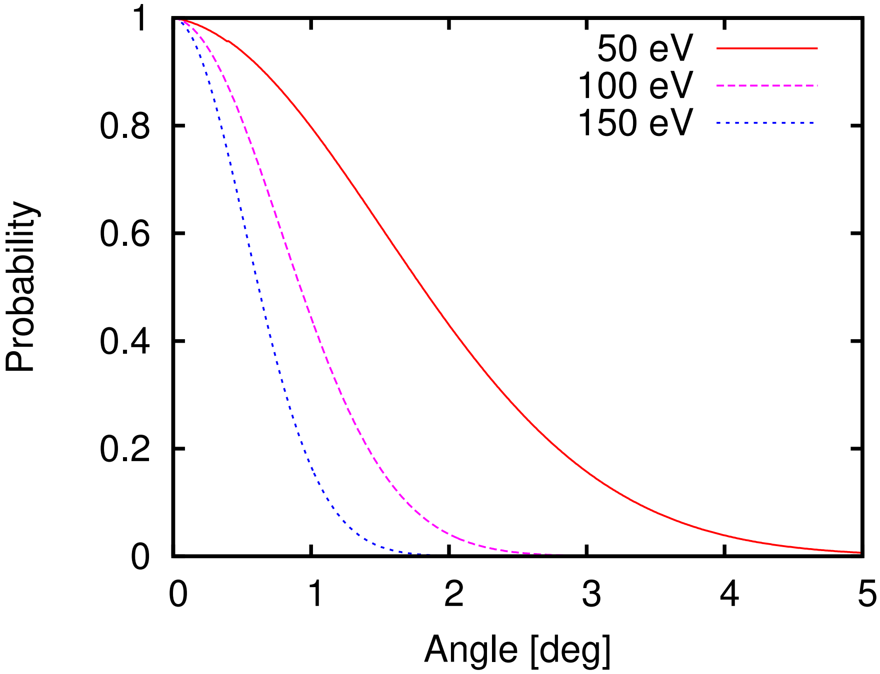

Figure 5.2: Specular photon reflectivity as a function of angle of incidence for several different photon energies, considering a 10 nm carbon layer on top of a copper surface and 50 nm rms surface roughness.

5.1.2 Analysis

The simulated distributions of absorbed photons in Fig. 5.3 and the corresponding reflection distributions in Fig. 5.4 illustrate the effect of the sawtooth surface as well as the effect of an inverted sawtooth. The number of passages is defined as the number of reflections plus one.

For the case of the sawtooth most photons are absorbed at the moment and location of primary impact ($\phi \approx 0$), as the mean number of passages is about 1, or the mean number of reflections close to 0, in Fig. 5.4. This explains the peak of the absorbed photon distribution at $\phi \approx 0$, in Fig. 5.3.

In case of the smooth chamber the average number of reflections is higher than 80, in Fig. 5.4, and, as a result, the location of absorbed photons is almost uniform around the azimuth, in Fig. 5.3, with only a slight bias towards the primary impact area, and tiny local maxima corresponding to the transitions between circular and flat portions of the beam screen in Fig. 5.1 (top left).

Finally, for the inverted sawtooth the average number of photon reflections is about two (Fig. 5.3), which gives rise to almost equally high absorption maxima on the horizontally outward and inward sides of the chamber in the horizontal plane, as can be seen in Fig. 5.3 . With this rather low number of reflections, photons are not yet spread towards the top and bottom of the vacuum chamber.

With the sawtooth only 0.2% each, of the photons, are absorbed on the top and bottom surfaces, whereas 99.6% are absorbed on the sides as is shown in Fig. 5.5. The Confidence Interval (CI) was calculated using the formula: $\hat{p} \pm 1.96\sqrt{\frac{\hat{p}(1-\hat{p})}{n}}$, where $\hat{p}$ is the relative amount of absorbed photons per side and n is the amount of generated photons.

By contrast, with no sawtooth 41% of the photons are absorbed on the primary impact side, 23% on the opposite side, and 18% each on the top and bottom of the chamber. These results can be compared with experimental measurements at VEPP-2M [70, 71] and ELETTRA [65].

For a quantitative comparison, the VEPP-2M measurement for a smooth copper coated surface without sawtooth at 20 mrad grazing incidence revealed a photon forward reflectivity R of up to 95% [71]. This would correspond to an average number of $\langle n \rangle = (1-R)\sum_n R^{n-1} = 1/(1-R) \approx 20$ photon passages through the chamber until absorption. Adding another 2–4% diffusely reflected photons [71], the average number of photon passages in the measurements would be between 33 and 100, which is consistent with the value of about 80 found by the Synrad3D simulations, in the top picture of Fig. 5.4. For the sawtooth surface a much lower total reflectivity of about 10% was measured [65]. This translates into an average number of passages not much above 1, and the Synrad3D simulations also predict a value barely above 1 (see the bottom picture of Fig. 5.4).

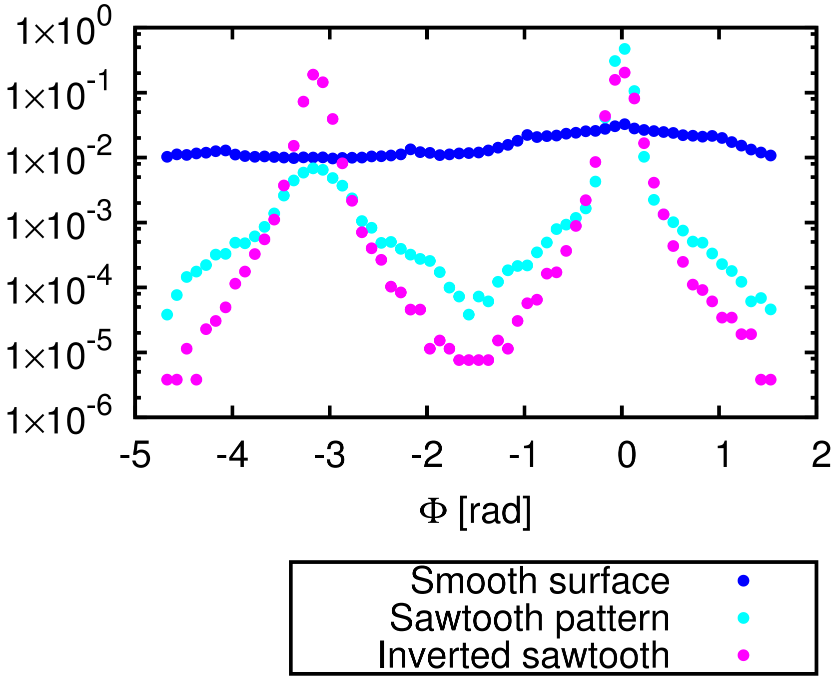

Figure 5.3: Simulated azimuthal distribution normalized to one of absorbed photons without (blue), with sawtooth (teal) and with an inverted sawtooth (purple) chamber.

The almost 10-fold reduction of photons hitting the top and bottom of the chamber confirms the intended effect of the sawtooth structure, namely to greatly reduce the number of photoelectrons generated at the top and bottom of the vacuum chamber in the arc dipole magnets (from where they could approach the beam, following the vertical field lines, and contribute to further electron-cloud build up).

While for the inverted sawtooth the average number of reflections is higher than for correct sawtooth (Fig. 5.4), to our surprise the inverted sawtooth proves even more efficient than the sawtooth in reducing the number of photons absorbed at the top or bottom of the chamber (Fig. 5.3). This strongly suggests that the assumptions for an inverted sawtooth made in [72] were very pessimistic.

5.2 HL-LHC

As mentioned in Sec. 3.2.2, the ATS optics may change the photon absorption distribution in the arcs because of the changes in β_{max}. Figures 5.6, 5.7, 5.8 show the β functions for the different optics: pre-squeezed, round and flat; in that order. Since the only relevant change toward photon absorption distribution is the lattice, this was the only modification to the SMIF described in Sec. 5.1.1.

Nevertheless, with a geometric rms emittance, ε_y, of about 0.3 nm, the corresponding maximum rms divergence of $\sigma_{y',\mathrm{max}} \approx (\varepsilon_x/\beta_{y,\mathrm{min}})^{1/2} \approx 5 \times 10^{-4}$ is still small compared with the rms angle of the photons emitted, $\sim \gamma^{-1} \approx 1.3 \times 10^{-6}$. Therefore no large effect of the ATS optics on the photon distribution is expected. Given that $\beta_{y,max}$ is a factor of 8 times larger for the flat ATS optics compared to the presqueezed, we expected that if there were any variation it would be more visible than that of the round ATS optics whose $\beta_{y,max}$ is only a factor of 4 times larger. Figure 5.9 shows the azimuthal distribution of photon absorption for both presqueezed and flat ATS optics. This expectation was confirmed in Synrad3D simulations by comparing photon distributions for a squeezed flat optics with those for the “pre-sequeeze” (equal to the standard LHC arc optics) [73].

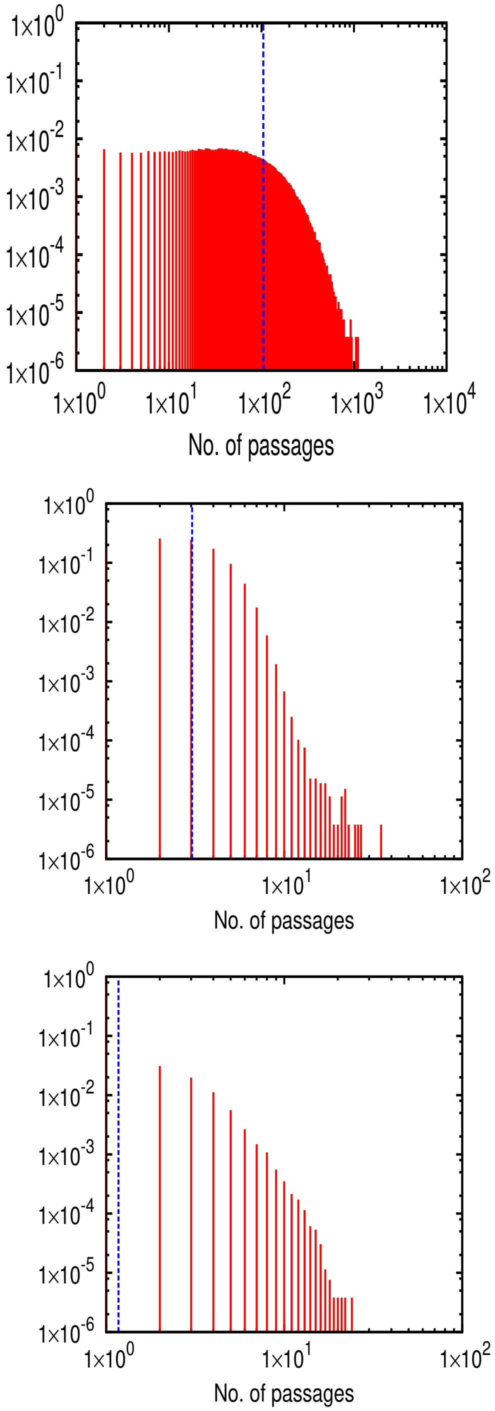

FIGURE 5.4: Distribution of number of photon passages till absorption without (top), with sawtooth chamber (bottom) and inverted sawtooth (center). The blue line represents the mean number of passages.

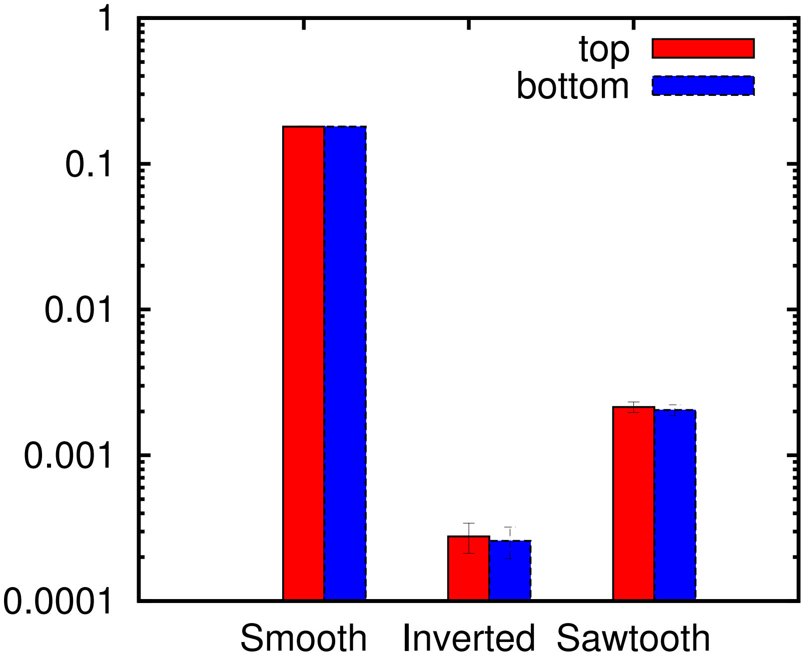

FIGURE 5.5: Fraction of photons absorbed at the top and bottom of the vacuum chamber of the LHC, with a 95% confidence interval.

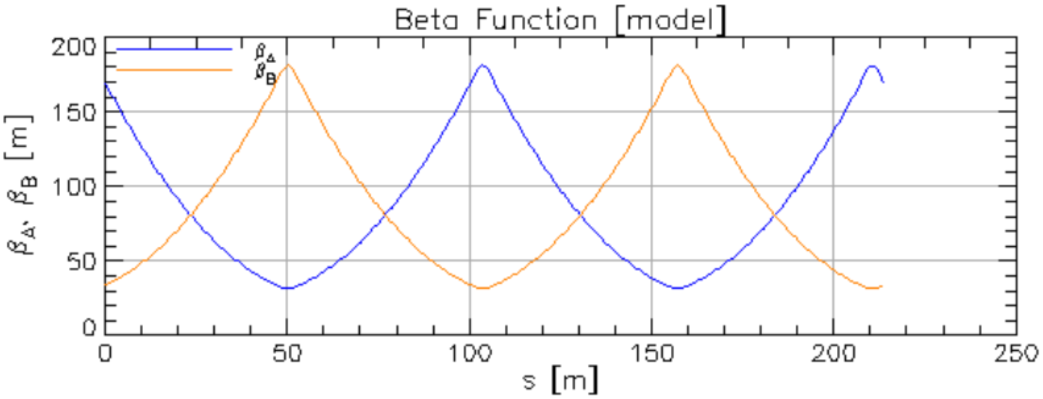

FIGURE 5.6: β functions in half a cell for the pre-squeezed optics.

5.3 HE-LHC

The main objective of this section was to compare the efficiency of the FCC-hh vacuum chamber and a scaled version of the LHC beam screen as they were competing proposals to be used for HE-LHC.

A secondary objective was to simulate the efficiency of the slots of the FCC-hh vacuum chamber as a function of energy.

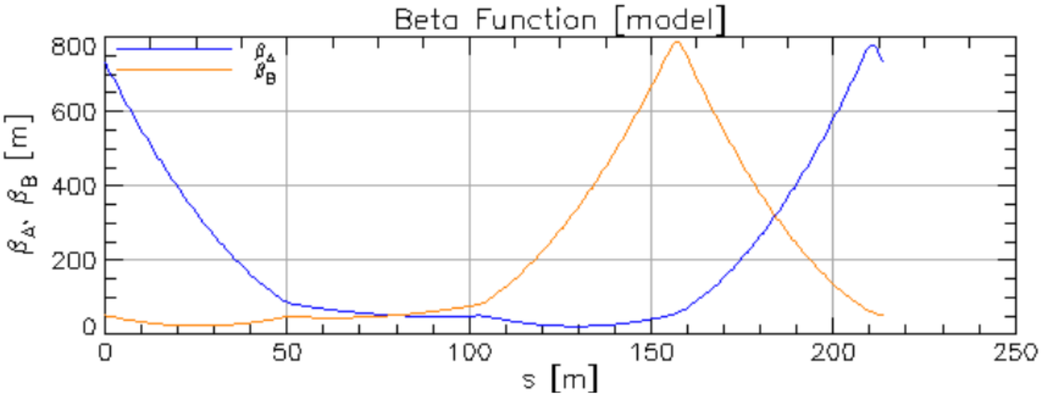

FIGURE 5.7: β functions in half a cell for the round ATS optics.

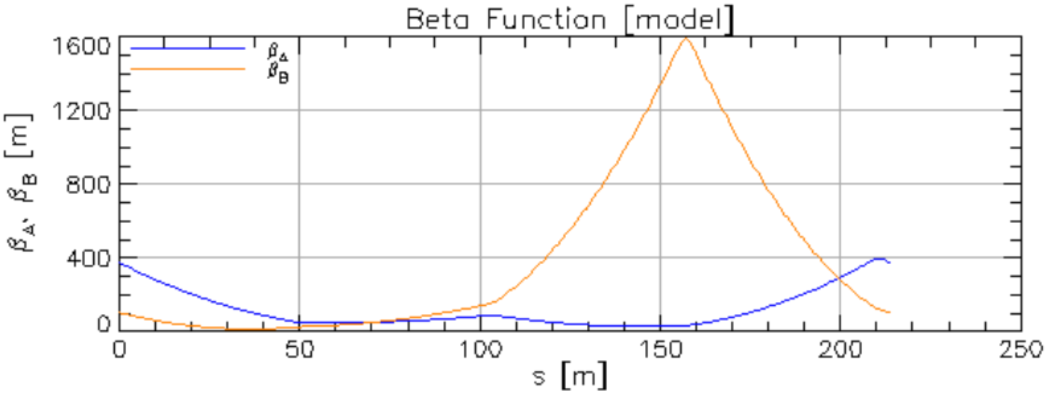

FIGURE 5.8: β functions in half a cell for the flat ATS optics.

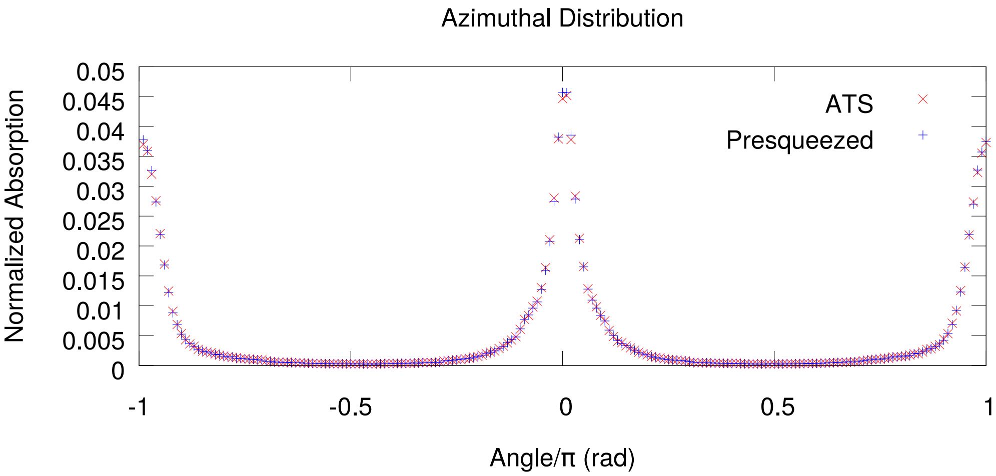

FIGURE 5.9: Photon absorption distribution for the presqueezed optics and the flat ATS optics.

5.3.1 SMIF

The SMIF used to run this simulations used the following parameters:

- The options to be analysed are shown in Fig. 5.10 along with the LHC beam screen. This first FCC-hh vacuum chamber approach (in red in Fig. 5.10) considers a slot 5 mm in height along the longitudinal axis. All photons going into this slot are considered to be lost. The scaled version of LHC beam screen is shown in pink in Fig. 5.10, it considers a 7.5 mm height sawtooth pattern just as LHC.
- Since the HE-LHC has no definitive optics yet, our preliminary studies used the pre-squeezed lattice for HL-LHC scaled in energy to 13.5 TeV per beam.
- The simulated section were two half cells, which are then periodically repeated in the arcs.
- The photon direction was set to be positive which means a forward generation.
- The total number of photons generated were over two millions per run.
- The seed for the random number generator was set to be the system clock.
- The material was considered to be the same as for the LHC simulations.

5.3.2 Analysis

Figure 5.11 illustrates that the FCC-hh chamber is four or five times more efficient than the scaled LHC chamber, in reducing photon absorption at the top and the bottom of the chamber.

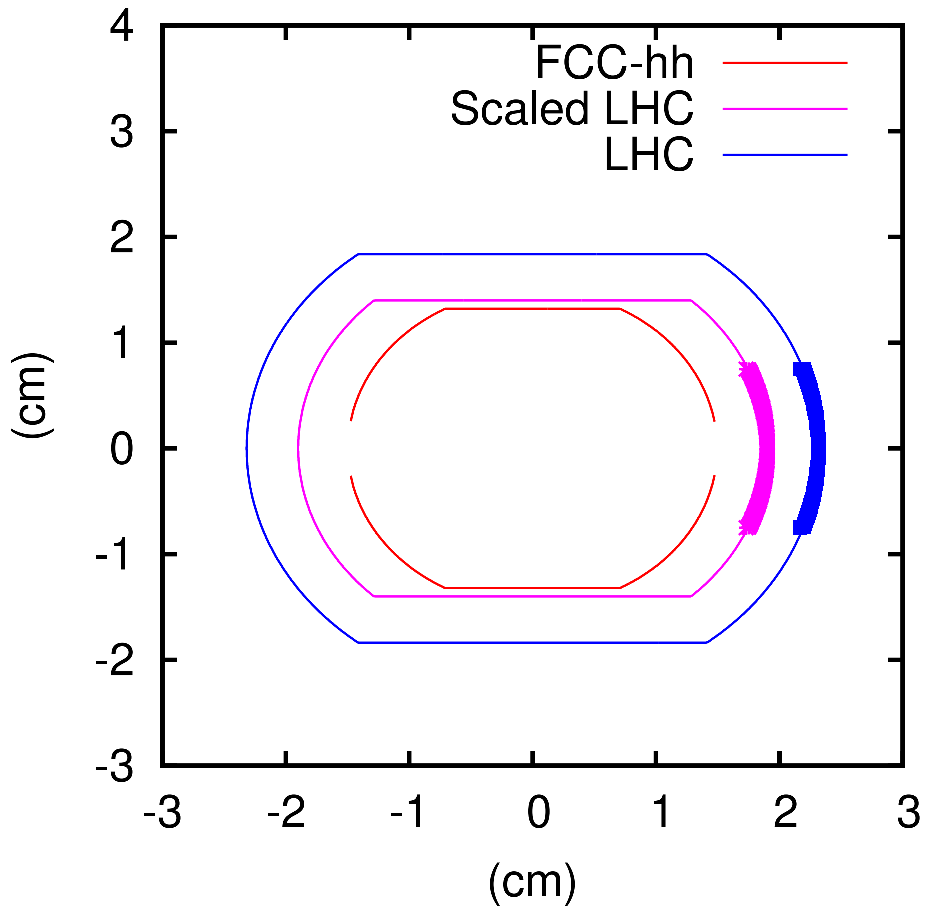

Figure 5.10: `Synrad3D` model of the FCC-hh vacuum chamber as well as the LHC beam screen and its scaled version.

5.3.3 Energy dependence

Since the angular distribution of the emitted synchrotron-radiation photons depends on the beam energy and emittance, we simulate, for different beam energies, the fraction of photons escaping from the slots of the FCC-hh-type beam screen

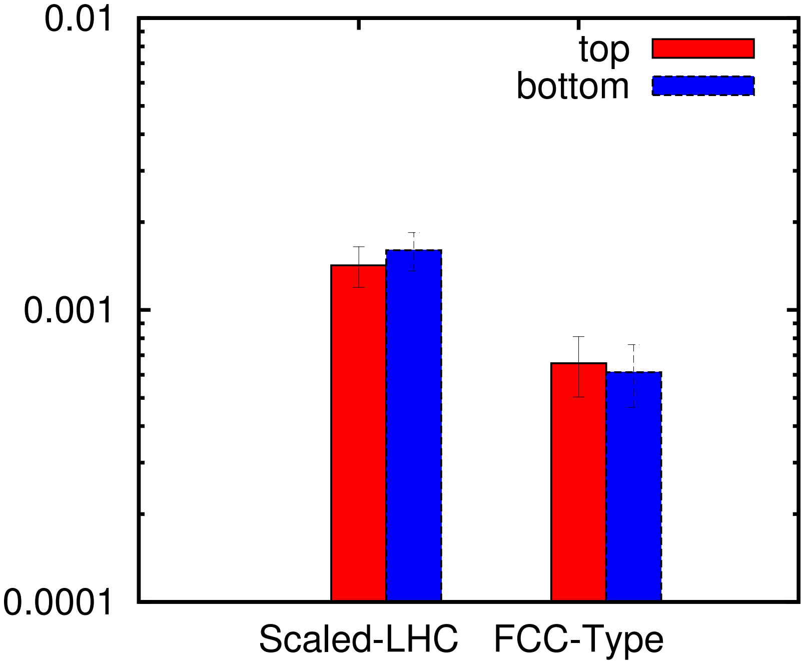

Figure 5.11: Fraction of photons absorbed at the top and bottom of two proposed vacuum chambers for the HE-LHC, with a 95% confidence interval.

and being absorbed on the surface of the beam chamber proper. Considering the LHC (HE-LHC) optics as an example, the result of such an energy scan is displayed in Fig. 5.12. The FCC-hh beamscreen is extremely effective at 50 TeV, but a factor 10 less at 7 TeV. As indicated in the figure, the fraction of photons not entering the slots decreases roughly inversely with the beam energy, as the vertical opening angle of the synchrotron radiation.

5.4 FCC-hh

Keeping a map of photon absorption in the FCC-hh vacuum chamber up to date, proved to be a difficult task, given the fast changes in the design, as mentioned in Sec. 3.3.4. In this section we are interested firstly in the azimuthal distribution of SR photon absorption. Then we introduced orbit displacements in the vertical axis to the optics in order to determine the sensibility of the efficiency of the slots

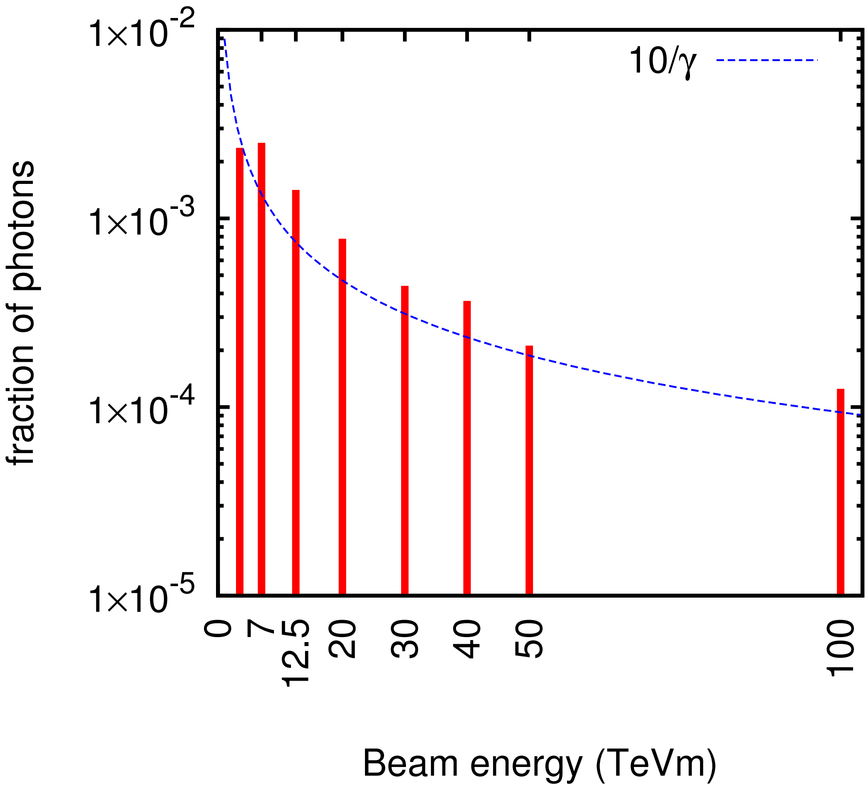

Figure 5.12: Fraction of photons absorbed by an FCC-hh type chamber as a function of beam energy for a normalized emittance of ε=2.5 μm and the LHC optics.

to this type of effects. Finally we show the angular distribution for an updated vacuum-chamber model.

5.4.1 SMIF

The SMIF used to run these simulations used the following parameters:

- The first approximation model for FCC-hh vacuum chamber is shown in Fig. 5.10 and described in Sec. 5.3.1. The schematic is shown in the third image in Fig. 3.7 from left to right. An updated version of this model is shown in 5.13. It considers a 7.5 mm aperture instead of 5 mm as before. It represents the chamber shown in Fig. 3.8a. The latest version is shown in Fig. 3.8b. This model also considers a 7.5 mm aperture, the deflector was substituted for a sawtooth pattern on both sides. The copper layer only covers the sections visible to the beam. We consider photons going into the antechamber to be lost. The schematic is shown in Fig. 5.14.

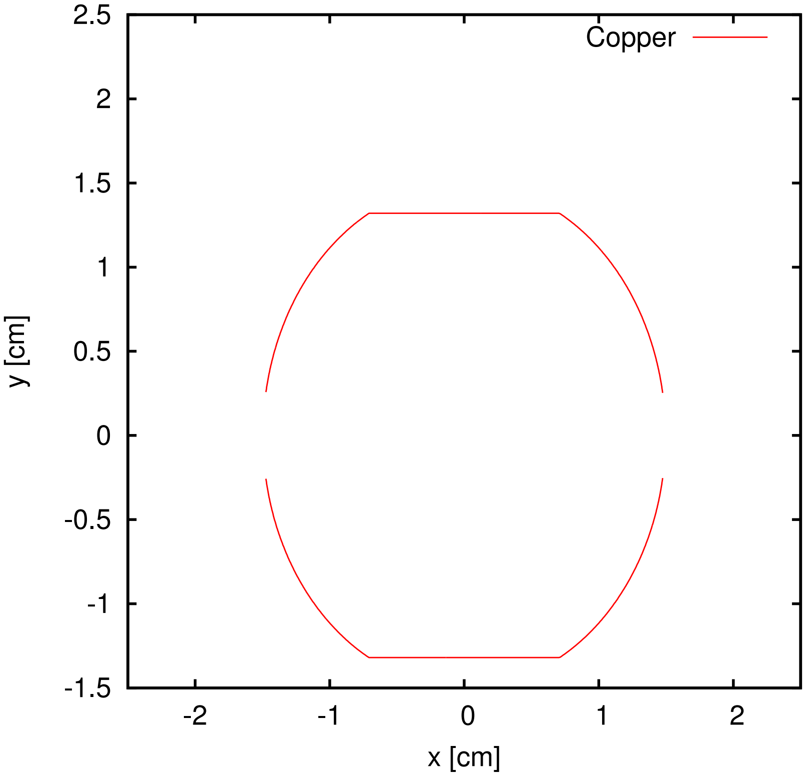

Figure 5.13: First approximation `Synrad3D` model of the FCC-hh vacuum chamber proposed in 2017.

- The simulation considered two half cells of the FCC-hh arcs with a length of 213.89 m. In a half cell, the main synchrotron radiation source is six dipole magnets, each 14.3 m long, with a dipole field of 16 T [74, 75]. A value of the normalized emittance of ε=2.2 μm is considered [76] and the energy equal to the collision beam energy (50 TeV).

- The photon direction was set to be positive which means a forward generation.

- The total number of photons generated were over two millions per run.

- The seed for the random number generator was set to be the system clock.

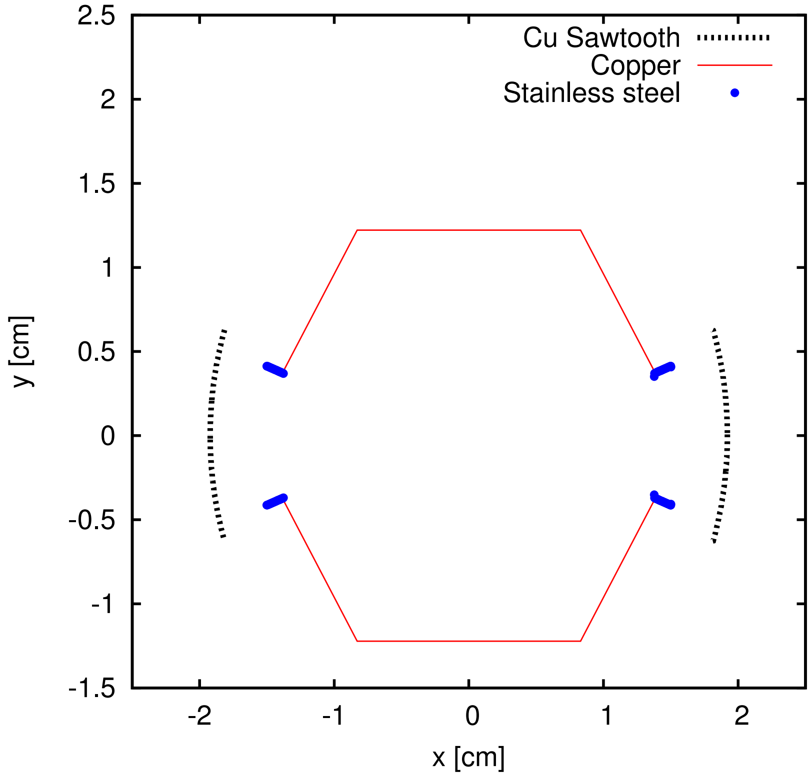

FIGURE 5.14: Updated `Synrad3D` model of the FCC-hh vacuum chamber proposed in 2018.

- The material was considered to be the same as for the LHC simulations, and stainless steel for the last model.

5.4.2 First azimuthal distribution

In our first model we assumed the slits were perfect absorbers, so in our first simulations, the large majority of photons escaped through them. This model is too ideal and not very reliable, since the photons are not actually absorbed, but leaving the environment, there would always be a chance, however small, that they would return.

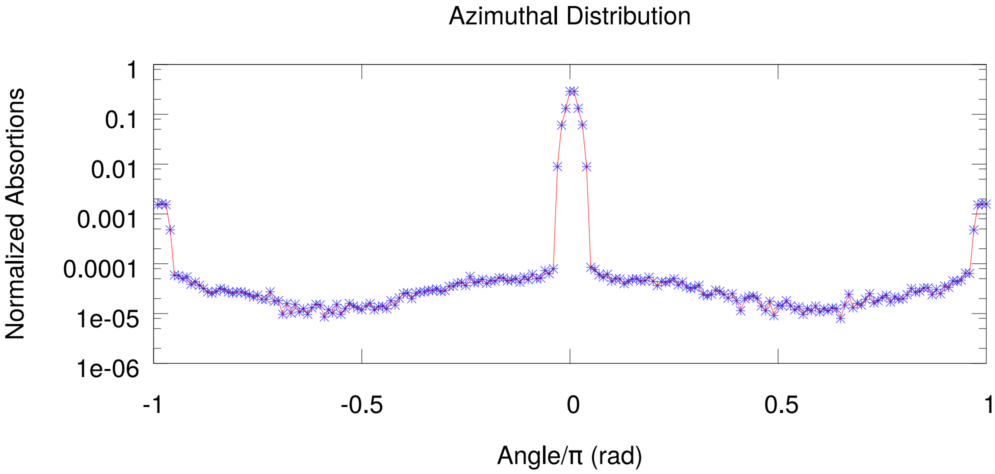

Figure 5.15: Photon absorption distribution in the FCC-hh vacuum chamber for an ideal orbit.

5.4.2.1 Orbit displacement

For a centered orbit, a fraction of 0.05% of the emitted photons are hitting the beam screen outside of the absorber slots. Figure 5.16 shows the dependence of this fraction on a vertical orbit offset, setting a tolerance on the acceptable closed-orbit distortions in the FCC-hh of about 1 mm (peak offset from the horizontal plane).

5.4.3 Distribution per sides for the updated models

Preliminary results for the updated models were obtained and analyzed per side. Figures 5.17 and 5.18 show the normalized photoabsorption per side for the 2017 (see Fig. 5.13) and 2018 models (see Fig. 5.14). This second approximation, includes the edge of the chamber, which could be of a different metal, namely stainless steel. Although this last model still has some ideal absorbers, it is much more reliable than the previous one, because the large majority of photons are actually absorbed within the environment, and just an insignificant fraction (<0.5%) of them escape through the absorbers. as we can see in the absorption histogram in Fig. 5.19.

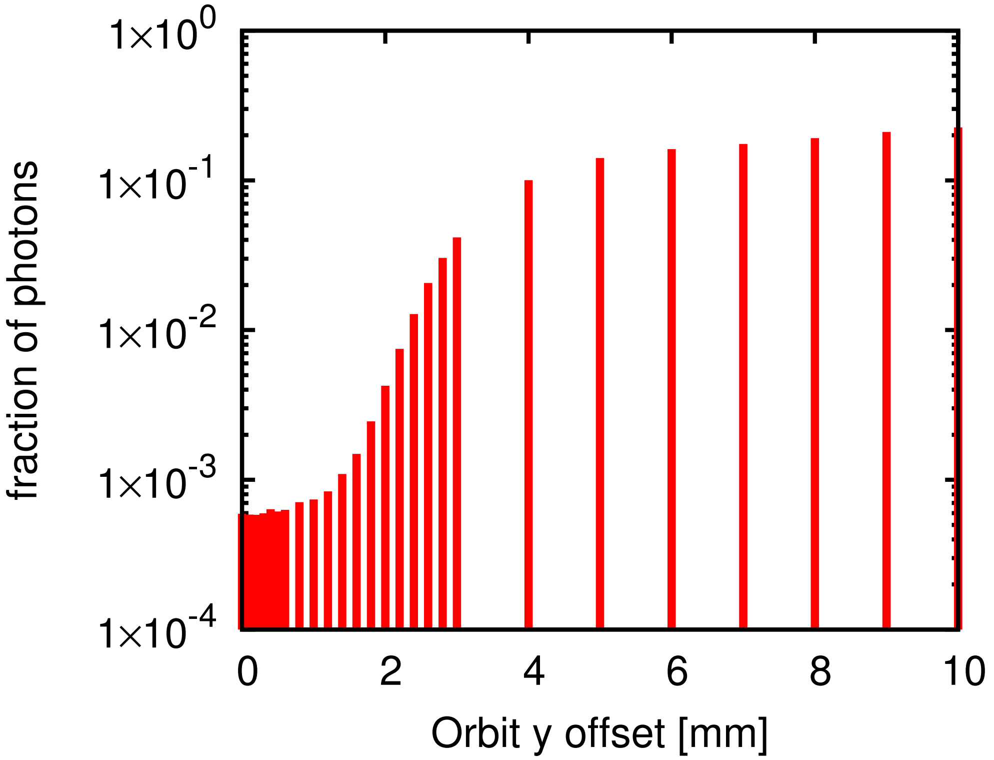

FIGURE 5.16: Simulated fraction of photons absorbed on the inner FCC-hh beam screen as function of peak vertical orbit error.

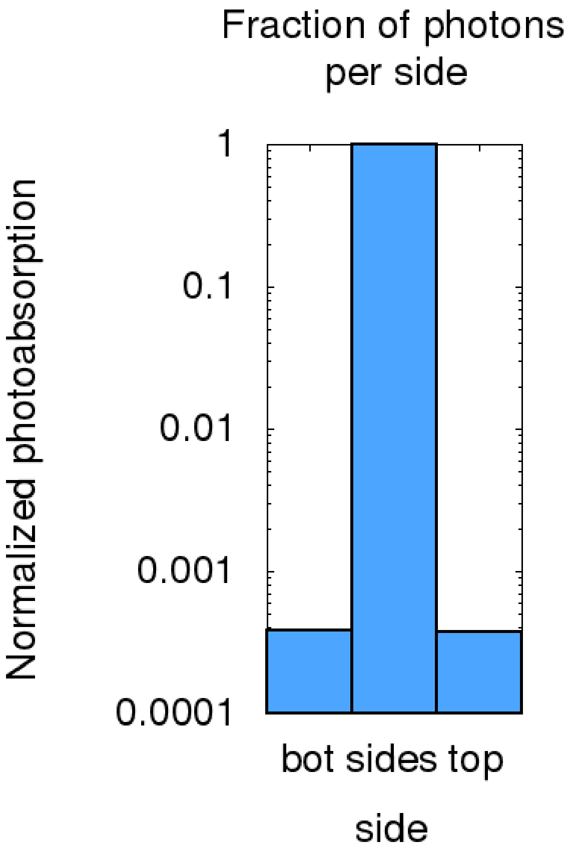

FIGURE 5.17: Fraction of photons absorbed at the bottom, sides and top of the 2017 version of the FCC-hh vacuum chamber.

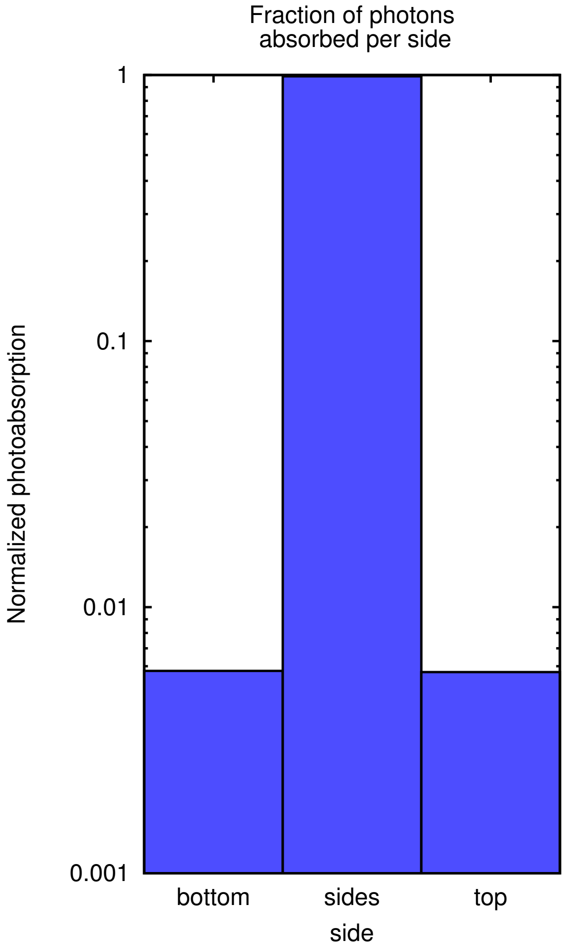

Figure 5.18: Fraction of photons absorbed at the bottom, sides and top of the 2018 version of the FCC-hh vacuum chamber.

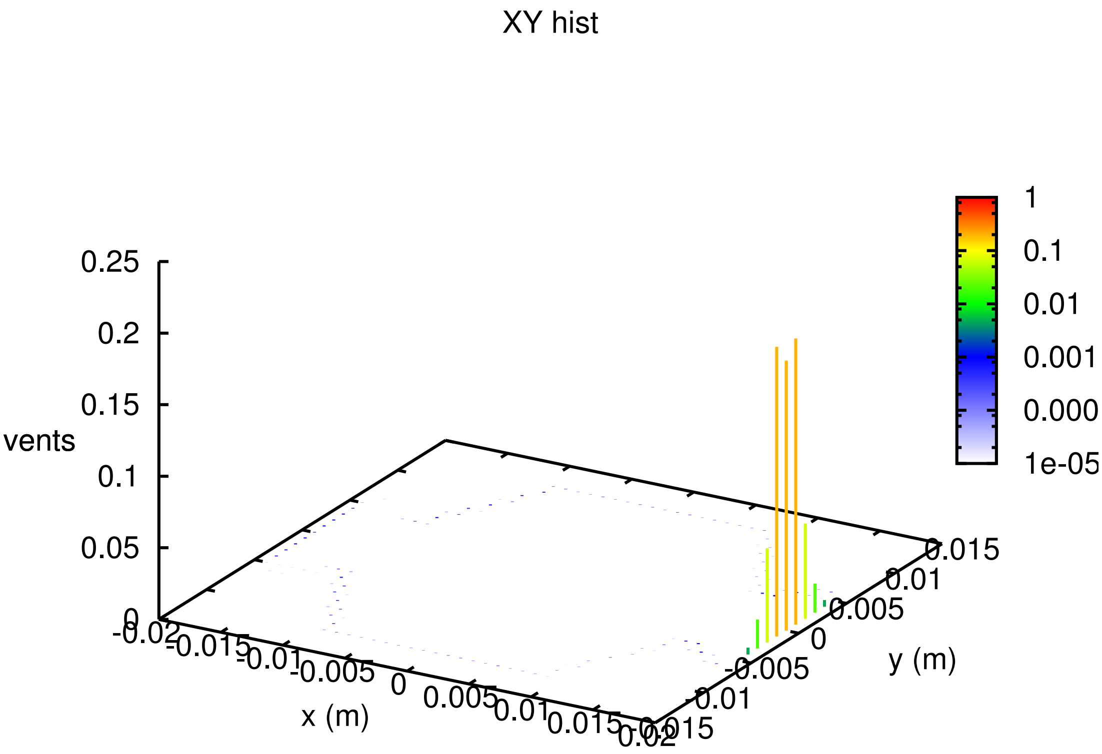

Figure 5.19: Normalised photoabsorption histogram of the 2018 version of the FCC-hh vacuum chamber.

Conclusions

In this thesis, using an extended version of the simulation code `Synrad3D`, developed at Cornell, I studied the flux of synchrotron radiation emitted inside the cold superconducting arc magnets of the present LHC collider, its upgrade HL-LHC, and the proposed future highest-energy hadron accelerators HE-LHC and FCC-hh. The efficiency of various applied or planned mitigation measures, like a sawtooth structure on the LHC beam screen or opening slots for FCC-hh, were investigated and have already helped in the design of future-accelerators vacuum chambers. The effect of electron-cloud surface conditioning ("scrubbing") was modelled by considering a thin 10 nm carbon layer on top of the beam screen's copper coating.

A validation of the `Synrad3D` code and of its applicaton to the LHC was performed by benchmarking the results both with another code, Synrad+, and against laboratory measurements on prototype LHC vacuum chambers.

Although in principle one should be able to use either code for any synchrotron radiation analysis, we find that `Synrad3D` is more practical for complex or long lattices, while Synrad+ is better suited at treating difficult and irregular chambers, such as places where BPMs are installed. Synrad+ and `Synrad3D` produced nearly identical simulation results for the photon flux in an LHC arc cell. This was almost expected since the surface model used in the two codes is rather similar, and they considered the same reflectivity tables. The primary differences between the two codes are the modeling of the beam-pipe boundaries and the approximation used for the sawtooth pattern.

Comparing `Synrad3D` simulations with photon reflectivity measurements at BESSY II, we found a fairly good agreement in the specular photon reflectivity, even in absolute value, between the predictions from `Synrad3D` and the experimental results for flat samples. According to both simulations and measurements, for the sawtooth pattern, the specular (forward) reflectivity is much reduced, at the expense of increased diffuse scattering and backscattering. However, the simulated total reflectivity is significantly lower than the measured total reflectivity and decreases much more strongly with photon energy. This qualitative difference might be due to differences between the manufactured sawtooth and the idealized model used in the simulation.

For the present LHC, the simulations demonstrate the efficiency of the sawtooth surface in reducing the average number of reflections almost to zero. Thereby, as intended, the sawtooth greatly decreases the number of photons absorbed at the top and bottom of the chamber, from where, in a dipole magnetic field, photoelectrons could approach the beam. Remarkably, our simulations also suggest that an inverted sawtooth, yielding an average number of reflections of about 2, might be even more efficient in this regard. This result could be attributed to a predominance of specular over diffuse reflection for the inverted sawtooth with extremely low surface roughness.

For the High-Luminosity upgrade, other than having twice the photon flux it was confirmed that the ATS optics, with significant beta beating across the arcs, does not noticeably change the azimuthal photon distributions.

For the FCC-hh a new type of beam screen is proposed. The `Synrad3D` simulations confirm that this beam screen significantly reduces the number of photons absorbed inside the beam chamber proper, by more than two orders of magnitude. For a centered orbit, a fraction of 0.6 % of the emitted photons is being absorbed at the beam screen outside of the absorber slots. The dependence of this fraction on a vertical orbit offset, sets a tolerance on the acceptable closed-orbit distortions in the FCC-hh of about 1 mm to loose 99 % of emitted photons.

A more realistic model of the latest version of the FCC-hh vacuum chamber that includes sawteeth on both sides was implemented. This model proved to be more realistic than the prior one. For an ideal orbit, only close to 1 % of the emitted photons would be absorbed on either the top or bottom of the chamber.

For the HE-LHC, the FCC-hh vacuum chamber is about five times more efficient than the scaled LHC chamber, in reducing the number of photons absorbed at the top and bottom of the chamber, and, therefore, in suppressing possible electron-cloud build up due to photoemission. The scaled version of the LHC has been discarded as option now. It was shown that the efficiency of the slots in the FCC-hh vacuum chamber, increase as the energy increases. The amount of photons absorbed in the beam screen decreases roughly as $1/\gamma_r$.

In the frame of accelerator-science development in Mexico, I have helped in the preliminary design of the optics of the FODO cells. We proposed to use three 3 m-long FODO cells, with the following quadrupolar gradients: 0.09 T/m, 0.5 T/m, 0.9 T/m. The increase of strength is to compensante the gain in energy in the RF cavities between the cells while keeping the betatron functions constant [5].

Ongoing and future work

The design of future accelerators is a work in progress, As such, the benchamarks and techniques developed here, will be needed, and used, in the search of the optimal design parameters for future facilities. In the future we plan to refine the sawtooth model used in the simulation, to take and analyse more experimental data, including at larger angles of incidence and higher photon energies, and to proceed with the benchmarking of measurements and simulations.

Direct measurements of the sawtooth profile and the surface roughness are being performed at Cinvestav Merida. These measurements will help to improve the model of the sawtooth. Also, to further validate or improve the model, new experiments on SR reflection are being carried out at BESSY II, aimed at closing the gap between total reflectivity measured on the beam line and obtained in the simulations [77].

Azimuthal distributions acquired in this thesis are being used to simulate electron cloud build [78] up using the code PyECLOUD [79].

Regarding the eLinac Project [6], I propose using a bending magnet to generate useful SR for experimental use. We could use `Synrad3D` to predict the behaviour of the emitted photons.

References

[1] F. R. Elder, A. M. Gurewitsch, R. V. Langmuir, and H. C. Pollock. Radiation from electrons in a synchrotron. *Phys. Rev.*, 71:829–830, Jun 1947. doi: 10.1103/PhysRev.71.829.5. URL `https://link.aps.org/doi/10.1103/PhysRev.71.829.5`.

[2] O. S. Brüning, P. Collier, P Lebrun, S. Myers, R. Ostojic, J. Poole, and P. Proudlock. *LHC Design Report*. CERN Yellow Reports: Monographs. CERN, Geneva, 2004. URL `https://cds.cern.ch/record/782076`.

[3] G. Dugan and D. Sagan. *Synrad3D Photon Tracking Program*. CLASSE, Cornell U., Ithaca, N.Y., 10 Nov 10 November 2017. URL `https://www.classe.cornell.edu/~dcs/manuals/synrad3d.pdf`.

[4] J. G. Contreras and M. Napsuciale. Creation of a group on particle accelerator science and technology in mexico. *Journal of Physics: Conference Series*, 761(1):012002, 2016. URL `http://stacks.iop.org/1742-6596/761/i=1/a=012002`.

[5] Cristhian Valerio Lizarraga, Alejandro Castilla Loaeza, Gerardo Guillermo CantÃ³n, Carlos Duarte, Daniel Chavez Valenzuela, Karim HernÃ¡ndez ChahÃn, Humberto Maury Cuna, Luis Medina Medrano, Juan Reyes Herrera, Salvador Sosa GÃ¼itrÃ³n, Alan Valdivia GarcÃa, and Bruce Yee RendÃ³n. Science and technology of accelerators. *Journal of Physics: Conference Series*, 761(1):012005, 2016. URL `http://stacks.iop.org/1742-6596/761/i=1/a=012005`.

[6] Cristhian Valerio-Lizarraga, Duarte-Galvan Carlos, D Chavez Valenzuela, G.H.I. Maury Cuna, L Medina, Karim Hernandez Chahin, G Guillermo CantÃ³n, and B Yee-Rendon. Study of the first mexican rf linear accelerator. 64:116–121, 01 2018.

[7] A.R. Steere. *A Timeline of Major Particle Accelerators*. Michigan State University. Department of Physics and Astronomy, 2005. URL `https://books.google.ch/books?id=YRNonQEACAAJ`.

[8] J.D. Cockcroft and E. T. S. Walton. Experiments with high velocity positive ions.–(i) further developments in the method of obtaining high velocity positive ions. *Proceedings of the Royal Society of London A: Mathematical, Physical and Engineering Sciences*, 136(830):619–630, 1932. ISSN 0950-1207. doi: 10.1098/rspa.1932.0107. URL `http://rspa.royalsocietypublishing.org/content/136/830/619`.

[9] D.A. Eastham. Voltage limitations of electrostatic accelerators. *Nuclear Instruments and Methods in Physics Research*, 220(1):101 – 103, 1984. ISSN 0167-5087. doi: https://doi.org/10.1016/0167-5087(84)90415-0. URL `http://www.sciencedirect.com/science/article/pii/0167508784904150`.

[10] G Ising. Prinzip einer Methode zur Herstellung von Kanalstrahlen hoher Voltzahl. *Ark. Mat. Astron. Fys.*, 18(30):1–4, 1924. URL `https://cds.cern.ch/record/433984`.

[11] Rolf Wideröe. Über ein neues prinzip zur herstellung hoher spannungen. *Archiv für Elektrotechnik*, 21(4):387–406, Jul 1928. ISSN 1432-0487. doi: 10.1007/BF01656341. URL `https://doi.org/10.1007/BF01656341`.

[12] Ernest O. Lawrence. Method and apparatus for the acceleration of ions, Feb 1934.

[13] V. I. Veksler. Concerning some new methods of acceleration of relativistic particles. *Phys. Rev.*, 69:244–244, Mar 1946. doi: 10.1103/PhysRev.69.244. URL `https://link.aps.org/doi/10.1103/PhysRev.69.244`.

[14] Edwin M. McMillan. The synchrotron—a proposed high energy particle accelerator. *Phys. Rev.*, 68:143–144, Sep 1945. doi: 10.1103/PhysRev.68.143. URL `https://link.aps.org/doi/10.1103/PhysRev.68.143`.

[15] F. K. Goward and D. E. BarnesS. Experimental 8 mev. synchrotron for electron acceleration. *Nature*, 158:413 EP –, Sep 1946. URL `http://dx.doi.org/10.1038/158413a0`.

[16] M. Hildred Blewett. The Cosmotron – a review. *Review of Scientific Instruments*, 24(9):725–737, 1953. doi: 10.1063/1.1770822. URL `https://doi.org/10.1063/1.1770822`.

[17] O. Piccioni, D. Clark, R. Cool, G. Friedlander, and D. Kassner. External proton beam of the cosmotron. *Review of Scientific Instruments*, 26(2):232–233, 1955. doi: 10.1063/1.1771259. URL `https://doi.org/10.1063/1.1771259`.

[18] K Hubner and T M Taylor. The Birth and Development of the First Hadron Collider The CERN Intersecting Storage Rings (ISR). Technical Report CERN-ACC-2013-0248, CERN, Geneva, Nov 2013. URL `http://cds.cern.ch/record/1626809`. Presented at the International Symposium on Subnuclear Physics: Past, Present and Future , held at the Pontifical Academy of Sciences in 30th October - 2nd November 2011.

[19] Edoardo Amaldi. *The Bruno Touschek legacy: Vienna 1921 - Innsbruck 1978*. CERN Yellow Reports: Monographs. CERN, Geneva, 1981. URL `https://cds.cern.ch/record/135949`.

[20] Pedro Waloschek. *The infancy of particle accelerators: life and work of Rolf Widerøe*. Vieweg, Wiesbaden, 1994. URL `http://cds.cern.ch/record/2023494`.

[21] Kjell Johnsen. CERN Intersecting Storage Rings (ISR). *Proc. Natl. Acad. Sci. U. S. A.*, 70:619–626. 8 p, 1973. URL `https://cds.cern.ch/record/2318386`. National Academy of Sciences Autumn Meeting (October 1972): Symposium: New Accelerators.

[22] Bruce Strauss and Steven ST Lorant. Superconductors and particle physics entwined. *CERN Courier*, 57(7):37–42, Sep 2017. URL `https://cds.cern.ch/record/2287619`.

[23] Arsenij Aleksandrovich Sokolov and Igor Mikhailovich Ternov. *Synchrotron radiation*. Akademie-Vrlg., Berlin, 1968. URL `https://cds.cern.ch/record/110140`. Trans. from the Russian.

[24] John David Jackson. *Classical electrodynamics*. Wiley, New York, NY, 3rd ed. edition, 1999. ISBN 9780471309321. URL `http://cdsweb.cern.ch/record/490457`.

[25] URL `http://physics.fullerton.edu/~jimw/general/inertia/efields.gif`. Accessed June 2016.

[26] H. Wiedemann. *Particle Accelerator Physics*. SpringerLink: Springer e-Books. Springer, 2007. ISBN 9783540490456. URL `http://books.google.com.mx/books?id=S8CfmLe87RAC`.

[27] URL `http://upload.wikimedia.org/wikipedia/commons/5/58/Syncrotron.png`. Accessed June 2016.

[28] M. Moreno. private communication, 19 July 2018.

[29] F Ruggiero, Giovanni Rumolo, and Frank Zimmermann. Simulation of the electron-cloud build up and its consequences on heat load, beam stability and diagnostics. *Phys. Rev. Spec. Top. Accel. Beams*, 4(CERN-SL-2000-073-AP): 012801. 24 p, Oct 2000. URL `https://cds.cern.ch/record/473534`.

[30] Matthew Sands. The Physics of Electron Storage Rings: An Introduction. *Conf. Proc.*, C6906161:257–411, 1969.

[31] G Rumolo, G Arduini, V Baglin, H Bartosik, N Biancacci, P Baudrenghien, G Bregliozzi, P Chiggiato, S Claudet, R De Maria, J Esteban-Muller, M Favier, C Hansen, W Höfle, J M Jimenez, V Kain, G Lanza, K S B Li, G H I Maury Cuna, E Métral, G Papotti, T Pieloni, F Roncarolo, B Salvant, E N

Shaposhnikova, R J Steinhagen, L J Tavian, D Valuch, W Venturini Delsolaro, F Zimmermann, U Iriso, O Dominguez, E Koukovini-Platia, N Mounet, C Zannini, and C M Bhat. Electron Cloud observation in the LHC. (CERN-ATS-2011-105):3 p, Sep 2011. URL `https://cds.cern.ch/record/1381532`.

[32] G Rumolo, G Iadarola, O Domínguez, G Arduini, H Bartosik, S Claudet, J Esteban-Müller, F Roncarolo, E Shaposhnikova, and L Tavian. Electron cloud effects in the LHC in 2011. 2012. URL `https://cds.cern.ch/record/1975505`.

[33] Frank Zimmermann. A simulation study of electron-cloud instability and beam-induced multipacting in the LHC. Technical Report LHC-Project-Report-95. CERN-LHC-Project-Report-95. SLAC-PUB-7425, CERN, Geneva, Feb 1997. URL `https://cds.cern.ch/record/323928`.

[34] G.H.I. Maury et al. Synchrotron-radiation photon distribution for highest energy circular colliders. In *Proc. 4th International Particle Accelerator Conferenc*, page 1340, May 2013.

[35] L.R. Evans. *The Large Hadron Collider: A Marvel of Technology*. Fundamental sciences. EPFL Press, 2009. ISBN 9782940222346. URL `http://books.google.com.mx/books?id=tl8fLB1viQcC`.

[36] Eberhard Keil. The CERN Large Hadron Collider LHC. (LHC-Project-Report-83. CERN-LHC-Project-Report-83):12 p, Dec 1996. URL `https://cds.cern.ch/record/321820`.

[37] O. Brüning, P. Collier, P. Lebrun, S. Myers, R. Ostojic, J. Poole, and P. Proudlock. LHC design report(Volume I, The LHC main ring). *Reports-CERN*, 2004.

[38] O Grobner. The LHC vacuum system. In *Particle Accelerator Conference, 1997. Proceedings of the 1997*, volume 3, pages 3542–3546. IEEE, 1997.

[39] R. Cimino, M. Commisso, D. R. Grosso, T. Demma, V. Baglin, R. Flammini, and R. Larciprete. Nature of the decrease of the secondary-electron yield

by electron bombardment and its energy dependence. *Phys. Rev. Lett.*, 109: 064801, Aug 2012. doi: 10.1103/PhysRevLett.109.064801. URL `https://link.aps.org/doi/10.1103/PhysRevLett.109.064801`.

[40] V. Baglin. private communication, 14 December 2015.

[41] G Apollinari, I Béjar Alonso, O Brüning, M Lamont, and L Rossi. *High-Luminosity Large Hadron Collider (HL-LHC): Preliminary Design Report.* CERN Yellow Reports: Monographs. CERN, Geneva, 2015. URL `https://cds.cern.ch/record/2116337`.

[42] Stéphane Fartoukh. Achromatic telescopic squeezing scheme and application to the LHC and its luminosity upgrade. *Phys. Rev. ST Accel. Beams*, 16: 111002, Nov 2013. doi: 10.1103/PhysRevSTAB.16.111002. URL `https://link.aps.org/doi/10.1103/PhysRevSTAB.16.111002`.

[43] R. de Maria. HL-LHC version 1.1 'Collision sFlat', viewed 11 May 2017. URL `http://abpdata.web.cern.ch/abpdata/lhc_optics_web/www/hllhc11/`.

[44] R. de Maria. HL-LHC version 1.1 'Presqueeze optics', viewed 11 May 2017. URL `http://abpdata.web.cern.ch/abpdata/lhc_optics_web/www/hllhc11/`.

[45] R De Maria and S Fartoukh. SLHCV3.0: layout, optics and long term stability. Technical Report sLHC-PROJECT-Report-0050. CERN-sLHC-PROJECT-Report-0050, CERN, Geneva, Nov 2010. URL `https://cds.cern.ch/record/1307558`.

[46] R. Contino et al. Physics at a 100 TeV pp collider: Higgs and EW symmetry breaking studies. *CERN Yellow Report*, (3):255–440, 2017. doi: 10.23731/CYRM-2017-003.255.

[47] Frank Zimmermann. Future Colliders for Particle Physics - "Big and Small". Technical Report arXiv:1801.03170, Jan 2018. URL `https://cds.cern.ch/record/2299950`. "Submitted to the proceedings of the Third European

Advanced Accelerator Concepts Workshop "EAAC2017", La Biodola, 24-30 September 2017; to be published in NIMA Proceedings".

[48] Michael Benedikt and Frank Zimmermann. Towards Future Circular Colliders. *J. Korean Phys. Soc.*, 69(CERN-ACC-2016-0004. 6):893–902. 21 p, Dec 2015. URL `https://cds.cern.ch/record/2120669`.

[49] R. Kersevan. Research program on the cryogenic beam-vacuum of the FCC-hh. In *Int. Conf. on High Energy Physics (ICHEP16), Chicago*, August 2016. URL `https://indico.cern.ch/event/432527/contributions/1072528/attachments/1319192/1977747/Research_program_on_the_cryogenic_beam-vacuum_of_the_FCC-hh_-_ICHEP_2016.pdf`.

[50] G. Apollinari et al. High-Luminosity Large Hadron Collider (HL-LHC): Technical Design Report V. 0.1. *CERN Yellow Report CERN-2017-007-M*, 2017.

[51] Philippe Lebrun and Laurent Tavian. Beyond the large hadron collider: A first look at cryogenics for cern future circular colliders. *Physics Procedia*, 67:768 – 775, 2015. ISSN 1875-3892. doi: https://doi.org/10.1016/j.phpro.2015.06.130. URL `http://www.sciencedirect.com/science/article/pii/S1875389215005118`. Proceedings of the 25th International Cryogenic Engineering Conference and International Cryogenic Materials Conference 2014.

[52] R. Kersevan. Beam screen design and cooling, vacuum aspects, synchrotron radiation. In *Review of the FCC-hh Injection Energy, CERN, 16 October 2015, http://indico.cern.ch/event/449449.*, October 2015. URL `http://indico.cern.ch/event/449449`.

[53] D. Sagan G. Dugan. *Synrad3D Photon Tracking Program*. Cornell University, 2013. URL `http://www.lepp.cornell.edu/~dcs/synrad3d.pdf`.

[54] A.Spizzichino P. Beckmann. *The Scattering of Electromagnetic Waves from Rough Surfaces*. Pergamon Press, New York, 1963. ISBN 0890062382. URL `http://www.amazon.com/`

`Scattering-Electromagnetic-Surfaces-Artech-Library/dp/0890062382`.

[55] J.A. Ogilvy. *Theory of Wave Scattering from Random Rough Surfaces.* Hilger, Bristol, 1991. ISBN 0750300639. URL `http://www.amazon.com/Theory-Scattering-Random-Rough-Surfaces/dp/0750300639`.

[56] J.C. Davis B.L. Henke, E.M. Gullikson. *X-ray interactions: photoabsorption, scattering, transmission, and reflection at E=50-30000 eV,=1-92, Atomic Data and Nuclear Data Tables.* Vol. 54 (no.2), 181-342, 1993. URL `http://henke.lbl.gov/optical`.

[57] N. Mahne et. al. *Experimental Determination of ECLOUD Simulation Input Parameters for DAΦNE.* EuroTev-Report-2005-013, 2005. URL `https://accelconf.web.cern.ch/accelconf/p05/PAPERS/FPAP002.PDF`.

[58] G. Dugan and D. Sagan. Simulating synchrotron radiation in accelerators including diffuse and specular reflections. *Phys. Rev. Accel. Beams*, 20(2): 020708, Feb 2017. ISSN 2469-9888. doi: 10.1103/PhysRevAccelBeams.20.020708. URL `http://link.aps.org/doi/10.1103/PhysRevAccelBeams.20.020708`.

[59] R. Cimino, V. Baglin, and F. Schäfers. Potential remedies for the high synchrotron-radiation-induced heat load for future highest-energy-proton circular colliders. *Phys. Rev. Lett.*, 115:264804, Dec 2015. doi: 10.1103/PhysRevLett.115.264804. URL `https://link.aps.org/doi/10.1103/PhysRevLett.115.264804`.

[60] Hiroshi Akima. A new method of interpolation and smooth curve fitting based on local procedures. *J. ACM*, 17(4):589–602, October 1970. ISSN 0004-5411. doi: 10.1145/321607.321609. URL `http://doi.acm.org/10.1145/321607.321609`.

[61] A. A. Sokolov, F. Eggenstein, A. Erko, R. Follath, S. Künstner, M. Mast, J. S. Schmidt, F. Senf, F. Siewert, T. Zeschke, and F. Schäfers. An XUV

optics beamline at BESSY II. In *Proc. SPIE*, volume 9206, page 92060J, September 2014. doi: 10.1117/12.2061778. URL `http://proceedings.spiedigitallibrary.org/proceeding.aspx?doi=10.1117/12.2061778`.

[62] F. Eggenstein, P. Bischoff, A. Gaupp, F. Senf, A. Sokolov, T. Zeschke, and F. Schäfers. A reflectometer for at-wavelength characterization of XUV-reflection gratings. In Lahsen Assoufid, Haruhiko Ohashi, and Anand K. Asundi, editors, *Proc. SPIE*, volume 9206, page 920607, September 2014. doi: 10.1117/12.2061828. URL `http://proceedings.spiedigitallibrary.org/proceeding.aspx?doi=10.1117/12.2061828`.

[63] Gerardo Guillermo Canton, Marton Ady, Marco Angelucci, Roberto Cimino, Roberto Kersevan, Eliana La Francesca, David Sagan, and Frank Zimmermann. Comparing Behaviour of Simulated Proton Synchrotron Radiation in the Arcs of the LHC with Measurements. In *Proceedings, 8th International Particle Accelerator Conference (IPAC 2017): Copenhagen, Denmark, May 14-19, 2017*, page TUPVA011, 2017. doi: 10.18429/JACoW-IPAC2017-TUPVA011. URL `http://inspirehep.net/record/1626426/files/tupva011.pdf`.

[64] R. Cimino et al. Electron cloud in accelerators. In *Int. J. of Modern Physics A*, volume 29, page 1430023, Jul 2014.

[65] N. Mahne, V. Baglin, I.R. Collins, A. Giglia, L. Pasquali, M. Pedio, S. Nannarone, and R. Cimino. Photon reflectivity distributions from the LHC beam screen and their implications on the arc beam vacuum system. *Applied Surface Science*, 235(1):221 – 226, 2004. ISSN 0169-4332. doi: https://doi.org/10.1016/j.apsusc.2004.05.271. URL `http://www.sciencedirect.com/science/article/pii/S0169433204007676`. 8th European Vacuum Conference and 2nd Annual Conference of the German Vacuum Society.

[66] O. Gröbner. Technological problems related to the cold vacuum system of the LHC. In *Vacuum*, volume 47, pages 591–595, 1996.

[67] G. Guillermo, D. Sagan, and F. Zimmermann. Examining mitigation schemes for synchrotron radiation in high-energy hadron colliders. *Phys. Rev. Accel. Beams*, 21:021001, Feb 2018. doi: 10.1103/PhysRevAccelBeams.21.021001. URL `https://link.aps.org/doi/10.1103/PhysRevAccelBeams.21.021001`.

[68] N. Kos. *Change of beam screen types in Cryo-dipoles for sector 3-4*. LHC-VSS-EC-0010 ver. 1.0, EDMS Document no. 98531. CERN, Geneva, 2004. URL `https://edms.cern.ch/document/985318/1.0`.

[69] URL `http://henke.lbl.gov/optical_constants/layer2.html`.

[70] V. V. Anashin and more. Azimuthal distribution of photoelectrons for an LHC beam screen prototype in a magnetic field. Technical Report Vacuum Technical Note 99-06, CERN, Geneva, 2005. URL `https://edms.cern.ch/document/678269/`.

[71] V. V. Anashin, I. R. Collins, N. V. Fedorov, B. G. Goldenberg, Oswald Gröbner, O. B. Malyshev, and V. P. Nazmov. Reflection of photons and azimuthal distribution of photoelectrons in a cylindrical beam pipe. *Nucl. Instrum. Methods Phys. Res., A*, 448(LHC-Project-Report-266. CERN-LHC-Project-Report-266):76–80. 7 p, Jan 1999. URL `https://cds.cern.ch/record/385374`.

[72] H. Maury Cuna and F. Zimmermann. Electron Cloud with Inverted Beam Screens. Technical Report CERN-ATS-Note-2011-129 TECH, CERN, Geneva, Dec 2011. URL `https://cds.cern.ch/record/1404281`.

[73] G. Guillermo, D. Sagan, and F. Zimmermann. Simulating Proton Synchrotron Radiation in the Arcs of the LHC, HL-LHC and FCC-hh. In *Proc. of Int. Particle Accelerator Conf.*, pages 2073–2076. JACoW, June 2016. ISBN 978-3-95450-147-2. URL `http://jacow.org/ipac2016/papers/weoca03.pdf`.

[74] Michael Benedikt and Frank Zimmermann. Towards future circular colliders. *Journal of the Korean Physical Society*, 69(6):893–902, Sep 2016. ISSN 1976-8524. doi: 10.3938/jkps.69.893. URL `https://doi.org/10.3938/jkps.69.893`.

[75] Michael Benedikt, Daniel Schulte, and Frank Zimmermann. Optimizing integrated luminosity of future hadron colliders. *Phys. Rev. ST Accel. Beams*, 18:101002, Oct 2015. doi: 10.1103/PhysRevSTAB.18.101002. URL `https://link.aps.org/doi/10.1103/PhysRevSTAB.18.101002`.

[76] FCC study website. https://fcc.web.cern.ch/, viewed 11 Nov 2017. URL `https://fcc.web.cern.ch/Pages/fcc-hh.aspx`.

[77] Gerardo Guillermo Canton, Marco Angelucci, Roberto Cimino, Ignasi Bellafont, A. Liedl, Eliana La Francesca, David Sagan, and Frank Zimmermann. Improved Benchmarking of Laboratory reflectivity Data and Simulations for a Sawtooth Chamber. In *Proceedings, 9th International Particle Accelerator Conference (IPAC 2018): Vancouver, Canada, April 29- May 4, 2018*, 2018.

[78] Gerardo Guillermo Canton, Humberto Maury Cuna, Edgar Ocapo, and Frank Zimmermann. Electron Cloud Build Up for the LHC Sawtooth Vacuum Chamberw . In *Proceedings, 9th International Particle Accelerator Conference (IPAC 2018): Vancouver, Canada, April 29- May 4, 2018*, 2018.

[79] Giovanni Iadarola, Giovanni Rumolo, and Giovanni Miano. Electron cloud studies for CERN particle accelerators and simulation code development, Mar 2014. URL `https://cds.cern.ch/record/1705520`. Presented 23 05 2014.

[80] Helmut Wiedemann. *Particle accelerator physics; 3rd ed.* Springer, Berlin, 2007. URL `https://cds.cern.ch/record/1083415`.

[81] *CAS - CERN Accelerator School : 5th General Accelerator Physics Course*, Geneva, 1994. CERN, CERN. URL `https://cds.cern.ch/record/235242`. 2 volumes, consecutive pagination.

[82] Lenny Rivkin. Cern accelerator school: Introduction to accelerator physics, September 5 2014.

[83] R Chasman, G K Green, and E M Rowe. Preliminary Design of a Dedicated Synchrotron Radiation Facility. 1975. URL `https://cds.cern.ch/record/889821`.

[84] D. Einfeld and G. Mülhaupt. Choice of the principal parameters and lattice of bessy, an 800 mev-dedicated light-source. *Nuclear Instruments and Methods*, 172(1):55 – 59, 1980. ISSN 0029-554X. doi: https://doi.org/10.1016/0029-554X(80)90607-2. URL `http://www.sciencedirect.com/science/article/pii/0029554X80906072`.

[85] M. Benedikt and F. Zimmermann, "Towards Future Circular Colliders," Journal Korean Physical Society 69 (2016) 893.

[86] L. Medina Medrano et al., "New HL-LHC Baseline and Performance at Ultimate Energy," presented at IPAC'18, Vancouver, MOPML009, this conference.

[87] H. Damerau et al., "LHC Injectors Upgrade, Technical Design Report, Vol. I: Protons", CERN-ACC-2014-0337 (2014).

[88] FCC Conceptual Design Report, volume 6, High Energy LHC Summary, in preparation.

[89] F. Burkart et al., "Conceptual Design Considerations for a 1.3 TeV superconducting SPS (scSPS)," in *Proc. IPAC'17* Copenhagen (2017).

[90] M. Benedikt, D. Schulte, F. Zimmermann, "Optimizing Integrated Luminosity of Future Hadron Colliders," Phys. Rev. ST Accel. Beams 8, 101002 (2015).

[91] F. Zimmermann, "Luminosity Limitations at Hadron Colliders," in *Proc. 18th International Conference on High-Energy Accelerators (HEACC'01)*, Tsukuba, 26–30 March, 2001; also published as CERN-SL-2001-009-AP (2001).

[92] M. Benedikt and F. Zimmermann, “Proton Colliders at the Energy Frontier,” submitted to NIM A Siegbahn issue, arXiv 1803.09723 (2018).

[93] HiLumi LHC Technical Coordination Committee, `http://espace.cern.ch/HiLumi/TCC`, “Parameters”.

[94] O. Brüning et al., “LHC Design Report, Volume v.1: The LHC Main Ring,” CERN-2004-003-V-1 (2004).

[95] L. van Riesen-Haupt et al., “Integrated Full HE-LHC Optics and Its Performance,” presented at IPAC’18, Vancouver, MOPMK002, this conference.

[96] R. Bruce et al., “Parameters for aperture calculations at injection for HL-LHC”, CERN-ACC-2016-0328 (2016).

[97] S. Izquierdo Bermudez et al., “Multipole field errors for HE-LHC with an effective filament size of 20 μm and ±5% critical-current variation,” private communication, to be published in the FCC Conceptual Design Report (2018).

[98] V.V. Kashikhin, A.V. Zlobin, “Persistent Current Effect in 15-16 T Nb_3Sn Accelerator Dipoles and its Correction”, in *Proc. NAPAC2016* (2016).

[99] J. van Nugteren et al., “Persistent Current Shim Coils for Accelerator Magnets”, CERN TE-MSC Internal Note 2016-03, EDMS Nr. 1574002 (2014).

[100] D. Schoerling, “b_2/b_3 Shimming Recipe and Prospects”, HE-LHC Design Meeting no. 26, 8 March 2018, to be published in the FCC Conceptual Design Report (2018).

[101] Y. Nosochkov et al., “Optimized Arc Optics for the HE-LHC,” presented at IPAC’18, Vancouver, MOPMF067.

[102] L. van Riesen-Haupt et al., “Experimental Interaction Region Optics for the HE-LHC,” presented at IPAC’18, Vancouver, MOPMK006, this conference.

[103] J. Abelleira et al., “HE-LHC Final Focus: Flat Beam Parameters and Energy Deposition Studies,” presented at IPAC’18, Vancouver, MOPMK005, this conference.

[104] M. Crouch et al., "A First Design of the Proton Collimation System for the HE-LHC," unpublished article (2018).

[105] W. Bartmann et al., "Injection and Dump Systems for a 13.5 TeV Hadron Synchrotron HE-LHC," presented at IPAC'18, Vancouver, TUPAF060, this conference.

[106] L. van Riesen-Haupt et al., "Optics for RF Acceleration Section in IR4 for the High Energy LHC," presented at IPAC'18, Vancouver, MOPMK001, this conference.

[107] T. Pieloni et al., "The High-Energy LHC Beam-Beam Effects Studies," presented at IPAC'18, Vancouver, MOPMF069.

[108] T. Pieloni et al., "Beam-Beam Effects Long-Range and Head-On," in *Proc. 6th Evian Workshop*, CERN-ACC-2015-376 (2015).

[109] S. Arsenyev, "Impedance Aspects of the Beamscreen," HE-LHC Design Review, CERN, 11-12 December 2017 (2017); to be published in the FCC Conceptual Design Report (2018).

[110] S. Arsenyev, D. Schulte, "Geometrical Impedance of Pumping Holes and Tapers in the FCC-hh Beamscreen," presented at IPAC'18, Vancouver, MOPMF030, this conference.

[111] B. Salvant et al., "HL-LHC impedance," in preparation.

[112] D. Amorim et al., "Impedance Model for HE-LHC," HE-LHC Design Review, CERN, 11-12 December 2017 (2017); to be published in the FCC Conceptual Design Report (2018).

[113] A. Burov, "Nested head-tail Vlasov solver," Phys. Rev. Accel. Beams 17, 021007 (2014).

[114] N. Mounet, "DELPHI: an analytic Vlasov solver for impedance-driven modes," Talk presented at HSC meeting, CERN, 09 April 2014, `https://espace.cern.ch/be-dep-workspace/abp/-HSC/Meetings/DELPHI-expanded.pdf` (2014).

[115] S. Antipov et al., "HE-LHC Instability Growth Rates," HE-LHC Design Review, CERN, 11-12 December 2017 (2017); to be published in the FCC Conceptual Design Report (2018).

[116] V. Shiltsev, Y. Alexahin, A. Burov, and A. Valishev, "Landau Damping of Beam Instabilities by Electron Lenses," Phys. Rev. Lett. 119, 134802 (2017)

[117] L. Tavian, "Report from the task force on beam-induced heat load," presented at LHC Performance Workshop 2018, Chamonix (2018).

[118] L. Mether, in D. Amorin et al., "Single-Beam Transverse Collective Effects for HE-LHC," ICFA Beam Dynamics Newsletter no. 72, Dec. 2017, `http://icfa-bd.kek.jp/news.html` (2017).

[119] G. Guillermo, D. Sagan, F. Zimmermann, "Examining Mitigation Schemes for Synchrotron Radiation in High-Energy Hadron Colliders," Phys. Rev. Accel. Beams 21, 021001 (2018).

[120] K. Ohmi, F. Zimmermann, and E. Perevedentsev, "Wake-field and fast head-tail instability caused by an electron cloud," Phys. Rev. E 65, 016502 (2001).

Appendix A

Working principles of accelerators

The objective of this section is to provide the reader with the most basic concepts and terminology in accelerators. More details can be found in References [24, 80, 81], which served as basis for this chapter. The concepts and formulas briefly presented here, are not explicitly used later on, but are implicit in all the methods needed to get the results. They are the foundation of the Bmad program mentioned in Sec. 4.1.

Accelerators rely solely in the manipulation of electromagnetic fields for all of its functions. More specifically, electric fields to increase the momentum of the particle, and magnetic fields to guide it through its trajectory.

A.1 Fields and forces

To describe the interaction between charges and electromagnetic fields we start from Maxwell's equations. Through these laws and knowing that the electric field produced by a point charge is proportional to the charge and decays as the square of the distance:

$$E_r(r) = \frac{1}{4\pi\epsilon_0\epsilon}\frac{q}{r^2}, \tag{A.1}$$

where r is the distance to the charge. so, for a beam with radius R of charged particles we have:

$$E_r(r) = \begin{cases} \frac{\rho_0}{2\epsilon_0\epsilon} r & \text{for } r \leq R; \\ \frac{\rho_0}{2\epsilon_0\epsilon} \frac{R^2}{r} & \text{for } r > R. \end{cases} \tag{A.2}$$

$$B_r(r) = \begin{cases} \frac{1}{2}\mu_0\mu j_0 r & \text{for } r \leq R; \\ \frac{1}{2}\mu_0\mu j_0 \frac{R^2}{r} & \text{for } r > R. \end{cases} \tag{A.3}$$

Fields that have a linear growth radially inside the beam and decreases by $\frac{1}{r}$ outside from the beam.

Scalar and vectorial potentials. Given that the divergence of $\vec{B}$ is null, we can express $\vec{B}$ as the rotational of a potential, which we call vector potential $\vec{A}$. Faraday's law can be used to determine the electric field of this vector potential and the scalar potential ϕ.

$$\vec{B} = \nabla \times \vec{A}, \tag{A.4}$$

$$\vec{E} = -\frac{\partial \vec{A}}{\partial t} - \nabla\phi. \tag{A.5}$$

Wave equations. We now express the fields using the potentials in Maxwell equations, while using the Lorentz gauge ($\nabla \cdot \vec{A} = -\frac{\epsilon\mu}{c^2}\frac{\partial\phi}{\partial t}$), and obtain the wave equations

$$\nabla^2\vec{A} - \frac{\epsilon\mu}{c^2}\frac{\partial^2\vec{A}}{\partial t^2} = -\mu_0\vec{j}, \tag{A.6}$$

$$\nabla^2\phi - \frac{1}{c^2}\frac{\partial^2\phi}{\partial t^2} = -\frac{\rho}{\epsilon_0}. \tag{A.7}$$

With knowledge of the charges and currents, we may perform integrals the wave equations to obtains:

$$\vec{A}(R,t) = \frac{\mu_0}{4\pi}\int \frac{\vec{J}}{R}d\tau, \tag{A.8}$$

$$\phi(R,t) = \frac{1}{4\pi\epsilon_0}\int \frac{\rho}{R}d\tau, \tag{A.9}$$

where the integrals are over all the charges and $R \equiv |\vec{r} - \vec{r}'|$.

Lienard-Wiechert potentials. To obtain the potentials of a point charge in motion we need to take into account said motion, and as a result we obtain the Lienard-Wiechert potentials

$$\vec{A}(R,t) = \left.\frac{\mu_0 c}{4\pi}\frac{q}{R}\frac{\beta_r}{1+n\beta_r}\right|_{\tau}, \tag{A.10}$$

$$\phi(R,t) = \left.\frac{1}{4\pi\epsilon_0}\frac{q}{R}\frac{\beta_r}{1+n\beta_r}\right|_{\tau}. \tag{A.11}$$

Equations of motion. The most relevant force in accelerator physics is the Lorentz force $\vec{F} = q\vec{E} + q(\vec{v} \times \vec{B}_r)$, to formulate particle dynamics. Connecting the changes in momenta and energy with the force we get:

$$\left.\begin{aligned} \Delta\vec{p} &= \textstyle\int F dt \\ \Delta E_{kin} &= \textstyle\int F ds \end{aligned}\right\} \rightarrow ds = vdt \rightarrow \vec{\beta}_r \cdot \Delta c\vec{p} = \Delta E_{kin}; \tag{A.12}$$

And expressing it in terms of fields:

$$\Delta E_{kin} = q\int \vec{E}ds + q\int \cancelto{0}{(\vec{v} \times \vec{B}) \cdot} \vec{v}dt, \tag{A.13}$$

which clearly shows that the electric component parallel to the motion of the particle contributes to a change in kinetic energy, while the magnetic does not.

The Lorentz force equation and Eq. A.12 are everything we need to determine the movement of charged particles in the presence of electromagnetic fields.

$$\frac{d\vec{p}}{dt} = \frac{d}{dt}(m\gamma\vec{v}) = eZ\vec{E} + eZ(\vec{v} \times \vec{B}). \tag{A.14}$$

In ultra-relativistic dynamics, the effect of fields on charged particles depend greatly on the angle between the force and the direction of motion of the particle.

Poynting vector. the Poynting vector, $\vec{S}$, is the lost/gained energy through a surface unit in the direction perpendicular to it, $\vec{n}$, and we express it this way:

$$\vec{S} = \frac{1}{\mu_0}[\vec{E} \times \vec{B}]. \tag{A.15}$$

A.2 Special relativity

When we reach high energies with sub-atomic particles or even ions we enter the relativistic regime.

Lorentz transformations. In order to transform a reference system to another that moves with respect to the first one at a velocity v_z, we use the following formulas:

$$\begin{aligned} x &= x', \\ y &= y', \\ z &= \gamma(z' + \beta_{rz}ct'), \\ ct &= \gamma(\beta_{rz}z' + ct'). \end{aligned} \tag{A.16}$$

Lorentz transformations for electromagnetic fields. The electromagnetic fields are transformed in the following way from a frame of reference that moves with respect to the first one at a velocity v_z:

$$\begin{pmatrix} E_x \\ E_y \\ E_z \\ cB_x \\ cB_y \\ cB_z \end{pmatrix} = \begin{pmatrix} \gamma & 0 & 0 & 0 & \gamma\beta_{rz} & 0 \\ 0 & \gamma & 0 & -\gamma\beta_{rz} & 0 & 0 \\ 0 & 0 & 1 & 0 & 0 & 0 \\ 0 & -\gamma\beta_{rz} & 0 & \gamma & 0 & 0 \\ \gamma\beta_{rz} & 0 & 0 & 0 & \gamma & 0 \\ 0 & 0 & 0 & 0 & 0 & 1 \end{pmatrix} \begin{pmatrix} E'_x \\ E'_y \\ E'_z \\ cB'_x \\ cB'_y \\ cB'_z \end{pmatrix}. \tag{A.17}$$

Time dilation. We can derive the dilation of time through two events happening at the same location in two frames of reference:

$$\begin{aligned} \Delta t = t_2 - t_1 = \gamma(t'_2 + \frac{\beta_{rz} z'_2}{c}) - \gamma(t'_1 + \frac{\beta_{rz} z'_1}{c}) \\ \Delta t = \gamma \Delta t' \end{aligned} \tag{A.18}$$

Four-vectors. We consider that four quantities are four-vectors if they are transformed by Lorentz transformations and its norm is invariant, and we denote them with a tilde. ($\tilde{a}$).

Invariance within Lorentz transformations. The magnitude of a four-vector is conserved in all frames of reference. And the internal product is also conserved among systems.

Important four-vectors.

- Space-Time $\tilde{x} = (\vec{x}, ct)$
- 4-velocity $\tilde{v} = (\dot{\vec{x}}, c)$
- 4-Acceleration $\tilde{a} = (\ddot{\vec{x}}, 0)$
- Momentum $\tilde{p} = (\vec{p}, \frac{1}{c}E)$
- Photon $\tilde{k} = (\vec{k}, \frac{1}{c}\omega)$

- Forces $\tilde{F} = (\dot{\vec{p}}, \frac{1}{c}\dot{E})$
- Electromagnetic potential $(c\vec{A}, \phi)$
- 4-Density $(\vec{v}\rho, 1c\rho)$
- 4-Divergence $\tilde{\nabla} = (-\nabla, \partial/\partial t)$

Spacial and espectral distribution of radiation. We should notice the relevance of the invariance of the inner product, when we represent the phase of the electromagnetic waves emitted by moving charges as the inner product of the photon and space-time four-vectors. Transforming the frequency from a frame of reference to another we obtain the relativistic Doppler effect, which gives us the spectral distribution. The same way we can obtain the spatial distribution by transforming the normal spatial directions.

A.3 Elements of classical mechanics

We expand d'Alembert's principle to four-vectors taking into account that the inner product of a four-vector with another or itself is conserved trough Lorentz transformations. In particular, the inner product of the momentum and the diferential of space-time four-vectors:

$$(dx', dy', dz', cdt') \cdot (p'_x, p'_y, p'_z, cE') = -mc^2 dt' = -mc^2\sqrt{1-\beta_r^2}dt. \tag{A.19}$$

We consider this to be the Lagrangian of a particle in its frame of reference. we notice that, for small β_r we obtain the classical Lagrangian. In the presence of electromagnetic fields, we calculate the inner product between the electromagnetic potential and the 4-velocity:

$$e(A_x, A_y, A_z, \phi) \cdot \gamma(v_x, v_y, v_z, 1) = e\gamma(\vec{A} \cdot \vec{v} - \phi). \tag{A.20}$$

And the Lagrangian turns out to be:

$$L = -mc^2\sqrt{1-\beta_r^2} + e(\vec{A}\cdot\vec{v} - \phi). \tag{A.21}$$

A.4 Frenet-Serret coordinates

The particular selection of a coordinate system should not affect the results of the physical phenomena under study. Thus, we should select the most convenient coordinate system to our subject of study. In accelerator science, the most convenient and common coordinate system is the Frenet-Serret. It consists of an orthogonal axis moving along the ideal beam path. This way we easily work with the deviations from such ideal path as shown in Fig. A.1.

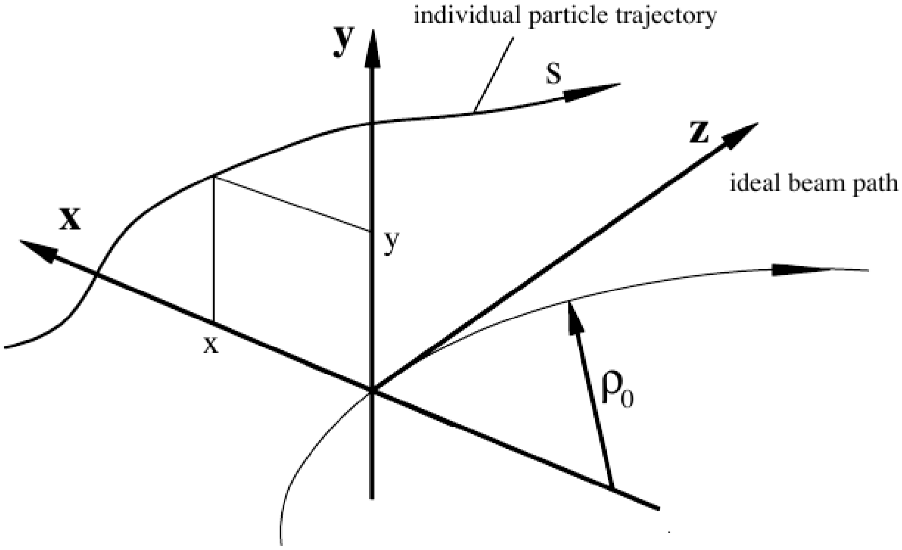

FIGURE A.1: Frenet-Serret Coordinate system. Picture taken from [26].

A.4.1 Hamiltonian formulation

The Hamiltonian formulation is an extension of the classical version to four-vectors. Just as the classical Hamiltonians, we ought to find a coordinate system with the highest number of cyclic variables to simplify the Hamiltonian. To do this, we can use canonical transformations in the same way as the classical form.

Canonical Transformation to Frenet-Serret. We begin by generating a function:

$$G(z,x,y,P_{c,z},P_{c,x},P_{c,y}) = -(c\vec{P_c} - ec\vec{A_c})(\vec{r_0}(z) + x\vec{u_x}(z) + y\vec{u_y}(z)), \qquad \text{(A.22)}$$

$$\begin{aligned}
(cP_z - ecA_z h) &= -\frac{\partial G}{\partial z} = (cP_z - ecA_z)_c h, \\
(cP_x - ecA_x) &= -\frac{\partial G}{\partial x} = (cP_x - ecA_x)_c, \\
(cP_y - ecA_y) &= -\frac{\partial G}{\partial y} = (cP_y - ecA_y)_c.
\end{aligned} \qquad \text{(A.23)}$$

And we obtain the following Hamiltonian:

$$H = e\phi + c\sqrt{m^2c^2 + \frac{(P_z - eA_z h)^2}{h^2} + (P_x - eA_x)^2 + (P_y - eA_y)^2}, \qquad \text{(A.24)}$$

extending the Hamiltonian, taking the time as the coordinate $q_0 = t$ and its conjugate is the negative of the Hamiltonian $P_0 = -H$.

A.5 Beam dynamics

The evolution of the trajectories of the particles under the effect of the Lorentz forces is what we call ‘beam dynamics’ or ‘beam optics’. The most basic formulation consists solely on linear fields that depend only on the distance of the particle over the ideal path and it is called ‘linear beam dynamics’. In this brief description of the working principles of accelerators, we will only discuss linear beam dynamics.

Before going deeper into the dynamics, it would be good to keep in mind that the force exerted by a 1 T magnetic field is similar to one exerted by 300 MV/m and this is why we rely mostly in magnetic fields to guide our particles through the trajectory.

Single particle dynamics. Beam transport systems, based on only bending magnets and quadrupoles, are called linear systems and the resulting theory of particle dynamics in the presence of only such magnets is referred to as linear beam dynamics or linear beam optics.

Furthermore, we will consider only the effect of the electromagnetic fields produced by our setup, i.e. the elements of our accelerator; and neglect all other forces, e.g. gravity, the fields produced by other particles in the same bunch, known as intrabunch scattering, instantaneous photon emissions, etc. This is called 'single particle dynamics'.

A.6 Matrix formalism in linear beam dynamics

To describe particle trajectories analytically through a beam transport line composed of drift spaces, bending magnets, and quadrupoles, we will derive and discuss the matrix formalism. This method makes use of the fact that the magnet strength parameters are constant at least within each individual magnet.

The equations of motion become very simple when the restoring force K is constant and the solutions have the form of trigonometric functions. The particle trajectories may now be described by analytic functions, at least within each uniform element of a transport line, including magnet free drift spaces.

Hard edge model. These solutions can be applied to any arbitrary beam transport line, where the focusing parameter K changes in a step like function along the beam transport line. By cutting this beam line into its smaller uniform pieces so that $K = const.$ in each of these pieces, we will be able to follow the particle trajectories analytically step by step through the whole transport system. This is the model generally used in particle beam optics and is called the hard edge model. The hard edge model is only an approximation, although for practical purposes a rather good one.

A.6.1 Drift space

We call drift space or drift tube a section with no electromagnetic field. In this case particles keep their momentum but are displaced through the length (l) of the element.

In the matrix form:

$$\begin{pmatrix} u(z) \\ u'(z) \end{pmatrix} = \begin{pmatrix} 1 & l \\ 0 & 1 \end{pmatrix} \begin{pmatrix} u_0(z) \\ u_0'(z) \end{pmatrix}. \tag{A.25}$$

A.6.2 Quadrupole

The use of quadrupole magnets to focus the beam, is referred to as *Strong focusing*, and it was mentioned to be essential in the design of the PS.

The equations of motion in the approximation of linear beam dynamics are:

$$x'' + (k_0 + \kappa_{0x}^2)x = 0, \tag{A.26}$$

$$y'' - k_0 y = 0; \tag{A.27}$$

In the matrix form:

$$\begin{pmatrix} u(z) \\ u'(z) \end{pmatrix} = \begin{pmatrix} cos\sqrt{kl} & \frac{1}{\sqrt{k}}\sqrt{kl} \\ -\sqrt{k}sin\sqrt{kl} & cos\sqrt{k} \end{pmatrix} \begin{pmatrix} u_0(z) \\ u_0'(z) \end{pmatrix}. \tag{A.28}$$

A.6.3 Thin lens approximation

We use this approximation when the length of the element is small compared to its focal length. so we take $l \to 0$, with $kl = const$.

in the matrix form:

$$\begin{pmatrix} u(z) \\ u'(z) \end{pmatrix} = \begin{pmatrix} 1 & l \\ -\frac{1}{f} & 1 \end{pmatrix} \begin{pmatrix} u_0(z) \\ u_0'(z) \end{pmatrix}. \tag{A.29}$$

This approximation is not very precise to treat two separate quadrupoles, but when they are symmetric with an anti-symmetric one between them, then it becomes focusing in both planes, and since it can be repeated arbitrarily this combination is very important in beam transport lines and is called a FODO cell.

A.6.3.1 FODO cell

A very useful structure commonly found in accelerators is the FODO cell and it uses only drift sections and quadrupoles. The name comes from focusing-defocusing. This structure consist of a focusing quadrupole with a focal length f, a drift section with length l, a defocusing quadrupole with a focal length $-f$, and finally another drift section with length l.

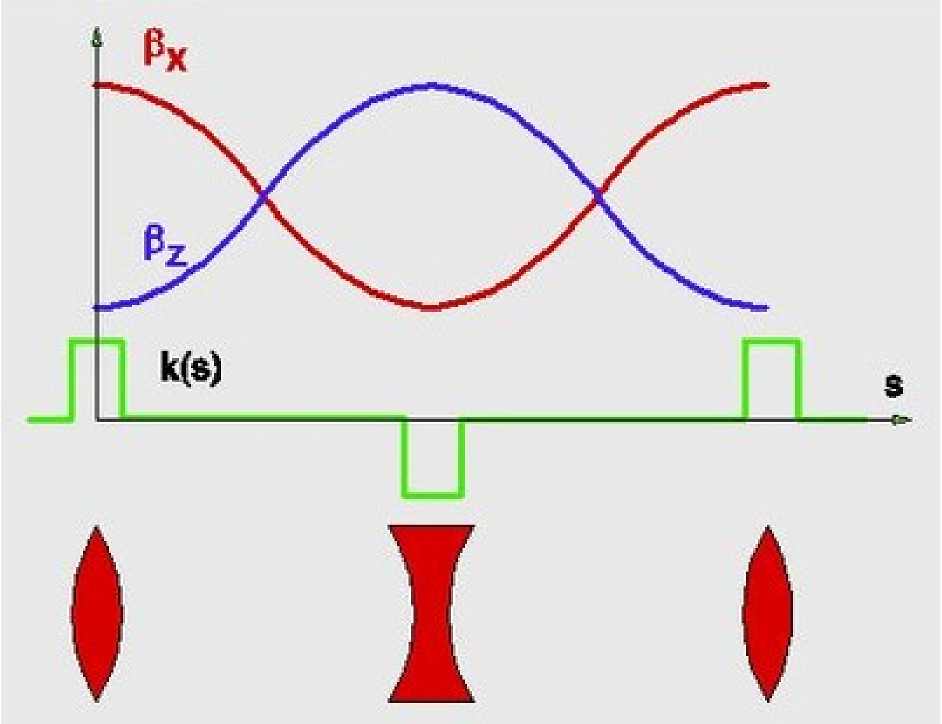

FIGURE A.2: Betatron functions of a typical FODO cell.
Picture taken from [82]

The transport matrix in the thin lens approximation for a FODO cell is:

$$M_{FODO} = \begin{pmatrix} 1 - \frac{L^2}{2f^2} & 2l\left(1 + \frac{l}{2f}\right) \\ -\frac{L}{2f^2}\left(1 - \frac{l}{2f}\right) & 1 - \frac{l}{2f} \end{pmatrix}, \tag{A.30}$$

and its betatron functions are shown in Fig. A.2

A.6.4 Dipole

Weak focusing Particles deviating from the ideal path will travel less or more inside the magnet resulting in a focusing effect. Figure A.3 shows that particles with higher energy will travel a longer distance inside the magnet. This effect is negligible in weak magnets (very small deflection angle).

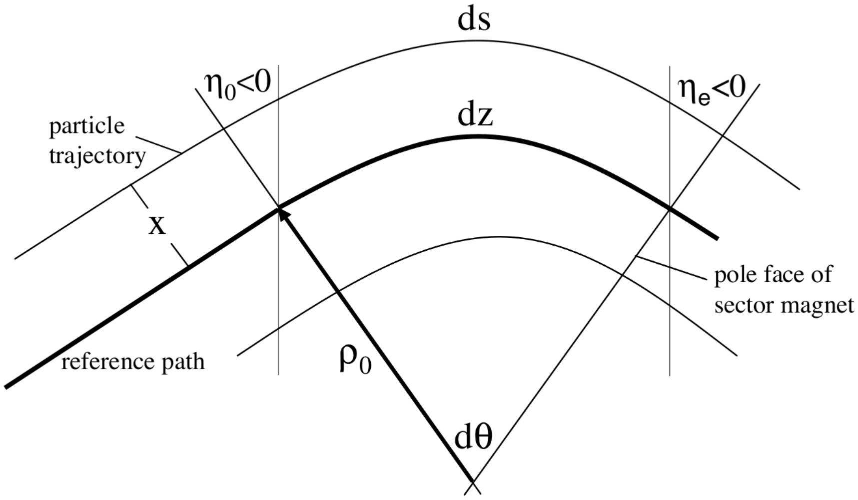

FIGURE A.3: Focusing effect of a bending magnet.
Picture taken from [26].

Fringe field effects and the finite pole gap. Solving the equations taking into account the fringe field effects the result does not deviate from the hard edge model, but from a small deflection angle θ; $\frac{1}{f_x} \approx \kappa_0\theta$.

In the vertical plane the fringe field of a sector magnet leads to defocusing effect which depends on the particular field profile. Both ends provide a small defocusing effect so in order to derive the corrected matrix we multiply the effects on either side of the matrix and we get:

$$M_{l,0} = \begin{bmatrix} 1 + \frac{1}{3}\theta\delta_f & l \\ \frac{2}{3}\frac{\delta_f}{\rho_0} + \frac{1}{9}\frac{\delta_f^2}{\rho_0^2} l & 1 + \frac{1}{3}\theta\delta_f \end{bmatrix}, \tag{A.31}$$

the quadratic term can be ignored but we should remember that the determinant of the matrix should be the unit.

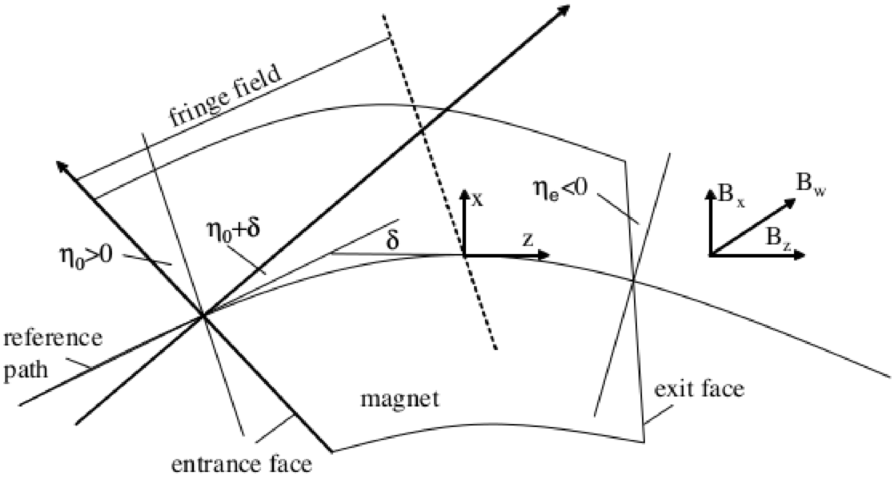

Figure A.4: Wedge Magnet.
Picture taken from [26].

Wedge magnets. First we notice that the fringe fields on this magnet are the same as the sector magnet with a displacement η as shown in Fig A.4. when $\eta > 0$, we obtain a beam focusing in the deflecting plane due the fringe field, and depending on the sign of the pole rotation a focusing or defocusing at the exit.

The corrected matrix is then:

$$M_{w,0} = \begin{bmatrix} 1 & 0 \\ \frac{1}{\rho_0}(\tan\eta_e + \frac{1}{3}\delta_{f_e}) & 1 \end{bmatrix} = \begin{bmatrix} 1 & l \\ 0 & 1 \end{bmatrix} \begin{bmatrix} 1 & 0 \\ \frac{1}{\rho_0}(\tan\eta_0 + \frac{1}{3}\delta_{f0}) & 1 \end{bmatrix}. \tag{A.32}$$

Rectangular magnets. A rectangular magnet is a wedge magnet with parallel faces which end faces equal half of the bending angle. so its matrix can be further simplified:

$$M_{r,0} = \begin{bmatrix} 1 & \rho_0 \sin\theta \\ 0 & 1 \end{bmatrix}. \tag{A.33}$$

In a rectangular dipole magnet we find just the opposite edge focusing properties compared to a sector magnet. The focusing in the deflecting plane of a sector magnet has shifted to the vertical plane in a rectangular magnet and focusing is completely eliminated in the deflecting plane, the focusing strength is reduced by the fraction $\frac{2G}{3L}$ where $2G$ is is the gap height and L is the straight magnet length.

Focusing on wiggler magnets. The fringe field of a wiggler magnet cause focusing in the non-deflecting plane, within the linear approximation there is no focusing effect in the deflecting plane. The focusing in each single wiggler pole is rather weak and we may apply the thin lens approximation.

$$M_{pole} = \begin{bmatrix} 1 & \frac{1}{2}\frac{\lambda_p}{4} \\ 0 & 1 \end{bmatrix}, \tag{A.34}$$

$$M_{wiggler} = M_{pole}^{N}. \tag{A.35}$$

Hard-edge model of wiggler magnets. It is desirable to describe the effects of wiggler magnets in the form of hard edge models when numerical programs are to be used. For the proper modelling of linear wiggler magnet properties, we choose three conditions to be met. The deflection angle for each pole should be the same as that for the equivalent hard edge model. The edge focusing should be the same. A wiggler magnet also contributes to quantum excitation and damping of the beam emittance and beam energy spread.

A.7 Beam lines

A beam line is a transport system formed of optical elements. A linear one is composed only by drift spaces, quadrupoles and bending magnets. A beam line is called a first-order achromat if at the end of the beam line, the position and the slope of a particle are independent of the energy.

A.7.1 Beam description

Having described the trajectory of a single particle through a beam line. We will now look for a way to describe the whole particle beam. To to this, it will be easier to describe the particles in its phase space: (x, p_x, y, p_y, s, E) Although the coordinate E could be changed to ΔP or $\frac{\Delta P}{P_0}$.

We will ignore the coupling between x and y planes, as we will be working in linear beam dynamics only.

A.7.1.1 Emittance

We will start our analysis assuming $\Delta E = 0$ so we can represent the particle distribution by (x, x') and (y, y') separately.

The beam emittance is the space occupied by the beam in phase space. We define three independent two-dimensional beam emittances. Beam emittance can be regarded as the temperature of the beam. This concept becomes very important in describing the beam because the density of particles in phase space does not change along a beam transport line, where the forces acting on particles can be derived from macroscopic electric and magnetic fields. The previous is guaranteed by the Liouville's Theorem.

Transformations in Phase Space. Since the emittance does not change along the beam line, knowing it at the beginning of the transport line will let us know the distribution at any location.

A.7.1.2 Phase ellipse and twiss parameters

It has become customary to surround all particles of a beam in phase space by an ellipse called the phase ellipse, described by:

$$\gamma x^2 + 2\alpha x x' + \beta x'^2 = \epsilon, \tag{A.36}$$

where α,β,γ and ϵ are the ellipse parameters also called ‘Twiss parameters’, and the area enclosed by it, is the emittance [1].

Remembering the formalism discussed in Sec. A.6 we can describe any beam line elements as:

$$\begin{pmatrix} x(z) \\ x'(z) \end{pmatrix} = \begin{pmatrix} C(z) & S(z) \\ C'(z) & S'(z) \end{pmatrix} \begin{pmatrix} x_0(z) \\ x_0'(z) \end{pmatrix}. \tag{A.37}$$

So if we transport the twiss parameters we find that:

$$\begin{aligned} \gamma &= C'^2\beta_0 - 2S'C'\alpha_0 + S'^2\gamma_0, \\ \alpha &= -CC'\beta_0 + (S'C + SC')\alpha_0 - SS'\gamma_0, \\ \beta &= C^2\beta_0 - 2SC\alpha_0 + S^2\gamma_0, \end{aligned} \tag{A.38}$$

and we could also express this as transport matrices for the twiss parameters

---

[1] The literature is not uniform in the representation of numerical values for the beam emittance. Some authors differ in their numerical values by a factor π. Regardless of this difference, the Twiss parameters must be consistent.

$$\begin{pmatrix} \beta(z) \\ \alpha(z) \\ \gamma(z) \end{pmatrix} = \begin{pmatrix} C^2 & -2CS & S^2 \\ -CC' & CS' + C'S & SS' \\ C'^2 & -2C'S' & S'^2 \end{pmatrix} \begin{pmatrix} \beta_0 \\ \alpha_0 \\ \gamma_0 \end{pmatrix}, \tag{A.39}$$

and from the geometric properties we get the relation

$$\beta\gamma - \alpha^2 = 1. \tag{A.40}$$

Waist When $\alpha = 0$ this is called the waist of the beam.

$$\alpha(z) = \begin{cases} + & \text{convergent,} \\ 0 & \text{waist,} \\ - & \text{divergent.} \end{cases} \tag{A.41}$$

In collider design it is very important to plan the collisions at a waist because this will give us a higher luminosity (a higher probability of collisions per crossing).

A.7.1.3 Beam matrix

Particle beams are conveniently described in phase space by enclosing their distribution with ellipses. The definition of the beam matrix elements are measures of the particle distribution in phase space. Most particle beams come with a Gaussian distribution, so we will focus in this shape only. Using the equations of the betatron oscillations described in Sec. A.7.2, for a particle:

$$x_i = a_i\sqrt{\beta}\cos(\psi + \psi_i), \tag{A.42}$$

$$x_i = a_i\frac{\beta'}{2\sqrt{\beta}}\cos(\psi + \psi_i) - a_i\frac{1}{\sqrt{\beta}}\sin(\psi + \psi_i), \tag{A.43}$$

so the beam emittance can be defined as:

$\epsilon^2 =< x_i^2 >< x_i'^2 > - < x_i x_i' >^2$ even for arbitrary particle distributions.

Measurements of the beam emittance. Although we can measure the size of the beam at a given point, we cannot measure its divergence. The emittance is defined by both parameters, so what we can do is measure the size at different points and use the previous formulas to calculate the divergence.

A.7.2 Betatron functions

The changes of the envelope of the particles in the beam through an arbitrary beam transport system can be determined by repeated multiplication of transformation matrices (Eq. A.39) through each of the individual elements of the beam line. This method does not reveal many properties of each particle trajectories. To do this we should solve analytically the equation of motion.

Courant-Snyder invariant. Solving analytically the equation of motion we arrive at the expression: $\gamma u^2 + 2\alpha u u' + \beta u'^2 = \epsilon$. This invariant equation of an ellipse with the area $\pi\epsilon$ is called the Courant-Snyder invariant and the α, β, γ and ϵ are the betatron functions and the beam emittance. The phase ψ from Fig. A.5 is also a betatron function.

To describe the beam as a whole, a beam envelope equation can be defined:

$$E(z) = \sqrt{\epsilon}\sqrt{\beta(z)} \tag{A.44}$$

Knowledge of the betatron functions along a beam line allows us to calculate individual particle trajectories. The betatron functions can be obtained by either solving numerically the differential equations or by using the matrix formalism to transform the phase ellipse parameters. Arriving at:

$$\begin{pmatrix} C(z) & S(z) \\ C'(z) & S'(z) \end{pmatrix} = \begin{pmatrix} \sqrt{\frac{\beta}{\beta_0}}(\cos\psi + \alpha_0 \sin\psi)) & \sqrt{\beta\beta_0}\sin\psi \\ \frac{\alpha_0-\alpha}{\sqrt{\beta\beta_0}}\cos\psi - \frac{1+\alpha\alpha_0}{\sqrt{\beta\beta_0}}\sin\psi & \sqrt{\frac{\beta_0}{\beta}}(\cos\psi + \alpha_0\sin\psi)) \end{pmatrix} \tag{A.45}$$

With initial conditions: $\beta = \beta_0$, $\alpha = \alpha_0$ and $\psi_0 = 0$

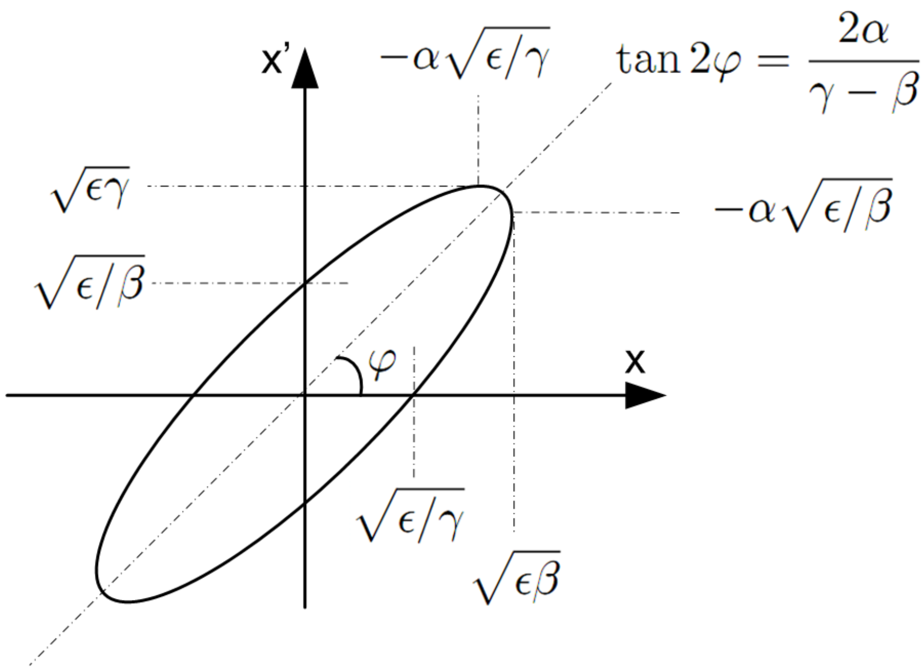

FIGURE A.5: Visual representation of the betatron parameters. Picture taken from [26].

Phase Advance in the drift space In a drift space of length $2L$, the advance in phase is

$$\psi(L) = \int_0^L \frac{dz'/\beta_W}{1+(z'/\beta_W)^2} \text{atan} \frac{L}{\beta_W} \tag{A.46}$$

So the phase advance in a drift space is always $\leq \pi$. where z' is $z - z_W$ and the subindex $_W$ represents a function at the waist.

It is important to notice that the maximum allowed value for the β function in a drift tube is the size of the vacuum pipe we can use.

A.7.3 Chromatic effects.

So far we have been assuming that all particles in the bunch have the same energy. But if we want to properly describe the dynamics of a real particle beam we must include chromatic effects caused by an error in the beam energy or by a spread of energies within the particle beam.

For this we note that the particle deviation u from the reference path is composed of the betatron motion and a displacement due to an energy error. The transformation matrix is therefore a composite of both contributions

$$\begin{pmatrix} u(z) \\ u'(z) \\ \delta \end{pmatrix} = \mathcal{M} \begin{pmatrix} u_\beta(z) \\ u'_\beta(z) \\ 0 \end{pmatrix} + \mathcal{M} \begin{pmatrix} u_\delta(z) \\ u'_\delta(z) \\ \delta \end{pmatrix} \tag{A.47}$$

Where δ is the relative momentum error.

By determining the transformation matrices for individual bending magnets, we are in a position to calculate in matrix formulation the dispersion function anywhere along a beam transport line.

Using the dispersion function: $D(z) = \int_0^z \kappa(z')[S(z)C(z') - C(z)S(z')]dz'$ and taking from the matrix formulation with no betatron oscillations and $\delta = 1$, we find:

$$\begin{pmatrix} D(z) \\ D'(z) \\ \delta \end{pmatrix} = \mathcal{M} \begin{pmatrix} D(z_0) \\ D'(z_0) \\ 1 \end{pmatrix} \tag{A.48}$$

Using this we can work now with 3x3 matrices that include the dispersive term.

Pure sector magnet. The only linear element which introduces dispersion is the bending magnet. Its transformation matrix is:

$$\mathcal{M}_{s,\rho} = \begin{pmatrix} \cos(\theta) & \rho_0 \sin(\theta) & \rho_0(1 - \cos(\theta)) \\ -\frac{1}{\rho_0}\sin(\theta) & \cos(\theta) & \sin(\theta) \\ 0 & 0 & 1 \end{pmatrix}. \tag{A.49}$$

We can follow this with any magnet. Only bending magnets introduce dispersion (only in the bending plane).

Practical use. A spectrometer is a device that measures the energy of particles. The easiest way to do this is making them go through a bending magnet given that they will acquire a dispersion that depends only on its δ.

Linear achromat. Magnets could be arranged in a way to avoid generating a dispersion. These systems composed of only bending magnets and quadrupoles are called linear achromats.

There is dispersion generated by crossing a bending magnet, but if we place another bending magnet half a betatron oscillation downstream the dispersion can be entirely suppressed. Figures A.6 and A.7 show examples of achromats. The first one is the Chasman-Green achromat suggested for a 1.5 GeV dedicated light source in Brookhaven [83]; and the third one is the triple bend achromat suggested for the Berliner Elektronenspeicherring-Gesellschaft für Synchrotronstrahlung (BESSY), an 800 MeV-dedicated light source [84].

Path length and momentum compaction. The only linear contribution to the path length comes from the curved sections of the beam transport line.

$$L = \int (1 + \kappa D(z)\delta) dz \tag{A.50}$$

The variation of the path length with momentum is determined by the momentum compaction factor α_0 :

$$\alpha_c = \frac{\frac{\Delta L}{L_0}}{\delta} \tag{A.51}$$

The travel time of the particle is given by

$$\tau = \frac{L}{c\beta_r} \tag{A.52}$$

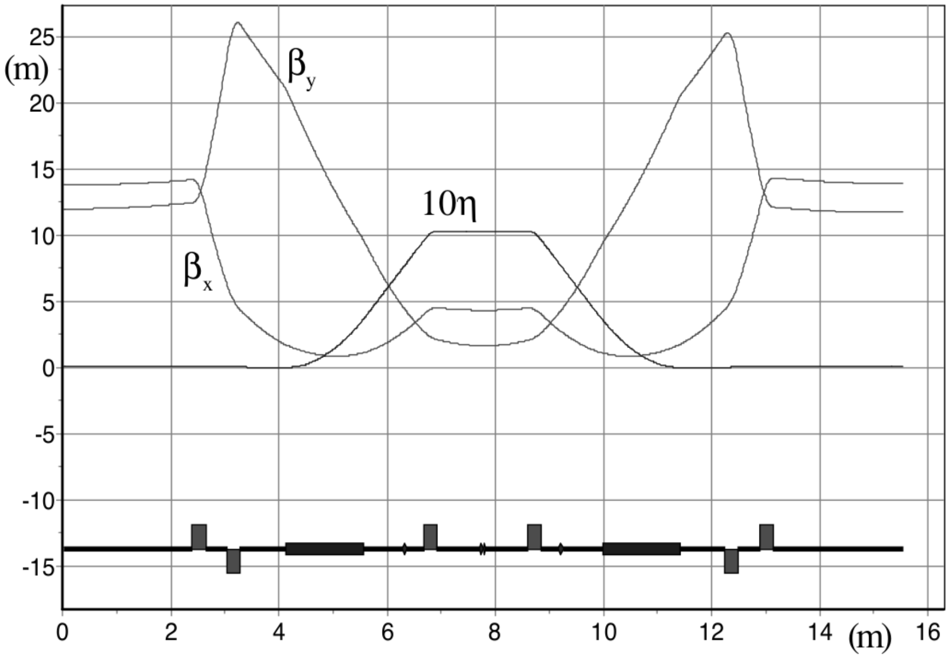

FIGURE A.6: Dependency of the amplitude functions [$\beta_x(s)$, $\beta_y(s)$], the oft-momentum function [$\eta(s)$] for the double-bend achromat [83] Picture taken from [20]

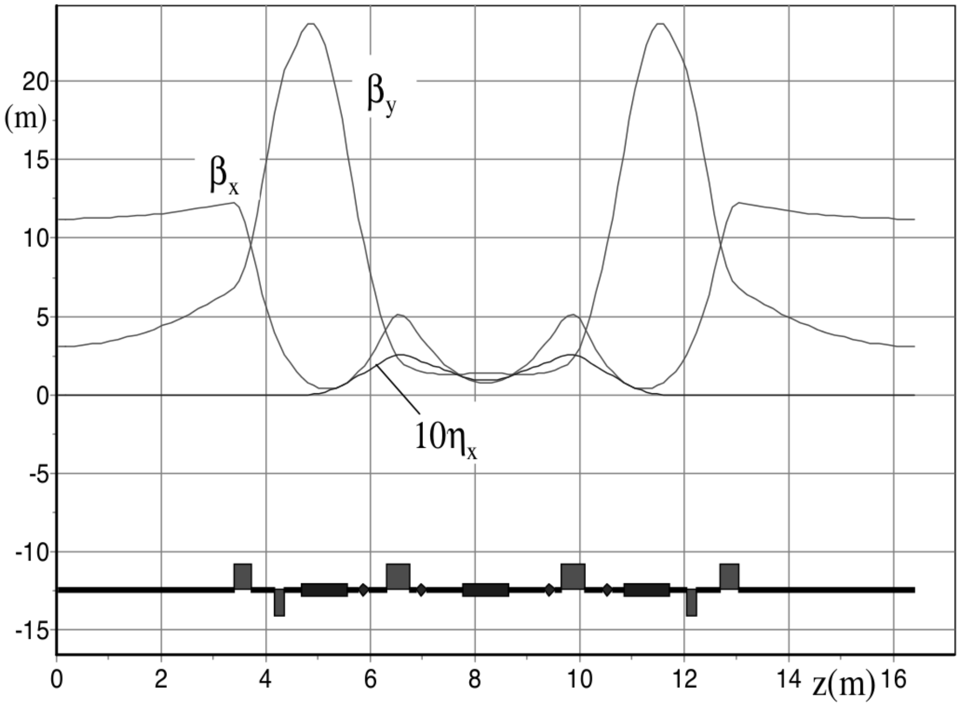

FIGURE A.7: Dependency of the amplitude functions [$\beta_x(s)$, $\beta_y(s)$], the off-momentum function [$\eta(s)$] for the triple-bend achromat used in BESSY [84]. Picture taken from [20]

The variation of τ gives by logarithmic differentiation:

$$\frac{\Delta\tau}{\tau} = \frac{\Delta L}{L} - \frac{\Delta\beta_r}{\beta_r}, \tag{A.53}$$

$$\frac{\Delta\tau}{\tau} = \frac{\Delta L}{L} - \frac{\Delta\beta_r}{\beta_r} = -(\frac{1}{\gamma_r^2} - \alpha_c)\frac{dp}{p} = -\eta_c\frac{dp}{p}. \tag{A.54}$$

We call η_c The momentum compaction. We call the energy for which the momentum compaction vanishes, the transition energy (γ_r), which is an important parameter for longitudinal dynamics and phase stability, which will be mention in Sec. A.8.1.1.

A.8 Longitudinal dynamics

We describe in this subsection the interaction of longitudinal electric fields with charged particles to derive the process of particle acceleration.

The most simple way to accelerate charged particles is through a static field applied to two electrodes. In this case, the total kinetic energy a particle can gain while travelling from one electrode to the other is equal to the product of the particle charge and the voltage between the electrodes. As mentioned in Ch. 1, Afterwards, as suggested by Wideröe, RF cavities were used instead [11]. Application of radio frequency in short rf-fields has become exceptionally effective for the acceleration of charged particles. A free electromagnetic wave does not have a longitudinal electric field component and therefore a special physical environment, called the accelerating structure, must be provided to generate accelerating field components in the direction of propagation. We assume that we were able to generate rf-fields with an electric field component along the path of the particles expressed by

$$E(z,t) = E_0 e^{i(wt-kz)} = E_0 e^{i\psi}. \tag{A.55}$$

The particle momentum changes at a rate equal to the electric force exerted on the particle by the rf-field giving and acceleration shown in Eq. A.56.

$$\frac{dp}{dt} = eE(\psi) = \frac{d}{dt}(\gamma_r mc\beta). \tag{A.56}$$

Multiplying this with the particle velocity we get the rate of change of the kinetic energy, $dE_{kin} = c\beta dp$. Integrating Eq. A.56 with respect to the longitudinal coordinate we obtain instead of the momentum gain, the increase in the kinetic or total energy for the complete accelerating structure

$$\Delta E = (\gamma_r - \gamma_{r0})mc^2 = e\int E(\psi)dz. \tag{A.57}$$

Longitudinal Phase Space Dynamics. For the purpose of developing a theory of stable particle acceleration we may imagine an rf-wave traveling along the path of the particle with a phase velocity equal to the particle velocity and an amplitude which is zero everywhere except in discrete accelerating cavities. For systematic acceleration the phase of the rf-fields must reach specific values at the moment the particles arrive. This phase is called the synchronous phase $\psi_s = \omega t - kz = const$ where ω is the oscillating frequency of the electromagnetic field. The time derivative of synchronous phase vanishes and the synchronicity condition is

$$\dot{\psi}_s = \omega - k\beta_r c = 0 \tag{A.58}$$

So if we set $k = \frac{2\pi}{L}$, the frequency of the electromagnetic field is then

$$\omega_h = k_h\beta_r c = \frac{2\pi}{L}\beta_r c = \frac{2\pi}{\Delta T} \tag{A.59}$$

where h is called the harmonic number and $k_h = hk$ and Eq. A.59 is known as the synchronicity condition.

For circular accelerators:

$$\beta_r \lambda_{rf} h = L. \tag{A.60}$$

This condition requires that the rf-frequency must be changed during acceleration proportional to the particle velocity $\beta_r c$.

A.8.1 Equation of motion in phase space

We cannot assume that the time of flight from one gap to the next is the same for all particles. the synchronicity condition must be modified to account for chromatic effects. Removing the restriction of a constant wave number k, we obtain by a variation of Eq. A.58

$$\Delta\dot{\psi} = -\Delta(k\beta_r c) = -ck\Delta\beta_r - \beta_r c\frac{\partial k}{\partial p}\frac{\partial p}{\partial t}\Delta t, \tag{A.61}$$

where $k = k_h = h\frac{\omega_{rev}}{\beta_r c}$ and L_0 is the distance between accelerating gaps along the ideal path. The synchronous phase is kept constant $\phi_s = const$ or

$$\dot{\psi}_s = 0$$

and serves as the reference phase against which all deviations are measured.

The variation of the wave number with particle momentum is therefore

$$\left.\frac{\partial k}{\partial p}\right|_0 = \left.\frac{\partial k}{\partial L}\frac{\partial L}{\partial p}\right|_0 = -\frac{k_h}{p_0}\alpha_c. \tag{A.62}$$

For a linear accelerator the momentum compaction factor vanishes since the length of a straight line does not depend on the momentum.

With $\frac{\partial p}{\partial t}\Delta t = \Delta p$ and $mc\gamma_r^3\Delta\beta_r = \Delta p$ and we get:

$$\dot{\psi} = -\beta_r ck_h(\gamma_r^{-2} - \alpha_c)\frac{\Delta cp}{cp_0}. \tag{A.63}$$

The term γ^2 appears together with the momentum compaction factor and therefore has the same physical relevance. This term represents the variation of the particle velocity with energy. Therefore, even in a linear accelerator the time of flight between accelerating gaps is energy dependent as long as particles are still non-relativistic.

After differentiation with respect to the time, we get the equation of motion in the longitudinal direction describing the variation of the phase with respect to the synchronous phase ϕ_s for particles with a total momentum deviation Δp

$$\ddot{\psi} + \frac{\partial}{\partial t}(\beta_r c k_h \eta_c \frac{\Delta cp}{cp_0}). \tag{A.64}$$

In most practical applications the particle velocity $\beta_r c$, or the energy vary only slowly during acceleration compared to the rate of change of the phase and we consider them for the time being as constants. The slow variation of these parameters constitutes an adiabatic variation of external parameters for which Ehrenfest's theorem holds [2]. The equation of motion in the potential of the rf-field becomes in this approximation

$$\ddot{\psi} + \frac{\beta_r c k_h \eta_c}{cp_0} \frac{\partial}{\partial t} \Delta cp = 0. \tag{A.65}$$

Integration of the electrical fields along the accelerating sections returns the kinetic energy gain per turn

$$e \int_L E(\psi) dz = eV(\psi). \tag{A.66}$$

Small Oscillation Amplitudes. The ideal particle arrives at the accelerating cavities exactly at the synchronous phase ψ_s, most other particles in a real beam arrive at slightly different phases. For small deviations ψ_s from the synchronous phase

$$\phi = \psi - \psi_s. \tag{A.67}$$

---

[2] The Ehrenfest theorem, relates the time derivative of the expectation values of the position and momentum operators x and p to the expectation value of the force $F = V(s)$ where $V(s)$ is the scalar potential.

We can expand the accelerating voltage into a Taylor series at $\psi = \psi_s$ and get for the average rate of change of the particle energy with respect to the energy of the synchronous particle from the equation:

$$\frac{d}{dt}\Delta E = \frac{1}{T_0}\left[eV(\psi_s) + e\left.\frac{dV}{d\psi}\right|_{\psi_s} \phi - U(E_0) - \left.\frac{dU}{dE}\right|_{E_0} \Delta E \right], \tag{A.68}$$

where the time of flight T_o is $T_o = \frac{L_0}{\beta c}$ since $\beta_r \Delta cp = \Delta E$ we get when $\ddot{\psi} = \ddot{\phi}$

From that we get the equation of motion:

$$\ddot{\phi} + \frac{\beta_r c k_h \eta_c}{cp_0 T_0} e \left.\frac{dV}{d\psi}\right|_{\psi_s} \phi - \frac{c k_h \eta_c}{T_0} \left.\frac{dU}{dE}\right|_{E_0} \frac{\Delta cp}{cp_0} = 0, \tag{A.69}$$

and using $\psi = \psi_s + \phi$

$$\ddot{\phi} + 2\alpha_z \dot{\phi} + \Omega^2 \phi = 0, \tag{A.70}$$

were the damping decrement is

$$\alpha_z = +\frac{1}{2T_0} \left.\frac{dU}{dE}\right|_{E_o}, \tag{A.71}$$

and the synchrotron frequency

$$\Omega^2 = +\frac{\beta_r c k_h \eta_c}{cp_0 T_0} e \left.\frac{dV}{d\psi}\right|_{\psi_s}. \tag{A.72}$$

Particles orbiting in a circular accelerator perform longitudinal oscillations with the frequency Ω. This phase equation is valid only for small oscillation amplitudes, because only the linear term has been used in the expansion for the rf-voltage. The small amplitude approximation is accurate to describe most of the fundamental features of phase oscillations. The phase equation has the form of the equation of motion for a damped harmonic oscillator and we will look for conditions leading to a positive frequency and stable phase oscillations. These oscillations are also called synchrotron oscillations.

In most cases, the accelerating voltage can be expressed by a sinusoidal waveform:

$$V(\psi) = \hat{V}_0 \sin\psi,$$

and expanded about the synchronous phase to get with $\psi = \psi_s + \phi$

$$V(\psi_s + \phi) = \hat{V}_0(\sin\psi_s \cos\phi + \sin\phi \cos\psi_s). \tag{A.73}$$

Keeping only linear terms in ϕ the phase equation is $\ddot{\phi} + \Omega^2\phi = 0$ and the synchrotron oscillation becomes

$$\Omega^2 = \frac{ck_h\eta_c}{cp_0T_0} e\hat{V}_0 \cos\psi_s. \tag{A.74}$$

The rf-frequency is an integer multiple of the revolution frequency $f_{rf} = hf_{rev}$ where the integer h is the harmonic number and the revolution frequency is, with the circumference C: $f_{rev} = \frac{C}{c\beta_r}$ with $\omega_{rev} = 2\pi f_{rev}$

The synchrotron Oscillation Tune (ν_s) is defined as:

$$\nu_s = \frac{\Omega}{\omega_{rev}}. \tag{A.75}$$

A.8.1.1 Phase stability

The synchrotron oscillation frequency must be real and the right-hand side of Eq. A.74 must therefore be positive to obtain stable solutions for phase oscillations. For low particle energies the momentum compaction is in general positive and the energy at which the momentum compaction changes sign is called the transition energy

$$\gamma_{tr} = \frac{1}{\sqrt{\alpha_c}}$$

. The synchronous rf-phase must be selected depending on the particle energy being below or above the transition energy.

Large oscillation amplitudes. This approximation is invalid when $\sin\phi \approx \phi$. In this case we use:

$$\ddot{\phi} = -\Omega^2 \sin\phi, \tag{A.76}$$

which can be derived from the Hamiltonian

$$\mathcal{H} = \frac{1}{2}\dot{\psi}^2 - \Omega^2 \cos\psi, \tag{A.77}$$

being identical to that of a mechanical pendulum. As a consequence of our ability to describe synchrotron motion by a Hamiltonian and canonical variables, we expect the validity of the Poincaré integral

$$J_1 = \int_z d\dot{\phi}\, d\phi = \mathrm{const}, \tag{A.78}$$

under canonical transformations.

The same result as in transverse phase space has been called the beam emittance. So we define an emittance for the longitudinal phase space. We find that it is often more convenient to use the particle momentum instead of $\dot{\phi}$.

Particle trajectories in phase space can be derived directly from the Hamiltonian. These trajectories, well known from the theory of harmonic oscillators, are shown in Fig. A.8.

The trajectories in Fig. A.8 are of two distinct types. Trajectories oscillating about equilibrium and others are not limited to a particular area in phase. The lines separating the regions are called separatrices.

Acceleration of charged particles. The average energy gain per revolution is

$$\Delta E = V(\phi_s) = \hat{V}_0 \sin\phi_s, \tag{A.79}$$

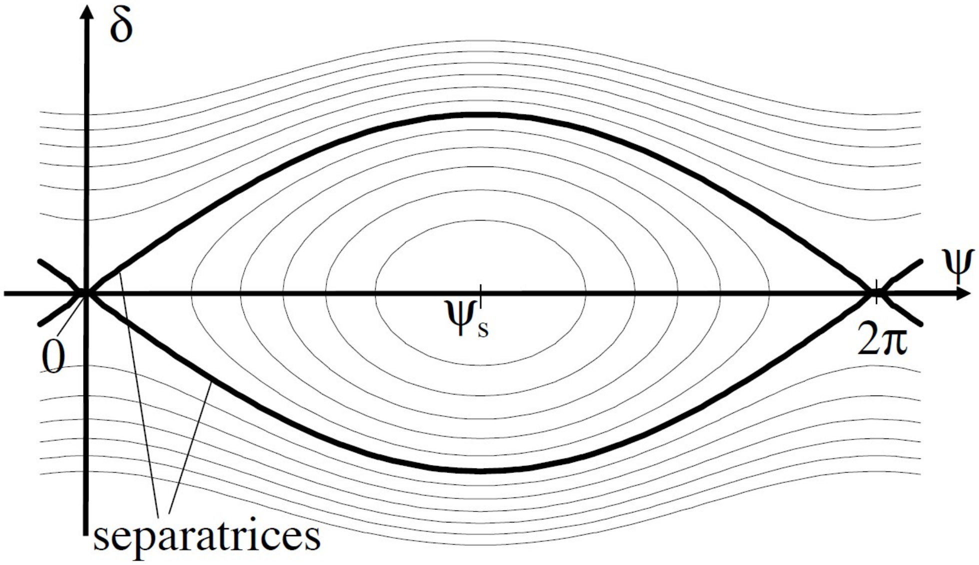

Figure A.8: Phase space diagram for a synchronous phase $\phi_s = \phi$
Picture taken from [20].

and using this $\phi_s \neq 0$ we get a a more general phase equation than Eq. A.76:

$$\ddot{\phi} + \frac{\Omega^2}{\cos\psi_s}[\sin(\psi_s + \phi) - \sin\psi_s] = 0. \tag{A.80}$$

The phase space trajectories depending on the value of the synchronous phase ψ_s are shown in Fig. A.9.

We note clearly the reduction in stable phase space area as the synchronous phase is increased or as the particle acceleration is increased.

A.8.2 Hamiltonian

The Hamiltonian:

$$\frac{1}{2}\dot{\phi}^2 - \frac{\Omega}{\cos\psi_s}[\cos(\psi_s + \phi) - \cos\psi_s + \phi\sin\psi_s] = \mathcal{H} \tag{A.81}$$

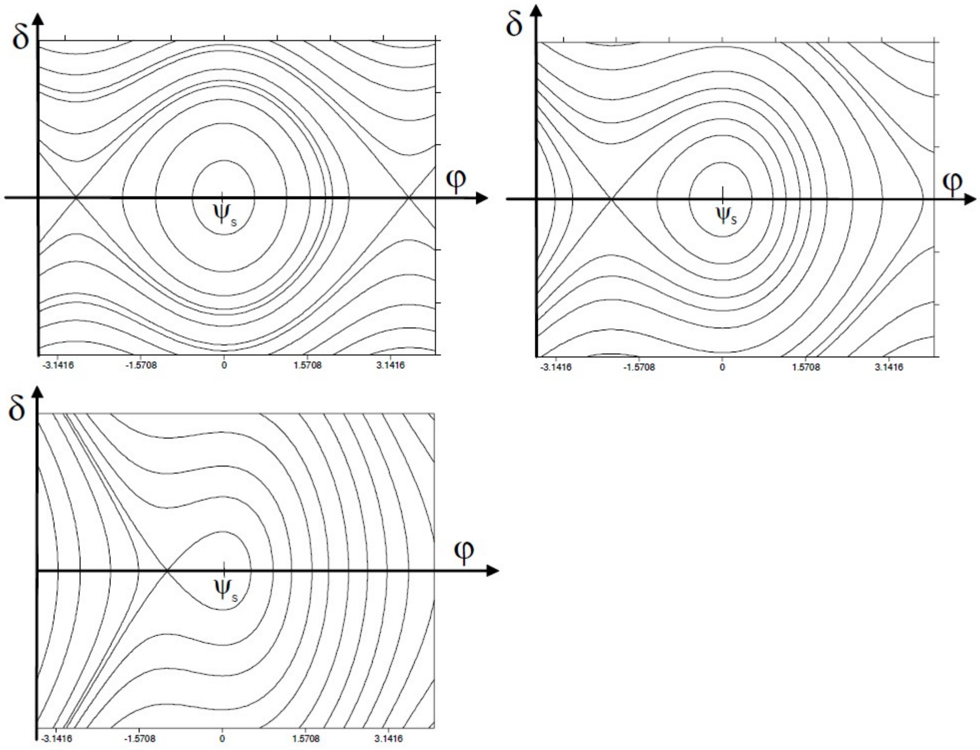

FIGURE A.9: Phase space diagram for a synchronous phase $\phi_s \neq 0$
Picture taken from [20].

describes the particle motion in phase space for arbitrary values of the synchronous phase The energy gain for the synchronous particle at $\psi = \psi_s$ becomes

$$\Delta E = e \int \mathbf{E}(\psi_s)\, d\mathbf{z}$$

We obtain a finite energy gain or loss whenever the synchronous phase in accelerating sections is different from an integer multiple of 180°. The synchronicity condition (Eq. A.59) assures that the acceleration in all accelerating sections is the same for each turn.

A.8.3 RF-Buckets

Phase stable regions in the case of finite values of the synchronous phase are called moving rf-buckets. Figure A.10 shows the relation between the RF-phase and the moving RF-buckets and its dependence on the transition energy (γ_{tr}).

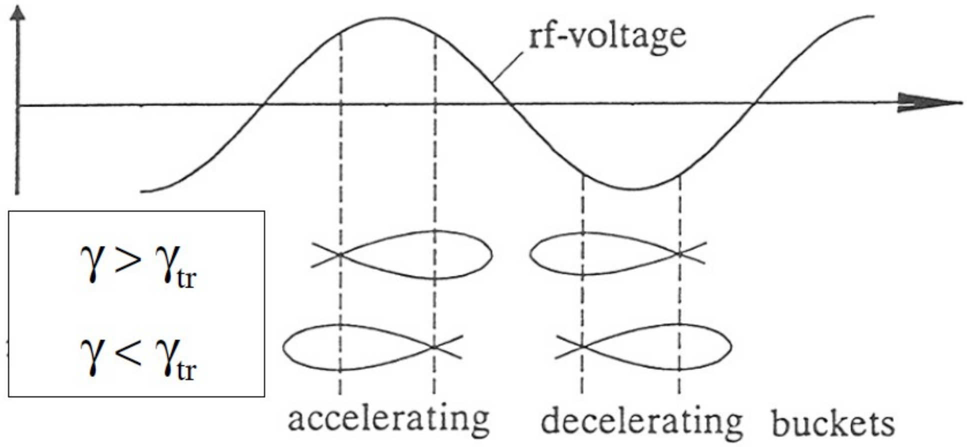

FIGURE A.10: RF-phase and orientation of moving RF-buckets for accelerating and decelerating fields. Picture taken from [20]

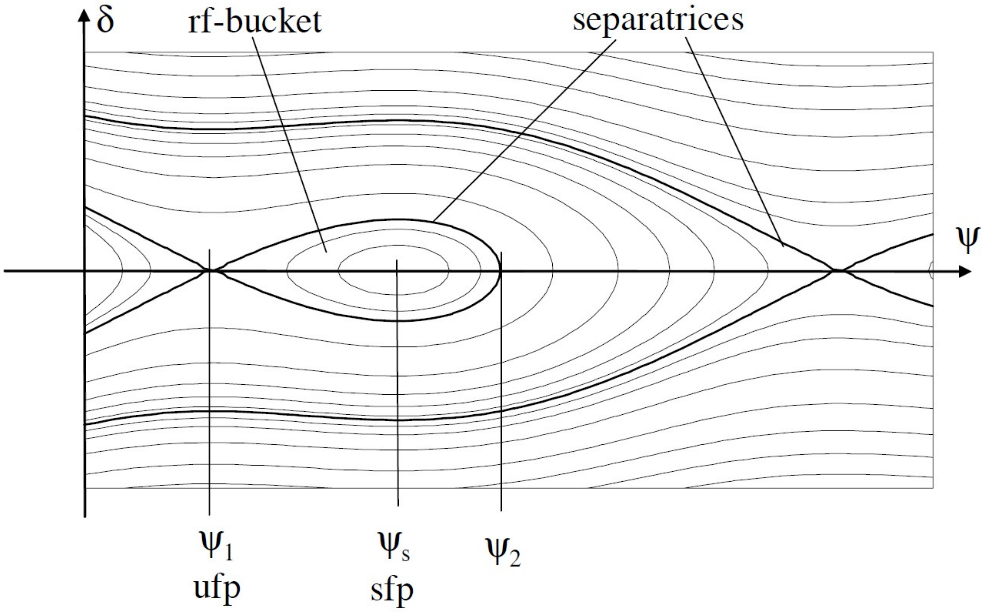

FIGURE A.11: Separatrix parameters in phase space. Picture taken from [20]

A.8.4 Phase space parameters

Separatrix parameters. The ‘focal point’ in the phase diagram is called a stable fixed point (SFP). The unstable fixed point (UFP) is located where the two branches of the separatrix cross. The location of fixed points can be derived from the two conditions:

$$\frac{\partial \mathcal{H}}{\partial \dot{\psi}} = 0, \tag{A.82}$$

$$\frac{\partial \mathcal{H}}{\partial \psi} = 0, \tag{A.83}$$

and can be seen graphically in Fig. A.11.

Momentum acceptance. A characteristic property of the separatrix is therefore the definition of the maximum phase or momentum deviation a particle may have and still undergo stable synchrotron oscillations. The value of the maximum momentum deviation is called the momentum acceptance of the accelerator. In accelerator physics it is customary to define an over voltage factor. This factor is equal to the ratio of the maximum rf-voltage in the cavities to the desired energy gain in the cavity U_0

$$q = \frac{eV_0}{U_0} = \frac{1}{\sin \psi_s}, \tag{A.84}$$

and can be used to replace the trigonometric functions of the synchronous phase.

For a moving bucket the momentum acceptance is:

$$\left(\frac{\Delta p}{p_0}\right)^2_{acc} = \frac{eV_0 \sin \psi_s}{\pi h |\eta_c| c p_0} 2 \left(\sqrt{q^2 - 1} - \mathrm{acos}\frac{1}{q}\right). \tag{A.85}$$

Overall, the momentum acceptance depends on lattice and rf-parameters and scales proportional to the square root of the rf-voltage in the accelerating cavities.

Moving rf-buckets can be measured in units of a stationary rf-bucket, where the proportionality factor depends only on the synchronous phase.

Bunch length. All particles of a beam perform incoherent phase oscillations about a common reference point and thereby generate the appearance of a steady longitudinal distribution of particles, which we call a particle bunch. The total bunch length is twice the maximum longitudinal excursion of particles from the bunch center defined by

$$\frac{l}{2} = \pm \frac{c}{h\omega_{rev}} \hat{\phi} = \pm \frac{\lambda_{rf}}{2\pi} \hat{\phi}, \tag{A.86}$$

where $\hat{\phi}$ is the maximum phase deviation.

The momentum compaction is a lattice function and theoretically allows the bunch length to be adjusted to any small value. For high energy electron rings $\eta_c \approx -\alpha_c$ and by arranging the focusing such that the dispersion functions change sign, the momentum compaction factor of a ring can become zero or even negative. Rings for which $\eta_c = 0$ are called isochronous rings.

To calculate the longitudinal emittance, we evaluate the integral

$$\oint p \, dq$$

where p and q are the conjugate variables describing the synchrotron oscillation.

The acceptance is the maximum value for the beam emittance to be able to pass through a transport line or accelerator components. The acceptance is the area enclosed by the separatrices. We define a longitudinal beam emittance by

$$\epsilon_\phi = \int_s \frac{\Delta E}{\omega_{rf}}. \tag{A.87}$$

Only for $\psi_s = n\pi$ can this integral be solved analytically.

A.8.5 Limits

For moving rf-buckets, the integration must be performed numerically between the limiting phases ψ_1 and ψ_2 and the acceptance for $\psi_s < 180°$ which imposes some practical limits on the maximum rate of acceleration for a given maximum rf-voltage.

Phase space matching. A need for matching exists while transferring a beam from one accelerator to another accelerator or storage ring.

If there is not a good matching, part of the beam may be lost due to lack of overlap with the rf-bucket; or severe phase space dilution may occur if a beam is injected unmatched into a too large rf-bucket.

Other matching problems occur when the injected beam is not continuous.

Adiabatic capture. A sophisticated capturing method that allows us to capture almost all particles in a uniform longitudinal distribution by turning on the rf-voltage very slowly is called 'Adiabatic capture'.

Phase space manipulation. We are able to manipulate within the limits of a constant longitudinal beam emittance the bunch length and momentum spread. The focusing device in this case is the voltage in accelerating cavities. This phase space manipulation can be conveniently expressed with the maximum momentum deviation $(\hat{\Delta} p/p_0)_0$ and the maximum phase deviation $\hat{\phi}_0$ which are related by:

$$\left.\frac{\hat{\Delta} p}{p_0}\right|_0 = \frac{\Omega_0}{h\omega_{rev}|\eta_c|}\hat{\phi}_0 \tag{A.88}$$

, where Ω_0 is the starting synchrotron oscillation frequency for the rf-voltage V_0. Then we increase the voltage up to V_1 and after a quarter of an oscillation in the new frequency Ω_1 the phase spread will have been transformed in energy spread.

A.9 Higher order phase focusing

To accurately describe beam stability when the momentum compaction factor is small or vanishes, we cannot completely ignore higher order terms.

There are two main contributions to the higher order momentum compaction factor, one from the dispersion function and the other from the momentum dependent path length. The analysis of these parameters is outside the scope of this basic introduction.